

AN ABSTRACT OF THE DISSERTATION OF

Frances Lin for the degree of Doctor of Philosophy in Statistics presented on
November 5, 2025.

Title: Copula-Based Mixture Transition Distribution Models for Forecasting Skewed and Zero-Inflated Time Series: Methodology and Comparisons with Deep Learning LSTM Networks

Abstract approved: _____

Lisa Madsen

Charlotte Wickham

Real-world time series in domains such as energy, insurance, and transportation often exhibit skewness and zero-inflation, which can undermine model performance if not properly addressed. To tackle these challenges, we develop the copula-based Gamma Mixture Transition Distribution (Gamma MTD) model and its zero-inflated extension (ZIGamma MTD) to capture high-order dependence, skewed distributions, and semicontinuous patterns. The proposed framework is generalizable, accommodating a wide range of marginal distributions and copula families beyond the Gamma and ZIGamma specifications. Simulation studies show promising results across various scenarios, demonstrating their effectiveness and robustness. Continued development of probabilistic frameworks for skewed and zero-inflated time series is crucial for methodological advancement and for expanding their applicability across a wider

range of fields. While recent AI advances such as Recurrent Neural Networks (RNNs) and Long Short-Term Memory (LSTM) networks effectively capture nonlinear and long-range dependence, claims of LSTM superiority can be misleading with inappropriate benchmarks, and prior work has shown that probabilistic models such as MTD perform comparably in predicting, for example, disease spread. To assess the relative strengths and limitations of each approach, we compare the proposed Gamma and ZIGamma MTD models with LSTM networks. Results from both simulation and real-data applications show that MTD models achieve higher predictive accuracy and greater robustness, albeit at the cost of increased computational demands and more involved model design, whereas LSTMs provide faster predictions but with lower accuracy. These findings highlight the complementary strengths of flexible probabilistic models and AI-driven neural architectures, suggesting opportunities for further advancements that integrate both approaches to better model skewed and zero-inflated time series.

©Copyright by Frances Lin
November 5, 2025
All Rights Reserved

Copula-Based Mixture Transition Distribution Models for Forecasting Skewed
and Zero-Inflated Time Series: Methodology and Comparisons with Deep
Learning LSTM Networks

by

Frances Lin

A DISSERTATION

submitted to

Oregon State University

in partial fulfillment of
the requirements for the
degree of

Doctor of Philosophy

Presented November 5, 2025
Commencement June 2026

Doctor of Philosophy dissertation of Frances Lin presented on November 5, 2025.

APPROVED:

Co-Major Professor, representing Statistics

Co-Major Professor, representing Statistics

Chair of the Department of Statistics

Dean of the Graduate Education

I understand that my dissertation will become part of the permanent collection of Oregon State University libraries. My signature below authorizes release of my dissertation to any reader upon request.

Frances Lin, Author

ACKNOWLEDGEMENTS

First and foremost, I would like to thank my advisors, Lisa Madsen and Charlotte Wickham, for their dedication, support, and inspiration throughout the process. They have not only shaped me as a researcher, but have also inspired me on a personal level through their integrity, kindness, and diligence. I am grateful for all the support they have given. I could not have made it this far without their guidance, nor could I have asked for better advisors. I would also like to thank my committee members, James Molyneux, Claudio Fuentes, and Prasad Tadepalli, for the time they dedicated and for their valuable feedback. I am also grateful to Xiaotian Zheng, whose models formed the basis of our work. He has been incredibly generous with his time and advice.

I am grateful to my family, my mom, dad, and brother, for their occasional financial support and for their patience and understanding throughout the journey. While I am privileged not to be the first in my family to pursue a doctoral degree, the unique challenges of my path have been shared and felt by all of us. I am grateful to my uncle, a professor of statistics in Taiwan, for his lifelong guidance and influence, and to Kate Huntington, a professor of geology at my undergraduate university, for inspiring me and igniting my interest in research. I am thankful to my friends, including my cohort, for their emotional support and for always being there, from late-night talks and fun hikes to ski trips and random food adventures. I am thankful to Gauri, my friend, cohort, and roommate of over five years, and to Baloo, Gauri's dog, for making this experience more manageable. Last but not least, I give special thanks to my partner, Joseph, for his timely distractions and annoyances.

This journey has been a long one: from navigating the challenges of remote work during COVID in 2020-2021, to supporting my grandma as she battled a brain tumor and gradually lost her ability to communicate over the years, the passing of our family dog, Collie, in 2024, swearing in as a U.S. citizen later in the same year, and completing an internship at Posit this summer. I would not have made it this far without the support of the aforementioned people, as well as many others.

TABLE OF CONTENTS

	<u>Page</u>
1 Introduction	1
1.1 Motivation and Objective	1
1.2 Data Challenges	3
1.3 Modeling Approaches	6
1.4 Outline of the Dissertation Chapters	7
I Models for Forecasting Skewed Time Series	8
2 Introduction	9
3 Background	11
3.1 Mixture Transition Distribution Models for Time Series	11
3.2 Model Construction	14
3.2.1 Mixture Weights	14
3.2.2 Transition Kernels	15
3.3 Bayesian Implementation	17
3.3.1 Hierarchical Model Formulation	17
3.3.2 Model Estimation and Prediction	18
4 Proposed Method: Copula-Based Gamma MTD Models	20
4.1 Copula	22
4.2 Marginal Distribution	22
5 Overview of MCMC Algorithms	24
6 Simulation Studies	26
6.1 Simulation Settings	26
6.2 Simulation Results	28
6.2.1 Convergence Diagnostics	28
6.2.2 Weight and Dependence Parameters for Copula	30

TABLE OF CONTENTS (Continued)

	<u>Page</u>
6.2.3 Parameters for Marginal Distributions	31
6.2.4 Sensitivity Analysis	34
6.2.5 Coverage Assessment	34
7 Prediction	38
8 Discussion	40
II Models for Forecasting Zero-Inflated Skewed Time Series	42
9 Introduction	43
10 Background	46
10.1 Zero-Inflated Count Models	46
10.2 Zero-Inflated Count Models for Dependent Data	47
10.2.1 State Space Models	47
10.2.2 Copula-Based Markov Models	48
10.3 Zero-Inflated Continuous models	49
10.4 The Continuous Extension Approach	51
11 Proposed Method: Copula-Based Zero-Inflated Gamma MTD Models	53
11.1 Copula	54
11.2 Marginal Distribution	54
12 Overview of MCMC Algorithms	59
13 Simulation Studies	62
13.1 Simulation Settings	62
13.2 Simulation Results	64
13.2.1 Convergence Diagnostics	64

TABLE OF CONTENTS (Continued)

	<u>Page</u>
13.2.2 Weight and Dependence Parameters for Copula	67
13.2.3 Parameters for Marginal Distributions	67
13.2.4 Coverage Assessment	69
14 Prediction	73
15 Discussion	77
III Copula-Based Markov MTD Models vs. Deep Learning LSTM Networks	79
16 Introduction	80
17 Background	83
17.1 Recurrent Neural Network (RNN) Architecture	83
17.1.1 Recurrent Unit	83
17.1.2 Problems with Long-Term Dependence	84
17.1.3 A Note on Foundation Models such as Transformers	85
17.2 Long Short-Term Memory (LSTM) Network Architecture	87
17.2.1 LSTM Units	87
17.3 Training, Hyperparameter Tuning, and Metrics	90
18 Simulation Studies	95
18.1 Network Configuration	95
18.2 Experimental Setup	96
18.3 Results	98
18.3.1 Prediction for Gamma Scenarios	98
18.3.2 Prediction for Zero-inflated Gamma Scenarios	104
19 Data Applications: NASA MERRA-2 Wind Speeds Data	109

TABLE OF CONTENTS (Continued)

	<u>Page</u>
19.1 Experimental Setup	109
19.1.1 Data Access and Description	109
19.1.2 Model Configuration and Implementation	111
19.2 Results	112
19.2.1 Prediction Results	112
19.2.2 Empirical Coverage of the MTD Model	119
20 Discussion	122
IV Conclusion	125
21 Conclusion	126
V Bibliography	129
Bibliography	130
Appendices	149
Appendices	149

LIST OF FIGURES

Figure	Page
1.1 Time series plot of observed hourly wind speeds (m/s) at heights of (a) 50 m, (b) 10 m, and (c) 2 m above ground level at the Limon Wind Energy Center, Colorado, for the year 2024. Data sourced from MERRA-2 via the NASA GES DISC Earthdata API.	4
1.2 Time series plot of observed values for varying zero-inflated probability (a) $P = 0.1$, (b) $P = 0.5$, and (c) $P = 0.7$. Data generated from a ZIGamma MTD model with mean, scale, and threshold parameters $\mu = 7$, $\beta = 1$, and $\epsilon = 0.1$.	5
3.1 Relationships between $X_1, X_2, X_3, X_4, X_5, \dots, X_t$. The joint distribution is $f(\mathbf{x}) = f(x_1, x_2, x_3, \dots, x_t)$.	12
3.2 Directed relationships between $X_1, X_2, X_3, X_4, X_5, \dots, X_t$ on a DAG. The joint distribution is factored as $f(\mathbf{x}) = f(x_1)f(x_2 x_1)f(x_3 x_1, x_2) \cdots f(x_t x_1, \dots, x_{t-1})$.	13
4.1 Probability density function (PDF) of the gamma distribution with varying shape and rate parameters	23
5.1 MCMC Algorithm for Parameter Estimation for Gamma MTD Models	25
6.1 (a), (b) Results for Scenarios 1 and 1.2: default setup; (c), (d) Scenarios 1.3 and 1.4: incompatible weight and dependence; (e), (f) Scenarios 1.5 and 1.6: compatible, but rarely observed patterns. (Left) Dashed lines are true weights, dot-dashed lines are prior means, solid lines are posterior means, and polygons are 95% posterior credible intervals. (Right) Dashed (black) lines are true dependence, dot-dashed (red) lines are prior means, solid (blue) lines are posterior means, and (purple) polygons are 95% posterior credible intervals.	32
6.2 Examples of Prior Distributions for Scenario 1: (a) Priors for α , with the true value equal to 7, and (b) priors for β , with the true value equal to 1.	35
6.3 Coverage Rates for α and β Across 40 Replicates for Scenario 1.	36
6.4 Coverage Rates for w and ρ Across 40 Replicates for Scenario 1.	37
7.1 95% one-step ahead posterior predictive intervals for (a) Gamma Scenario 1 and (b) Scenario 2.	39

LIST OF FIGURES (Continued)

<u>Figure</u>	<u>Page</u>
11.1 (a), (b): $ZIGamma(\mu = 7, \beta = 1, P = 0.1, \epsilon = 0.1, 0.4)$; (c), (d): $ZIGamma(\mu = 7, \beta = 1, P = 0.5, \epsilon = 0.1, 0.4)$; (e), (f): $ZIGamma(\mu = 7, \beta = 1, P = 0.7, \epsilon = 0.1, 0.4)$. (Left) Probability density function (PDF) and (Right) cumulative distribution function (CDF) of the zero-inflated gamma distribution with varying parameters.	57
12.1 MCMC Algorithm for Parameter Estimation for Zero-Inflated Gamma MTD Models	61
13.1 (a), (b) Results for Scenarios 1 and 2: default setup for w and ρ ($P = 0.1$ and $\epsilon = 0.1$). (Left) Dashed (black) lines are true weights, dot-dashed (red) lines are prior means, solid lines are posterior means, and (purple) polygons are 95% posterior credible intervals. (Right) Dashed (black) lines are true dependence, dot-dashed (red) lines are prior means, solid (blue) lines are posterior means, and (purple) polygons are 95% posterior credible intervals.	68
14.1 95% one-step ahead posterior predictive intervals for ZIGamma Scenario 1 (varying P and ϵ). Reported values show overall empirical coverage, with decomposed coverage below and above the threshold shown in parentheses: coverage (coverage for data $\leq \epsilon$, coverage for data $> \epsilon$).	75
14.2 95% one-step ahead posterior predictive intervals for ZIGamma Scenario 2 (varying P and ϵ). Reported values show overall empirical coverage, with decomposed coverage below and above the threshold shown in parentheses: coverage (coverage for data $\leq \epsilon$, coverage for data $> \epsilon$).	76
17.1 Architecture of an RNN unit, reproduced from Olah (2015). x_t is the input, h_t is the hidden state, and o_t is the output. $tanh$ is the activation function, squashing values to $(-1, 1)$ for stability and zero-centered output.	83
17.2 Architecture of an LSTM unit with a forget gate, reproduced from Olah (2015). x_t is the input, h_t the hidden state, and c_t the cell state. f_t , i_t , and o_t are the forget, input, and output gates, respectively. σ is used to squash values to $(0, 1)$ for gating, while $tanh$ squashes values to $(-1, 1)$ for stability and zero-centered output.	88

LIST OF FIGURES (Continued)

Figure	Page
18.1 One-step-ahead predicted means for (a) Gamma Scenario 1 and (b) Scenario 2: Solid (black) lines are true values. Dashed (red) lines are LSTM predicted means and dashed (blue) lines are MTD predicted means.	100
18.2 Zoomed-in view of one-step ahead predicted means for (a) Gamma Scenario 1 and (b) Scenario 2: Solid (black) lines are true values. Dashed (red) lines are LSTM predicted means and dashed (blue) lines are MTD predicted means.	100
18.3 Relative Performance of LSTM and MTD models for Gamma Scenario 1 (Mean RMSE for LSTM = 1.5290; Mean RMSE for MTD = 1.4000). Data points are connected by lines to indicate results from the same replicate.	101
18.4 Relative performance of LSTM networks with varying learning rates (0.1, 0.01, 0.001), batch sizes (1, 8, 16, 32, 64, 128), number of layers (1–3), and cell dimensions (32, 64, 128) for Gamma Scenario 1.	103
18.5 One-step ahead predicted means for ZIGamma Scenario 1: Solid (black) lines are true values. Dashed (red) lines are LSTM predicted means and dashed (blue) lines are MTD predicted means. Reported values show overall RMSE, with decomposed RMSE below and above the threshold shown in parentheses: RMSE (RMSE for data $\leq \epsilon$, RMSE for data $> \epsilon$).	107
18.6 Zoomed-in view of one-step ahead predicted means for ZIGamma Scenario 1: Solid (black) lines are true values. Dashed (red) lines are LSTM predicted means and dashed (blue) lines are MTD predicted means. Reported values show overall RMSE, with decomposed RMSE below and above the threshold shown in parentheses: RMSE (RMSE for data $\leq \epsilon$, RMSE for data $> \epsilon$).	108
19.1 Time series plot of observed hourly wind speeds (m/s) at heights of (a) 50 m, (b) 10 m, and (c) 2 m above ground level at the Limon Wind Energy Center, Colorado, for the year 2024. Data sourced from MERRA-2 via the NASA GES DISC Earthdata API.	110
19.2 One-step ahead predicted means for wind speeds (m/s) at heights of (a) 50 m, (b) 10 m, and (c) 2 m above ground level: Solid (black) lines are true values. Dashed (red) lines are LSTM predicted means and dashed (blue) lines are MTD predicted means.	115

LIST OF FIGURES (Continued)

<u>Figure</u>	<u>Page</u>
19.3 Zoomed-in view of one-step ahead predicted means for wind speeds (m/s) at (a) 50 m, (b) 10 m, and (c) 2 m above ground level for $n = 200$. Solid (black) lines represent true values. Dashed (red) lines are LSTM predictions; dashed (blue) lines are MTD predictions.	116
19.4 One-step ahead prediction errors for wind speeds (m/s) at heights of (a) 50 m, (b) 10 m, and (c) 2 m above ground level: Dashed (red) lines show differences between LSTM predicted means and observed values and dashed (blue) lines show differences between MTD predicted means and observed values.	117
19.5 Zoomed-in view of one-step ahead prediction errors for wind speeds (m/s) at heights of (a) 50 m, (b) 10 m, and (c) 2 m above ground level: Dashed (red) lines show differences between LSTM predicted means and observed values and dashed (blue) lines show differences between MTD predicted means and observed values.	118
19.6 95% one-step ahead posterior predictive intervals for wind speeds (m/s) at heights of (a) 50 m, (b) 10 m, and (c) 2 m above ground level for look-back steps $L = 5$	120
19.7 95% one-step ahead posterior predictive intervals for wind speeds (m/s) at heights of (a) 50 m, (b) 10 m, and (c) 2 m above ground level for look-back steps $L = 15$	121

LIST OF TABLES

Table	Page
6.1 Description of Scenarios for Gamma Model	27
6.2 Summary of Scenarios for Gamma Model	27
6.3 Estimates and Gelman-Rubin Diagnostics for Scenario 1's w at Each Lag	29
6.4 Estimates and Gelman-Rubin Diagnostics for Scenario 1's ρ at Each Lag	29
6.5 Estimates and Gelman-Rubin Diagnostics for Scenario 1's α, β	29
6.6 Results for Scenario 3-6	33
6.7 Results for Scenario 7-9	33
6.8 Setups and Prior Specifications for Scenario 1: α and β	34
6.9 Coverage Rates for All Parameters Across 40 Replicates for Scenario 1.	36
6.10 Coverage Rates for All Parameters Across 40 Replicates for Scenario 2.	36
 7.1 Empirical coverage of the 95% predictive intervals for Gamma Scenario 1-9 (s1-s9).	 38
 13.1 Description of Scenarios for Zero-Inflated Gamma Model	 63
13.2 Summary of Scenarios for Zero-Inflated Gamma Model	63
13.3 Estimates and Gelman-Rubin Diagnostics for Scenario 1's w at Each Lag ($P = 0.1$ and $\epsilon = 0.1$)	65
13.4 Estimates and Gelman-Rubin Diagnostics for Scenario 1's ρ at Each Lag ($P = 0.1$ and $\epsilon = 0.1$)	65
13.5 Estimates and Gelman-Rubin Diagnostics for Scenario 1 (varying P and ϵ), with true parameter values fixed at $\mu = 7$ and $\beta = 1$. The table includes all combinations of $P = 0.1, 0.5, 0.7$ and $\epsilon = 0.1, 0.4$. Specifically, the top two rows correspond to $P = 0.1$ with $\epsilon = 0.1$ and 0.4 ; the middle two rows to $P = 0.5$ with $\epsilon = 0.1$ and 0.4 ; and the final two rows to $P = 0.7$ with $\epsilon = 0.1$ and 0.4	66

LIST OF TABLES (Continued)

Table	Page
13.6 Estimates and Gelman–Rubin Diagnostics for Scenario 3 (varying P and ϵ), with true parameter values fixed at $\mu = 4$ and $\beta = 1$. The table includes all combinations of $P = 0.1, 0.5, 0.7$ and $\epsilon = 0.1, 0.4$. Specifically, the top two rows correspond to $P = 0.1$ with $\epsilon = 0.1$ and 0.4 ; the middle two rows to $P = 0.5$ with $\epsilon = 0.1$ and 0.4 ; and the final two rows to $P = 0.7$ with $\epsilon = 0.1$ and 0.4 .	70
13.7 Estimates and Gelman–Rubin Diagnostics for Scenario 7 (varying P and ϵ), with true parameter values fixed at $\mu = 2$ and $\beta = 1$. The table includes all combinations of $P = 0.1, 0.5, 0.7$ and $\epsilon = 0.1, 0.4$. Specifically, the top two rows correspond to $P = 0.1$ with $\epsilon = 0.1$ and 0.4 ; the middle two rows to $P = 0.5$ with $\epsilon = 0.1$ and 0.4 ; and the final two rows to $P = 0.7$ with $\epsilon = 0.1$ and 0.4 .	71
13.8 Coverage Rates for All Parameters Across 40 Replicates for Scenario 1 (varying P and ϵ), with true parameter values fixed at $\mu = 7$ and $\beta = 1$. The table includes all combinations of $P = 0.1, 0.5, 0.7$ and $\epsilon = 0.1, 0.4$. Specifically, the top two rows correspond to $P = 0.1$ with $\epsilon = 0.1$ and 0.4 ; the middle two rows to $P = 0.5$ with $\epsilon = 0.1$ and 0.4 ; and the final two rows to $P = 0.7$ with $\epsilon = 0.1$ and 0.4 .	72
13.9 Coverage Rates for All Parameters Across 40 Replicates for Scenario 2 (varying P and ϵ), with true parameter values fixed at $\mu = 7$ and $\beta = 1$. The table includes all combinations of $P = 0.1, 0.5, 0.7$ and $\epsilon = 0.1, 0.4$. Specifically, the top two rows correspond to $P = 0.1$ with $\epsilon = 0.1$ and 0.4 ; the middle two rows to $P = 0.5$ with $\epsilon = 0.1$ and 0.4 ; and the final two rows to $P = 0.7$ with $\epsilon = 0.1$ and 0.4 .	72
14.1 Empirical coverage of the 95% predictive intervals for ZIGamma Scenario 1 (varying P and ϵ). Each row label indicates the combination of P (zero-inflated probability) and ϵ (threshold value) used in the simulation. Reported values show overall empirical coverage, with decomposed coverage below and above the threshold.	74
14.2 Empirical coverage of the 95% predictive intervals for ZIGamma Scenario 2 (varying P and ϵ). Each row label indicates the combination of P (zero-inflated probability) and ϵ (threshold value) used in the simulation. Reported values show overall empirical coverage, with decomposed coverage below and above the threshold.	74

LIST OF TABLES (Continued)

Table	Page
17.1 Common metrics for evaluating forecasting models.	94
18.1 RMSE Comparison of LSTM and MTD for Gamma Scenarios 1–9 (s1–s9).	99
18.2 Bias Comparison of LSTM and MTD for Gamma Scenarios 1–9 (s1–s9).	99
18.3 RMSE Comparison of LSTM and MTD for ZIGamma Scenarios 1. Each row label indicates the combination of P (zero-inflated probability) and ϵ (threshold value) used in the simulation.	105
18.4 RMSE Comparison of LSTM and MTD for ZIGamma Scenarios 1 Above and Below. Each row label indicates the combination of P (zero-inflated probability) and ϵ (threshold value) used in the simulation. Reported values show decomposed RMSE below and above the threshold.	105
18.5 Bias Comparison of LSTM and MTD for ZIGamma Scenarios 1. Each row label indicates the combination of P (zero-inflated probability) and ϵ (threshold value) used in the simulation.	106
18.6 Bias Comparison of LSTM and MTD for ZIGamma Scenarios 1 Above and Below. Each row label indicates the combination of P (zero-inflated probability) and ϵ (threshold value) used in the simulation. Reported values show overall RMSE, with decomposed RMSE below and above the threshold.	106
19.1 Comparison of LSTM and MTD for predicting wind speeds (m/s) at 50 m above ground level.	112
19.2 Comparison of LSTM and MTD for predicting wind speeds (m/s) at 10 m above ground level.	113
19.3 Comparison of LSTM and MTD for predicting wind speeds (m/s) at 2 m above ground level.	113
19.4 Comparison of LSTM and MTD with 5 vs. 15 look-back steps for predicting wind speeds (m/s) at 50 m above ground level. W denotes the LSTM input window size and L denotes the MTD order; both represent look-back steps.	114
19.5 Comparison of LSTM and MTD with 5 vs. 15 look-back steps for predicting wind speeds (m/s) at 10 m above ground level. W denotes the LSTM input window size and L denotes the MTD order; both represent look-back steps.	114

LIST OF TABLES (Continued)

<u>Table</u>		<u>Page</u>
19.6	Comparison of LSTM and MTD with 5 vs. 15 look-back steps for predicting wind speeds (m/s) at 2 m above ground level. W denotes the LSTM input window size and L denotes the MTD order; both represent look-back steps.	114
19.7	Empirical coverage of the 95% predictive intervals for wind speeds (m/s), with look-back steps $L = 5$ vs 15.	119

LIST OF ALGORITHMS

<u>Algorithm</u>	<u>Page</u>
------------------	-------------

LIST OF APPENDICES

<u>Appendix</u>	<u>Page</u>
A PDF and CDF Plots for Zero-Inflated Gamma MTD Models	150
B Simulations for Gamma MTD Models	152
C Simulations for Zero-Inflated Gamma MTD Models	161
D Predictions for Gamma MTD Models	173
E Predictions for Zero-Inflated Gamma MTD Models	175
F Predictions for MTD Models vs LSTM Networks	183
G <code>mtd</code> : An R Package for Modeling Gamma and Zero-inflated Gamma Time Series .	191

LIST OF APPENDIX FIGURES

Figure	Page
A.1 (a), (b): $ZIGamma(\mu = 7, \beta = 1, P = 0.1, \epsilon = 0.1, 0.4)$; (c), (d): $ZIGamma(\mu = 7, \beta = 1, P = 0.5, \epsilon = 0.1, 0.4)$; (e), (f): $ZIGamma(\mu = 7, \beta = 1, P = 0.7, \epsilon = 0.1, 0.4)$. (Left) Probability density function (PDF) and (Right) cumulative distribution function (CDF) of the zero-inflated gamma distribution with varying parameters.	151
B.1 (Left) Gelman-Rubin and (Right) ACF plot for Scenario 1's w	153
B.2 (Left) Gelman-Rubin and (Right) ACF plot for Scenario 1's ρ	154
B.3 (Left) Gelman-Rubin and (Right) ACF plot for Scenario 1's α, β	155
B.4 (Left) Trace and (Right) density plot for Scenario 1's w	156
B.5 (Left) Trace and (Right) density plot for Scenario 1's ρ	157
B.6 (Left) Trace and (Right) density plot for Scenario 1's α, β	158
B.7 Results for Scenario 3-6. Grey bars are histogram of the data. Circles are the true gamma density evaluated at the support, i.e., $x > 0$. Solid lines are the posterior means. Dashed lines are 95% credible intervals.	159
B.8 Results for Scenario 7-9. Grey bars are histogram of the data. Circles are the true gamma density evaluated at the support, i.e., $x > 0$. Solid lines are the posterior means. Dashed lines are 95% credible intervals.	160
C.1 (Left) Gelman-Rubin and (Right) ACF plot for Scenario 1's w	162
C.2 (Left) Gelman-Rubin and (Right) ACF plot for Scenario 1's ρ	163
C.3 (Left) Gelman-Rubin and (Right) ACF plot for Scenario 1's μ, β, P, ϵ	164
C.4 (Left) Trace and (Right) density plot for Scenario 1's w	165
C.5 (Left) Trace and (Right) density plot for Scenario 1's ρ	166
C.6 (Left) Trace and (Right) density plot for Scenario 1's μ, β, P, ϵ	167
C.7 Simulated data for Scenario 1. Grey bars are histogram of the data. Black bar is the zero-inflated probability.	168

LIST OF APPENDIX FIGURES (Continued)

<u>Figure</u>		<u>Page</u>
C.8 Results for Scenario 1. Grey bars are histogram of the data. Circles are the true gamma density evaluated at the support, i.e., $x > 0$. Solid lines are the posterior means. Dashed lines are 95% credible intervals. Red bar is the zero-inflated probability.		169
D.1 95% one-step ahead posterior predictive intervals for (a) Gamma Scenario 3, (b) Scenario 4, (c) Scenario 5, and (d) Scenario 6.		173
D.2 95% one-step ahead posterior predictive intervals for (a) Gamma Scenario 7, (b) Scenario 8, and (c) Scenario 9.		174
E.1 95% one-step ahead posterior predictive intervals for ZIGamma Scenario 3. Reported values show overall empirical coverage, with decomposed coverage below and above the threshold shown in parentheses: coverage (coverage for data $\leq \epsilon$, coverage for data $> \epsilon$).		176
E.2 95% one-step ahead posterior predictive intervals for ZIGamma Scenario 4. Reported values show overall empirical coverage, with decomposed coverage below and above the threshold shown in parentheses: coverage (coverage for data $\leq \epsilon$, coverage for data $> \epsilon$).		177
E.3 95% one-step ahead posterior predictive intervals for ZIGamma Scenario 5. Reported values show overall empirical coverage, with decomposed coverage below and above the threshold shown in parentheses: coverage (coverage for data $\leq \epsilon$, coverage for data $> \epsilon$).		178
E.4 95% one-step ahead posterior predictive intervals for ZIGamma Scenario 6. Reported values show overall empirical coverage, with decomposed coverage below and above the threshold shown in parentheses: coverage (coverage for data $\leq \epsilon$, coverage for data $> \epsilon$).		179
E.5 95% one-step ahead posterior predictive intervals for ZIGamma Scenario 7. Reported values show overall empirical coverage, with decomposed coverage below and above the threshold shown in parentheses: coverage (coverage for data $\leq \epsilon$, coverage for data $> \epsilon$).		180

LIST OF APPENDIX FIGURES (Continued)

<u>Figure</u>		<u>Page</u>
E.6 95% one-step ahead posterior predictive intervals for ZIGamma Scenario 8. Reported values show overall empirical coverage, with decomposed coverage below and above the threshold shown in parentheses: coverage (coverage for data $\leq \epsilon$, coverage for data $> \epsilon$).	181	
E.7 95% one-step ahead posterior predictive intervals for ZIGamma Scenario 9. Reported values show overall empirical coverage, with decomposed coverage below and above the threshold shown in parentheses: coverage (coverage for data $\leq \epsilon$, coverage for data $> \epsilon$).	182	
F.1 One-step ahead predicted means for Gamma Scenario 3, 4, 5, 6: Solid (black) lines are true values. Dashed (red) lines are LSTM predicted means and dashed (blue) lines are MTD predicted means.	184	
F.2 One-step ahead predicted means for Gamma Scenario 7, 8, 9: Solid (black) lines are true values. Dashed (red) lines are LSTM predicted means and dashed (blue) lines are MTD predicted means.	185	
F.3 One-step ahead predicted means for Gamma Scenario 2: Solid (black) lines are true values. Dashed (red) lines are LSTM predicted means and dashed (blue) lines are MTD predicted means. Reported values show overall RMSE, with decomposed RMSE below and above the threshold shown in parentheses: RMSE (RMSE for data $\leq \epsilon$, RMSE for data $> \epsilon$).	187	
F.4 Zoomed-in view of one-step ahead predicted means for ZIGamma Scenario 2: Solid (black) lines are true values. Dashed (red) lines are LSTM predicted means and dashed (blue) lines are MTD predicted means. Reported values show overall RMSE, with decomposed RMSE below and above the threshold shown in parentheses: RMSE (RMSE for data $\leq \epsilon$, RMSE for data $> \epsilon$). . .	188	
F.5 Training and validation loss curves for the LSTM model. Columns (left to right) correspond to wind speeds at 50 m, 10 m, and 2 m above ground level, respectively. Rows (top to bottom) correspond to batch sizes 8, 16, and 32, respectively.	189	
F.6 Training and validation loss curves for the LSTM model. Columns (left to right) correspond to wind speeds at 50 m, 10 m, and 2 m above ground level, respectively. Rows (top to bottom) correspond to batch sizes 64, 128, and 256, respectively.	190	

LIST OF APPENDIX TABLES

Table	Page
C.1 Estimates and Gelman–Rubin Diagnostics for Scenario 1 ($P = 0.1, \epsilon = 0.1$) for parameters w, ρ, μ, β, P , and ϵ	170
C.2 Estimates and Gelman–Rubin Diagnostics for Scenario 2 ($P = 0.1, \epsilon = 0.1$) for parameters w, ρ, μ, β, P , and ϵ	170
C.3 Estimates and Gelman–Rubin Diagnostics for Scenario 1 (varying P, ϵ) for parameters μ, β, P , and ϵ	171
C.4 Estimates and Gelman–Rubin Diagnostics for Scenario 2 (varying P, ϵ) for parameters μ, β, P , and ϵ	172
F.1 RMSE Comparison of LSTM and MTD for ZIGamma Scenarios 2. Each row label indicates the combination of P (zero-inflated probability) and ϵ (threshold value) used in the simulation.	183
F.2 RMSE Comparison of LSTM and MTD for ZIGamma Scenarios 2 Above and Below. Each row label indicates the combination of P (zero-inflated probability) and ϵ (threshold value) used in the simulation. Reported values show overall RMSE, with decomposed RMSE below and above the threshold.	185
F.3 Bias Comparison of LSTM and MTD for ZIGamma Scenarios 2. Each row label indicates the combination of P (zero-inflated probability) and ϵ (threshold value) used in the simulation.	186
F.4 Bias Comparison of LSTM and MTD for ZIGamma Scenarios 2 Above and Below. Each row label indicates the combination of P (zero-inflated probability) and ϵ (threshold value) used in the simulation. Reported values show overall RMSE, with decomposed RMSE below and above the threshold.	186

Chapter 1: Introduction

1.1 Motivation and Objective

Modeling complex patterns in sequence data is a central task across domains such as energy, insurance, and transportation. Real-world time series often exhibit skewness and zero-inflation, which, if unaddressed, undermine prediction accuracy. For example, wind speeds are typically skewed, while medical expenditures, insurance claims, and transportation safety measures may also include an excess of zeros. These features highlight the need for flexible models capable of capturing both continuous skewed behavior and semicontinuous, zero-inflated structures. Figure 1.1 and Figure 1.2 illustrate the skewed and zero-inflated time series that motivate the design choices.

Recent advances in artificial intelligence (AI) have introduced powerful deep learning architectures, particularly Recurrent Neural Networks (RNNs) and Long Short-Term Memory (LSTM) networks. These models effectively capture nonlinear and long-range dependence in data, offering fast predictions without explicit probabilistic assumptions. Nevertheless, claims of LSTM superiority can be misleading when compared against inappropriate benchmarks such as ARIMA models. In addition, prior work has found comparable predictive performance between probabilistic Mixture Transition Distribution (MTD) model and deep learning LSTM network for disease spread. These considerations motivate a more rigorous

comparison of deep learning approaches with flexible probabilistic models designed to handle nonlinear, non-Gaussian, and zero-inflated dynamics, providing a more realistic benchmark than traditional methods.

While deep learning methods offer powerful predictive capabilities, classical statistical approaches remain indispensable, especially when robustness, interpretability, and uncertainty quantification are priorities. We propose the Gamma Mixture Transition Distribution (Gamma MTD) and the Zero-Inflated Gamma MTD (ZIGamma MTD) models, which extend the traditional MTD framework through a copula-based formulation. These models provide flexible and interpretable frameworks for skewed and zero-inflated time series, enabling accurate representation of both continuous and semicontinuous dynamics commonly observed in real-world applications, while also allowing a fair comparison with deep learning methods such as LSTMs.

This dissertation develops the Gamma MTD and ZIGamma MTD models, evaluates their predictive performance and robustness, and compares them with modern deep learning approaches such as LSTMs. By integrating insights from both probabilistic and AI-driven frameworks, this work highlights their complementary strengths and limitations, providing a clearer picture of their practical applications. We expand on these points in the sections that follow.

1.2 Data Challenges

To account for skewness and zero-inflation commonly observed in real-world time series, we develop a copula-based Gamma MTD model and its zero-inflated extension, ZIGamma MTD, providing a robust, flexible, and interpretable framework for modeling such data type.

The Gamma MTD model extends the original MTD framework by incorporating copulas into the transition kernels. This allows the dependence structure to be modeled separately from the marginal distributions, enabling the selection of copula families that effectively capture complex dependence while maintaining flexibility in the choice of marginals. As a result, the model offers enhanced modeling capabilities and greater adaptability to diverse data characteristics.

The ZIGamma MTD model further extends the copula-based Gamma MTD to handle zero-inflated data by reconstructing the marginal distribution. By transforming semi-continuous distributions into fully continuous ones, this approach overcomes the challenges posed by non-continuity in the copula approach. As a result, the model preserves its effectiveness in modeling dependence structures while retaining flexibility in the choice of marginals.

By developing and evaluating the Gamma MTD and ZIGamma MTD models, this work aims to provide a robust and flexible framework for modeling complex time series, addressing both skewness and zero-inflation while preserving interpretability and effectiveness.

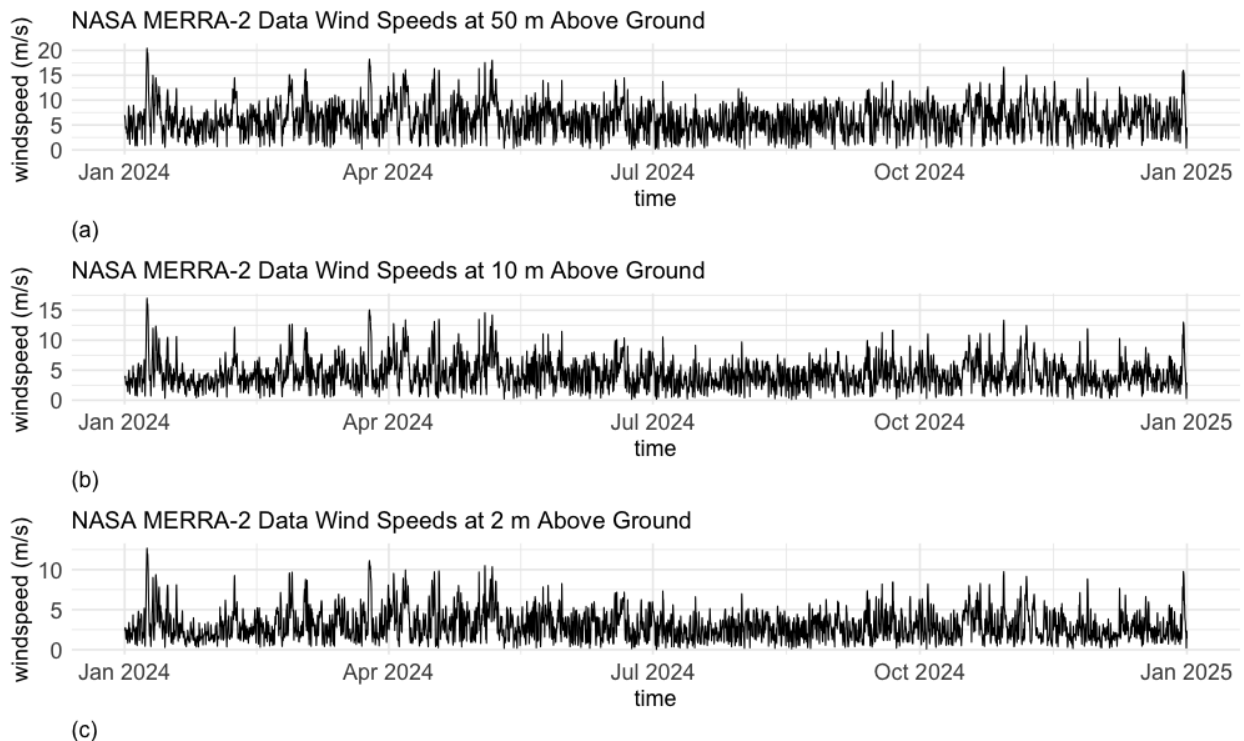


Figure 1.1: Time series plot of observed hourly wind speeds (m/s) at heights of (a) 50 m, (b) 10 m, and (c) 2 m above ground level at the Limon Wind Energy Center, Colorado, for the year 2024. Data sourced from MERRA-2 via the NASA GES DISC Earthdata API.

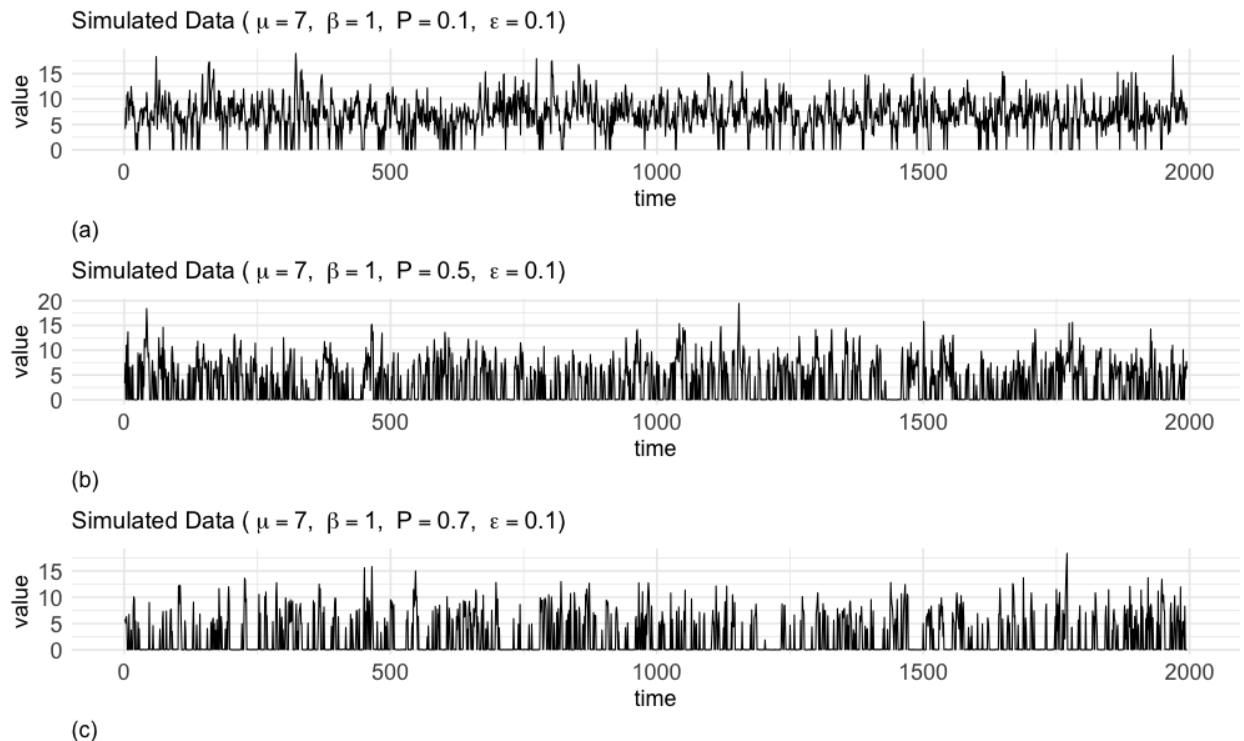


Figure 1.2: Time series plot of observed values for varying zero-inflated probability (a) $P = 0.1$, (b) $P = 0.5$, and (c) $P = 0.7$. Data generated from a ZIGamma MTD model with mean, scale, and threshold parameters $\mu = 7$, $\beta = 1$, and $\epsilon = 0.1$.

1.3 Modeling Approaches

To ensure a fair and balanced evaluation, we examine two complementary modeling approaches: probabilistic MTD models and deep learning methods, such as LSTM networks.

MTD models represent each conditional distribution as a mixture of l transition kernels, weighting past lags probabilistically to capture complex temporal dependence. They are particularly effective for non-Gaussian, skewed, and zero-inflated data. The copula-based formulation further enhances their ability to model continuous and semicontinuous patterns.

Recurrent Neural Network (RNN) architectures, including LSTMs, model temporal dependence by propagating recurrent units over time. These networks learn internal states directly from data using backpropagation through time (BPTT) without relying on explicit probabilistic assumptions. LSTMs efficiently capture long-range nonlinear dependence, making them well-suited for fast prediction on large-scale datasets.

Although both MTD models and LSTMs describe evolving dynamics, they differ fundamentally. MTD models employ probabilistic transition mechanisms, whereas LSTMs rely on deterministic, learned transformations of hidden and cell states. This distinction has practical implications: MTD models tend to provide higher predictive accuracy, improved robustness, and greater interpretability, but at greater computational cost and with more complex model design. LSTMs offer faster predictions and simpler deployment, but with lower interpretability and potentially reduced accuracy.

By combining insights from both classical and AI-driven frameworks, this work aims to

provide practical guidance for modeling time series with complex, skewed, and zero-inflated patterns.

1.4 Outline of the Dissertation Chapters

The rest of the dissertation is organized as follows. In Part I, we propose the copula-based Gamma MTD model, detailing its design, estimation procedures, and predictive performance. In Part II, we extend this framework to accommodate zero-inflated time series with the ZIGamma MTD model, covering similar aspects of design, estimation, and prediction. In Part III, we compare the MTD models with deep learning approaches, specifically the Long Short-Term Memory (LSTM) networks, evaluating predictive performance and robustness through simulation studies and real-world data applications.

Part I

Models for Forecasting Skewed Time Series

Chapter 2: Introduction

Time series data consist of observations measured at regular time intervals. In these data types, observations often exhibit temporal dependence; that is, observations from recent time lags tend to be similar. Examples of time series data are sensor readings, stock prices, sale figures, energy production, weather data, and various other metrics.

Time series models capture how past values contribute to the current value and use this information to predict future values. In the autoregressive (AR) model with order p , for example, each current value depends on all p past values, with fixed, deterministic weights. The mixture transition distribution (MTD) model extends the AR models to accommodate discrete, continuous, and mixed time series, expanding its range of applications. The MTD model models each conditional distribution as a mixture of transition kernels, with random, stochastic weights.

The first MTD model was developed in 1985 to model high-order Markov chains ([Raftery 1985a, 1985b](#)), followed by several variant models over the years. Our work builds upon the architecture of the MTD model introduced in 2022 by Zheng et al. ([2022](#)). This model includes various applications, such as the Gaussian MTD, Poisson MTD, negative binomial MTD, and Lomax MTD regression models, extending beyond linear, Gaussian dynamics. However, there are two limitations. First, under this model framework, the transition kernel

lacks component-varying parameters. Second, for certain invariant marginal distributions, the transition kernel may either require careful construction or can result in a form that is not explicitly defined or too complex.

We propose to incorporate copulas into the transition kernels to address the second limitation. Using copulas, dependence structures and marginal distributions can be modeled separately, enabling a choice of copula families that effectively capture data's dependence while allowing flexibility in marginal selection. The proposed copula-based MTD model enables flexible dependence modeling and accommodates any continuous marginals, thereby enhancing modeling capabilities and flexibility.

The rest of the chapter is organized as follows. We review the MTD model developed by Zheng et al. (2022) in Chapter 3. We present the proposed model in Chapter 4 and provide an overview of the MCMC algorithm for parameter estimation in Chapter 5. We present the results of various simulations conducted to assess the accuracy and performance of the proposed model in Chapter 6 and discuss the model's predictive capabilities, including uncertainty quantification, in Chapter 7. Finally, we conclude with a discussion in Chapter 8. Appendix G provides the instruction for installing the extended `mtd` R package.

Chapter 3: Background

The MTD model is a state space model. The MTD model was initially developed in 1985 to model high-order Markov chains ([Raftery 1985a, 1985b](#)). On a finite state space, the model offers a parsimonious approximation of higher-order Markov chains. On a more general state space, the model can capture non-Gaussian and nonlinear features, such as flat stretches, bursts, outliers, and change points ([Raftery 1994; Le et al. 1996](#)). The class of MTD models and their generalizations have diverse applications, including wind power forecasting, social behavior analysis, DNA sequence modeling, and forecasting of stock prices and inflation rates. A complete review of the MTD model and its applications can be found in Berchtold and Raftery ([2002](#)). Recent applications extend to the modeling of crime incidents and precipitation patterns ([Zheng et al. 2022](#)) and the network analysis of financial markets ([D'Amico et al. 2023](#)). Although the MTD model has primarily been used for modeling time series, its generalizations has also demonstrated success in modeling spatial data. Some applications within the spatial context can be found in Berchtold ([2001](#)), Zheng et al. ([2023b](#)), and Zheng et al. ([2023a](#)).

3.1 Mixture Transition Distribution Models for Time Series

In the general MTD model framework, the joint data distribution over a directed acyclic graph (DAG) is modeled as a weighted combination of first-order component densities or

transition kernels. A DAG simplifies complex relationships in the data, enabling flexible and parsimonious multivariate non-Gaussian modeling. Let $\{X_t : t \in \mathbb{N}\}$ be a time series, represented by a sequence of random variables in an arbitrary state space and $f(\mathbf{x})$, where $\mathbf{x} = (X_1, \dots, X_t)^T$, be the joint distribution of X_1 to X_t . By applying the chain rule of probability theory and constructing the model on a DAG, the joint distribution of X_1 to X_t can be factorized into a product of conditional distributions as

$$f(\mathbf{x}) = f(x_1) \prod_{t=2}^t f(x_t | \mathbf{x}^{t-1}). \quad (3.1)$$

$f(x_t | \mathbf{x}^{t-1})$ is the conditional probability density function (pdf) of current value X_t given all of its past values $\mathbf{X}^{t-1} = \mathbf{x}^{t-1}$, where $\mathbf{X}^{t-1} = \{X_i : i \leq t-1\}$ and $\mathbf{x}^{t-1} = \{x_i : i \leq t-1\}$. The joint distribution in (3.1) corresponds to a directed graphical model (Jordan (2004); also known as a Bayesian network), where the conditional independence structure among the random variables is encoded by a DAG. Figure 3.1 and 3.2 provide visual illustrations of the linear and directed relationships between X_1 through X_t on a DAG, respectively. In Figure 3.2, let X_1, \dots, X_t be vertices or nodes in a graph. The set \mathbf{X}^{t-1} , which consists of nodes that have directed edges pointed to X_t , is called the parent or conditioning set of X_t .

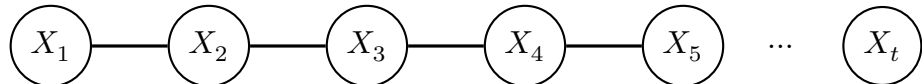


Figure 3.1: Relationships between $X_1, X_2, X_3, X_4, X_5, \dots, X_t$. The joint distribution is $f(\mathbf{x}) = f(x_1, x_2, x_3, \dots, x_t)$.

As t increases, the size of the conditioning set of X_t can become notably large. Zheng et al. (2022) address the challenge of modeling a non-Gaussian conditional density with a high-

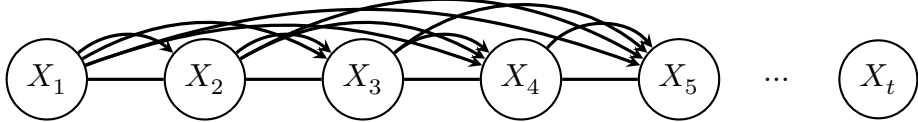


Figure 3.2: Directed relationships between $X_1, X_2, X_3, X_4, X_5, \dots, X_t$ on a DAG. The joint distribution is factored as $f(\mathbf{x}) = f(x_1)f(x_2|x_1)f(x_3|x_1, x_2)\cdots f(x_t|x_1, \dots, x_{t-1})$.

dimensional conditioning set using the structured mixture model. When the order of the MTD model is set to $L \ll t$, the conditioning set of x_t is reduced to $\{x_{t-L}, \dots, x_{t-1}\} \subset \{x_1, \dots, x_{t-1}\}$. Consequently, in Figure 3.2, the number of directed edges pointing to each X_t is reduced to at most L . Each current value in the MTD model references only to the L lagged values, rather than the entire history of the time series.

Each conditional in (3.1) is modeled as a mixture of L transition kernels, with mixture weights. Transition kernels, similar to transition probabilities in discrete-valued time series, describe how a probability distribution moves from one state to another in a stochastic process, but applied to continuous or more general state spaces. Transition kernels represent the influence of the l th lag value on the current value. Mixture weights indicate the contribution of that influence. Let $\{X_t : t \in \mathbb{N}\}$ be a time series, represented by a sequence of random variables in an arbitrary state space. For $t > L$, the MTD model specifies the conditional distribution of X_t given $\mathbf{X}^{t-1} = \mathbf{x}^{t-1}$ as

$$f(x_t|\mathbf{x}^{t-1}) = \sum_{l=1}^L w_l f_l(x_t|x_{t-l}). \quad (3.2)$$

$f_l(x_t|x_{t-l})$ is the conditional pdf of X_t with respect to the l th transition kernel given that

$X_{t-l} = x_{t-l}$. w_l are weight parameters, where $w_l \geq 0$ such that $\sum_{l=1}^L w_l = 1$. Transition kernels in (3.2) capture dependence between the current value and its lag values. Weight parameters assign specific weights to the transition kernels, determining the relative contribution of the lagged values' influence. We will expand the discussion of transition kernels and mixture weights in the next section.

3.2 Model Construction

Earlier MTD models were built using frequentist approaches. Estimation and prediction in the MTD model by Zheng et al. (2022) is constructed with a focus on Bayesian methodologies.

3.2.1 Mixture Weights

Zheng et al. (2022) consider three weight types: weights with a uniform Dirichlet prior, a truncated version of the stick-breaking prior, and the cdf-based Dirichlet process prior. We use the weight with the cdf-based prior, which will be the focus of our discussion.

Let $x_k \in [0, 1]$ with $\sum_{k=1}^K x_k = 1$. The Dirichlet distribution, denoted as $Dirichlet(\alpha)$, is a discrete distribution on $[0, 1]^K$. It is characterized by a vector of concentration parameters α , where $\alpha_k > 0$, and the mean of x_k is $\alpha_k / \sum_{k=1}^K \alpha_k$, for $k = 1, \dots, K$. The Dirichlet process, denoted as $DP(\alpha, G)$, is a discrete distribution over probability distributions. The Dirichlet process generates a distribution that shrinks around a base distribution G , with the degree of shrinkage controlled by a concentration parameter α . The base distribution determines the form of the distribution generated by the Dirichlet process, and the concentration parameter

controls the degree of shrinkage of the resulting distribution toward the base distribution.

The weight associated with a cdf-based Dirichlet process prior assumes that the weights are increments of a cdf G . This prior is denoted as $CDP(\cdot|1_L/L)$, where 1_L is a unit vector of length L . It is constructed as follows. First assume that the weights are increments of a cdf G on the support $[0, 1]$; that is,

$$w_l = G(l/L) - G((l-1)/L), \quad l = 1, \dots, L. \quad (3.3)$$

Next place a Dirichlet process prior on G , denoted as $DP(\alpha_0, G_0)$, where $\alpha_0 > 0$ and $G_0 = Beta(a_0, b_0)$. Then the vector of weights follows a Dirichlet distribution with parameter vector $\alpha_0(a_1, \dots, a_L)^T$, where $\alpha_0 > 0$ and $a_l = G_0(l/L) - G_0((l-1)/L)$, for $l = 1, \dots, L$. Together, these parameters determine how the data is allocated across the l intervals on the support of the weight distribution and the initial shape of the distribution. Using the Dirichlet process as a nonparametric prior for G allows for general distributional shapes and thus provides flexibility in estimating the mixture weights.

3.2.2 Transition Kernels

Each transition kernel in (3.2) corresponds to the distribution for a random pair (U_l, V_l) , for $l = 1, \dots, L$. That is, $f_l \equiv f_{U_l|V_l}$, where f_l denotes the transition kernel and $f_{U_l|V_l}$ is the associated conditional density. Necessary and sufficient conditions for constant first and second moments are difficult to establish. Zheng et al. (2022) offer an alternative condition on

the marginal densities of bivariate distributions that define the transition kernels, simplifying implementation while avoiding restrictive constraints on the parameter space. Proposition 1 states that if a stationary marginal density f_X that corresponds to the marginal densities of a bivariate random vector (U_l, V_l) , for all l , can be identified, then the resulting time series is first-order strictly stationary ([Zheng et al. 2022](#)).

Proposition 1 *Consider a set of bivariate random vectors (U_l, V_l) that takes values in $S \times S \subset \mathbb{R}$, with conditional densities $f_{U_l|V_l}, f_{V_l|U_l}$ and marginal densities f_U, f_V , for $l = 1, \dots, L$. Let $w_l \geq 0$, for $l = 1, \dots, L$, such that $\sum_{l=1}^L w_l = 1$. Consider a time series $\{X_t : t \in \mathbb{N}\}$, where $X_t \in S$, generated from*

$$f(x_t | \mathbf{x}^{t-1}) = \sum_{l=1}^L w_l f_{U_l|V_l}(x_t | x_{t-l}), \quad t > L, \quad (3.4)$$

and from

$$f(x_t | \mathbf{x}^{t-1}) = \sum_{l=1}^{t-2} w_l f_{U_l|V_l}(x_t | x_{t-l}) + \left(1 - \sum_{k=1}^{t-2} w_k\right) f_{U_{t-1}|V_{t-1}}(x_t | x_1), \quad 2 \leq t \leq L. \quad (3.5)$$

If a time series satisfies the invariant condition: $X_1 \sim f_X$, and $f_{U_l}(x) = f_{V_l}(x) = f_X(x)$, for all $x \in S$, and for all l , then this time series is first-order strictly stationary with invariant marginal density f_X .

In addition, Proposition 1 applies to continuous, discrete, or mixed distributions.

Building on Proposition 1, [Zheng et al. \(2022\)](#) outline two general methods for constructing transition kernels: the bivariate distribution method and the conditional distribution method.

The bivariate distribution method identifies a bivariate distribution of (U_l, V_l) such that the marginal densities f_{U_l} and f_{V_l} are equal to a pre-specified stationary marginal density f_X for l th transition kernel. The conditional distribution method finds compatible conditional densities, $f_{U_l|V_l}$ and $f_{V_l|U_l}$, to specify the bivariate density of (U_l, V_l) for the l th transition kernel.

The Gaussian MTD model, for example, is constructed via the bivariate distribution method. Under marginal $f_x(x) = N(x|\mu, \sigma^2)$, the Gaussian MTD model can be constructed as

$$f(x_t | \mathbf{x}^{t-1}) = \sum_{l=1}^L w_l N(x_t | (1 - \rho_l)\mu + \rho_l x_{t-l}, \sigma^2(1 - \rho_l^2)). \quad (3.6)$$

3.3 Bayesian Implementation

3.3.1 Hierarchical Model Formulation

Inference is facilitated through a set of latent variables, which identify kernels within the structured mixture model. Let $\{Z_t\}_{t=L+1}^n$ be the set of latent variables, where each Z_t has a discrete distribution with support $\{1, \dots, L\}$. $Z_t = l$ selects the l th kernel through a random mechanism that is not directly observable. In addition, $p(z_t|w) = \sum_{l=1}^L w_l \delta_l(z_t)$, where $w = (w_1, \dots, w_L)^T$, and $\delta_l(z_t) = 1$ if $z_t = l$ and 0 otherwise. Based on the specific value of z_t , $\delta_l(z_t)$ selects the corresponding w_l .

The full Bayesian model is completed by the specification of prior distributions for the parameters θ . The priors for θ depend on the form of the kernels f_l . For the cdf-based

weights, the priors for w is $CDP(w|\alpha_0, a_0, b_0)$.

3.3.2 Model Estimation and Prediction

The posterior distribution of the parameters, based on the conditional likelihood, is

$$p(w, \theta, \{z_t\}_{t=L+1}^n | D_n) \propto \pi_w(w) \prod_{l=1}^L \pi_l(\theta_l) \prod_{t=L+1}^n \left\{ f_{z_t}(x_t | x_{t-z_t}, \theta_{z_t}) \sum_{l=1}^L w_l \delta_l(z_t) \right\}. \quad (3.7)$$

$D_n = \{x_t\}_{t=L+1}^n$ is the data. In this general framework, full simulation-based Bayesian estimation and prediction can be achieved using Markov chain Monte Carlo (MCMC) algorithms.

Conditioning on $\{z_t\}_{t=L+1}^n$ and w , the posterior full condition for each θ_l depends on the specific form of the kernel f_l , which will be presented in Chapter 5. Conditioning on θ and w , the posterior full condition of each latent variable Z_t is a discrete distribution on $\{1, \dots, L\}$ with probabilities proportional to $w_l f_l(x_t | x_{t-l}, \theta)$. Conditioning on $\{z_t\}_{t=L+1}^n$ and θ , the posterior full condition for w depends only on $M_l = |\{t : z_t = l\}|$, for $l = 1, \dots, L$, where $|\{\cdot\}|$ is the carnality or the size of the set $\{\cdot\}$.

Turning to predictions for future values, the one-step-ahead posterior predictive density is

$$p(x_{n+1} | D_n) = \int \int \left\{ \sum_{l=1}^L w_l f_l(x_{n+1} | x_{n+1-l}, \theta_l) \right\} p(\theta, w | D_n) d\theta dw. \quad (3.8)$$

The k -step-ahead posterior predictive density, which incorporates the uncertainty from the parameter estimation and the predictions of the previous $(k - 1)$ out-of-sample values, can be obtained by extending the posterior predictive density in (3.8).

Our work builds upon the MTD time series model by Zheng et al. (2022) and draws inspiration from the nearest-neighbor mixture processes (NNMP) and the discrete nearest-neighbor mixture processes (DNNMP) spatial models developed by the same authors (Zheng et al. 2023b, 2023a). The MTD model by Zheng et al. (2022) includes Gaussian, Poisson, negative binomial MTD, and Lomax MTD regression models, with applications to simulated data, crime incidents and precipitation prediction. Their flexibility offers potential for broader applications. However, to satisfy Proposition 1, for certain invariant marginal distributions, the transition kernel may either require careful construction or can result in a form that is not explicitly defined or too complex. The NNMP and DNNMP models effectively use copula to model dependence and marginals separately. Building onto the class of MTD models and motivated by the class of NNMP and DNNMP models, we propose to incorporate copula-based transition kernels. The proposed model is presented in the next chapter.

Chapter 4: Proposed Method: Copula-Based Gamma MTD Models

The proposed MTD model extends the original MTD model by incorporating copulas into the transition kernels. By allowing dependence structures to be modeled separately from the marginal distribution, the proposed approach enables a choice of copula families that effectively capture the data's dependence structures while allowing flexibility in marginal selection, thereby enhancing modeling capabilities and flexibility.

The invariant condition in Proposition 1 is achieved using the bivariate distribution approach, which specifies the stationary density f_X as the marginal densities of (U_l, V_l) , f_{U_l} and f_{V_l} , for all l . This is facilitated by the use of a copula, which separates the marginal behavior of the random variables from their dependence structure.

Copula is a multivariate cumulative distribution function where its marginal distribution of each random variable follows a uniform distribution on the interval $[0, 1]$. Copulas are useful for modeling dependence between random variables. Copulas decompose any joint distribution F into two parts: the copula C and the marginal distributions F_j . The theoretical groundwork for copulas is rooted in Sklar's theorem Sklar (1959).

Definition 1 *For any p -dimensional multivariate cumulative distribution function of a random vector (X_1, \dots, X_p) , denoted as $F(x_1, \dots, x_p)$, there exists a copula function $C : [0, 1]^p \rightarrow [0, 1]$ for which $F(x_1, \dots, x_p) = C(F_1(x_1), \dots, F_p(x_p))$, where F_j is the marginal*

cumulative distribution function of $X_j, j = 1, \dots, p$.

If X_j is continuous for all j , then C is unique and differentiable. The joint probability density function of $X_j, j = 1, \dots, p$ is given by $f(x_j) = c(x_j) \prod_{j=1}^p f_j(x_j)$, where $c = \partial^p C / \partial F_j$ is the copula density and f_j is the density of X_j .

In the bivariate setting, as outlined in the bivariate distribution approach, the joint density of (U_l, V_l) is $f_{U_l, V_l}(x_t, x_{t-l}) = c(x_t, x_{t-l}) f_{U_l}(x_t) f_{V_l}(x_{t-l})$. By applying the law of conditional probability, the conditional density of U_l given V_l is then $f_{U_l|V_l}(x_t|x_{t-l}) = c(x_t, x_{t-l}) f_{U_l}(x_t) f_{V_l}(x_{t-l}) / f_{V_l}(x_{t-l}) = c(x_t, x_{t-l}) f_{U_l}(x_t)$. Given a pre-specified stationary marginal density f_X , and replace f_{U_l} and f_{V_l} with f_X , for every x_t and for all l . For $t > L$, the proposed copula-based MTD model specifies the conditional distribution as

$$f(x_t | \mathbf{x}^{t-1}) = \sum_{l=1}^L w_l c_l(x_t, x_{t-l}) f_X(x_t) \quad (4.1)$$

$c_l(x_t, x_{t-l})$ is the copula density evaluated at x_t and x_{t-l} , and $f_X(x_t)$ is the stationary marginal density evaluated at x_t . Compared to 3.2, the transition kernel, f_l , is now replaced by two components: the copula density c_l , and the stationary marginal density f_X . The copula captures the dependence between current and lagged value and controls the strength of the dependence through a dependence parameter. Stationary marginal density describes the marginal behavior of the current value. A variety of copula families and marginal distributions are available for choice. Without much modifications to our proposed model, the marginal distribution can take any form, but is limited to continuous distributions.

4.1 Copula

We consider the Gaussian copula with the dependence parameter ρ . A Gaussian copula for (X_1, X_2) is

$$C(u_1, u_2 | \rho) = \Phi_2(\Phi^{-1}(u_1), \Phi^{-1}(u_2) | \rho) \quad (4.2)$$

$u_j = F_j(x_j)$ are standard uniform distribution, where F_j is the marginal cdf of X_j , for $j = 1, 2$. Φ_2 is the cdf of a bivariate standard Gaussian distribution with the dependence parameter $\rho \in (-1, 1)$, and Φ is the cdf of a univariate standard Gaussian distribution. If both X_1 and X_2 are continuous variables, the copula has the density

$$c(\Phi^{-1}(u_1), \Phi^{-1}(u_2) | \rho) = \frac{1}{\sqrt{1 - \rho^2}} \exp \left(\frac{2\rho\Phi^{-1}(u_1)\Phi^{-1}(u_2) - \rho^2\{\Phi^{-1}(u_1)^2 + \Phi^{-1}(u_2)^2\}}{2(1 - \rho^2)} \right). \quad (4.3)$$

4.2 Marginal Distribution

We choose Gamma with the shape, α , and the rate parameter, β , as the marginal distribution, i.e., $\text{Gamma}(\alpha, \beta)$ with mean α/β and variance α/β^2 . Figure 4.1 illustrates gamma distributions with varying shape and rate parameters, which are subsequently used in the simulation studies. The Gamma distribution is useful for modeling positively-skewed, non-negative data, such as failure times, runoff amounts, and insurance claims. Figure 1.1 illustrates a positively-skewed time series dataset of wind speeds, motivating the model design.

While we use a Gaussian copula with a Gamma marginal distribution to illustrate the

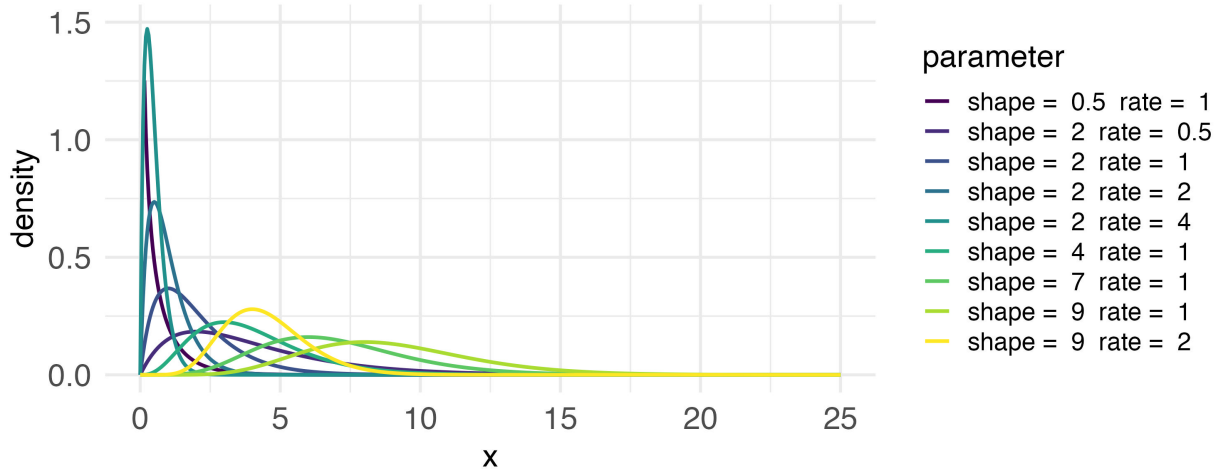


Figure 4.1: Probability density function (PDF) of the gamma distribution with varying shape and rate parameters

structure of the proposed model, other choices of copulas and marginal distributions can also be employed without requiring significant modifications to the proposed model. For example, one could develop a Gumble copula with a Gamma MTD model or a Gaussian copula with a Beta MTD model, among others. As copula modeling constitutes a substantial research area beyond the scope of this work, we refer the reader to Joe (2014) for more details.

Chapter 5: Overview of MCMC Algorithms

The full Bayesian model is completed by the specification of prior distributions for the parameters α , β , ρ , and w , where α and β are parameters of the gamma marginals, and ρ and w are the dependence and weight parameters, respectively. For the copula-based Gamma MTD model, the priors are specified as $Gamma(\alpha|u_\alpha, v_\alpha)$, $Gamma(\beta|u_\beta, v_\beta)$, and $Unif(\rho_l|-1, 1)$. For the cdf-based weights, the prior is $CDP(w|\alpha_0, a_0, b_0)$.

The parameters α , β , and ρ are updated using a slice sampler (Neal 2003). Following the definition in Equation 4.1, denote $f_l(x_t|x_{t-l})$ as $f_l(x_t|x_{t-l}) = c_l(x_t, x_{t-l})f_X(x_t)$, where f_l is the transition kernel, c_l is the copula density, and f_X is the stationary marginal density. The posterior full conditional distributions for the marginal parameters α and β are proportional to $Gamma(\alpha|u_\alpha, v_\alpha) \prod_{t=L+1}^n f_l(x_t|x_{t-l})$ and $Gamma(\beta|u_\beta, v_\beta) \prod_{t=L+1}^n f_l(x_t|x_{t-l})$, respectively. The posterior full conditional distribution for each of the dependence parameters ρ is proportional to $Unif(\rho_l|-1, 1) \prod_{t:z_t=l} c_l(x_t, x_{t-l})$.

For the latent variables $\{z_t\}_{t=L+1}^n$, the posterior full conditional for each z_t is a discrete distribution on $\{1, \dots, L\}$, where the probability of $z_t = l$, denoted by q_l , is proportional to $w_l c_l(x_t, x_{t-l})$, for $l = 1, \dots, L$. The posterior full conditional distribution for weight parameters w , under the cdf-based prior, is $Dirichlet(\alpha)$, where $\alpha = (\alpha_0 a_1 + M_1, \dots, \alpha_0 a_L + M_L)$.

The MCMC algorithm, adapted from Zheng's source code for the MTD model (Zheng et

al. 2022), is written in R, with certain functions written in C++. Algorithm 1 (Figure 5.1) requires data, mtd order, hyperparameters of the priors for α , β , w , and starting values for α , β , ρ . It also requires tuning parameters for the slice sampler, including step size and upper bounds for α and β , along with the general MCMC settings such as number of iterations, burn-in period, and thinning interval. The algorithm outputs posterior samples of α , β , ρ and w . Asterisk (*) denotes steps that differ from of the algorithm by Zheng et al. (2022).

Algorithm 1 MCMC Algorithm for Parameter Estimation for Gamma MTD Models

Require: data y , mtd order L , priors for α , β , w , starting for α , β , ρ , tuning for slice sampler, mcmc settings

Ensure:

```

 $\alpha$ : a vector of marginal parameters with dimension nsample = (niter - nburn)/nthin
 $\beta$ : a vector of marginal parameters with dimension nsample
 $\rho$ : a matrix of dependence parameters with dimension  $L \times \text{nsample}$ 
 $w$ : a matrix weight parameters with dimension  $L \times \text{nsample}$ 
Initialize  $\alpha$ ,  $\beta$ ,  $\rho$ ,  $\{z_t\}_{t=L+1}^n$ ,  $w$ 
for each MCMC iteration iter = 1, ..., niter do
    update  $\alpha$                                  $\triangleright$  Sample  $\alpha$  using a slice sampler *
    update  $\beta$                                  $\triangleright$  Sample  $\beta$  using a slice sampler *
    update  $\rho$                                  $\triangleright$  Sample  $\rho_l, l = 1, \dots, L$  using a slice sampler *
    update  $\{z_t\}_{t=L+1}^n$                      $\triangleright$  Sample  $z_t, t = L + 1, \dots, n$  with probability  $q_l$  *
    update  $w$                                   $\triangleright$  Sample  $w_l, l = 1, \dots, L$  from Dirichlet( $\cdot$ )
end for
Discard the first nburn iterations and retain every nthin iteration

```

Figure 5.1: MCMC Algorithm for Parameter Estimation for Gamma MTD Models

Chapter 6: Simulation Studies

6.1 Simulation Settings

The goal of simulation studies is to assess accuracy and performance of the proposed model in Chapter 4. We examine a range of settings by varying the parameters for weight, dependence, and marginal distribution.

With weight parameters w , dependence parameters for Gaussian copula ρ , shape α and rate parameter β , we generate $n = 2000$ observations from the copula-based Gamma MTD model. For model fitting, we set the order $L = 5$ and consider the Gaussian copula with gamma marginals.

To be consistent with the original MTD studies, we run the Gibbs sampler for 165,000 iterations, discard the first 5000 iterations as burn-in, and collect samples every 20 iterations, resulting in 8000 iterations per MCMC chain. To ensure that we can assess MCMC convergence and obtain more precise estimates of parameters, we also run four MCMC chains with 8000 iterations each for all of the following scenarios in Tables (Table 6.1, Table 6.2), which contain the description and the summary of scenarios, respectively.

In all scenarios, we use the cdf-based Dirichlet process (CDP) prior on the weights. Other prior choices, such as the Dirichlet prior and the truncated stick-breaking (SB) prior are

Table 6.1: Description of Scenarios for Gamma Model

Section 6.2.1: Convergence Diagnostics
- Focuses on convergence diagnostics using the Gelman-Rubin statistic and additional diagnostic tools.
- Scenario 1: Follows the same setup as the original studies.
Section 6.2.2: Weight, Dependence Parameters, w, ρ
- Focuses on weight and dependence parameters for the copula.
- Scenarios 1, 2: Follow the same setup as the original studies.
- Scenarios 1.3, 1.4: Involve incompatible weight and dependence.
- Scenarios 1.5, 1.6: Involve compatible weight and dependence, but rarely observed patterns.
Section 6.2.3: Shape, Rate Parameters, α, β
- Examines varying parameters for the marginal distribution.
- Scenarios 3-6: Present the usual cases.
- Scenarios 7-9: Focus on unusual cases with highly skewed distributions.

Table 6.2: Summary of Scenarios for Gamma Model

Scenario	w	ρ	α	β
1	$w_i \propto \exp(-i), i = 1, \dots, 5$	(0.7, 0.5, 0.3, 0.1, 0.1)	7	1
2	(0.2, 0.05, 0.45, 0.05, 0.25)	(0.4, 0.1, 0.7, 0.1, 0.5)		
1.3	$w_i = (0.2, 0.2, 0.2, 0.2, 0.2)$	(0.7, 0.5, 0.3, 0.1, 0.1)	7	1
1.4	$w_i \propto \exp(-i), i = 1, \dots, 5$	(0.1, 0.1, 0.3, 0.5, 0.7)		
1.5	$w_i \propto \exp(-i), i = 5, \dots, 1$	(0.1, 0.1, 0.3, 0.5, 0.7)	7	1
1.6	$w_i = (0.2, 0.2, 0.2, 0.2, 0.2)$	(0.5, 0.5, 0.5, 0.5, 0.5)		
3	$w_i \propto \exp(-i), i = 1, \dots, 5$	(0.7, 0.5, 0.3, 0.1, 0.1)	4	1
4			9	1
5			2	1/2
6			9	2
7	$w_i \propto \exp(-i), i = 1, \dots, 5$	(0.7, 0.5, 0.3, 0.1, 0.1)	2	1
8			2	2
9			2	4

readily available, but the original MTD studies has shown that SB and CDP priors give more precise estimates.

All scenarios were initially analyzed using a single replicate. Scenarios 1 and 2 were further evaluated with multiple replicates to assess coverage and robustness. Each replicate consisted of a new synthetic dataset generated with the same underlying parameters but different random seeds. Specifically, we ran the models on 40 independently generated replicates for Scenarios 1 and 2 to evaluate the consistency and robustness of the results, ensuring comparability across scenarios.

6.2 Simulation Results

6.2.1 Convergence Diagnostics

Scenario 1 in Table 6.2 serves as an example to show and track convergence and has the same setup as Scenario 1 in the original MTD studies.

Tables (Table 6.3, Table 6.4, Table 6.5) present the posterior estimates and convergence diagnostics for the parameters related to weight, dependence, and marginal distribution, respectively. We defer the discussion of the estimates of the posterior mean and standard deviation (mean and SD) until a later section. There is no evidence of lack of convergence for all parameters (Gelman-Rubin statistic R and its upper CI ≤ 1.1). The simulation error of the estimates is also negligible for all parameters (Naive SE and Time-series SE are close to zero).

Table 6.3: Estimates and Gelman-Rubin Diagnostics for Scenario 1's w at Each Lag

.	Mean (SD)	R (Upper CI)	Naive SE	Time-series SE
$w_1 = 0.636$	0.6411 (0.0425)	1 (1)	0.0002	0.0003
$w_2 = 0.234$	0.1908 (0.0642)	1 (1)	0.0004	0.0013
$w_3 = 0.086$	0.1283 (0.0742)	1 (1)	0.0004	0.0022
$w_4 = 0.032$	0.0341 (0.0532)	1.01 (1.02)	0.0003	0.0017
$w_5 = 0.012$	0.0057 (0.0224)	1.02 (1.02)	0.0001	0.0008

Table 6.4: Estimates and Gelman-Rubin Diagnostics for Scenario 1's ρ at Each Lag

.	Mean (SD)	R (Upper CI)	Naive SE	Time-series SE
$\rho_1 = 0.700$	0.6789 (0.0281)	1 (1)	0.0002	0.0002
$\rho_2 = 0.500$	0.5991 (0.1442)	1 (1)	0.0008	0.0027
$\rho_3 = 0.300$	0.1258 (0.2468)	1 (1)	0.0014	0.0020
$\rho_4 = 0.100$	0.0103 (0.4721)	1 (1)	0.0026	0.0027
$\rho_5 = 0.100$	-0.0063 (0.5591)	1 (1)	0.0031	0.0032

Gelman–Rubin convergence diagnostic and ACF plots (Figure B.1, Figure B.2, Figure B.3) can be found in the Appendix B Section B.1.1. In Scenario 1, the chains converge more rapidly for the parameters related to the marginal distribution, achieving convergence at around 2000 iterations. The chains converge more slowly for the parameters related to weight and dependence, especially at later lags. Nevertheless, all weight and dependence parameters reach convergence by 8000 iterations. Similar patterns emerge across all other scenarios. Trace and density plots (Figure B.4, Figure B.5, Figure B.6) are also included in Appendix B Section B.1.1.

Table 6.5: Estimates and Gelman-Rubin Diagnostics for Scenario 1's α, β

.	Mean (SD)	R (Upper CI)	Naive SE	Time-series SE
$\alpha = 7$	7.4402 (0.3447)	1 (1)	0.0019	0.0023
$\beta = 1$	1.0058 (0.0477)	1 (1)	0.0003	0.0003

6.2.2 Weight and Dependence Parameters for Copula

Scenarios 1, 2, 1.3, 1.4, 1.5, 1.6 in Table 6.2 are employed to demonstrate the effectiveness of weight and dependence construction, as well as their interplay.

Scenario 1 and 2 share the same setup as the original MTD studies, where weight and dependence are compatible. In Scenario 1, we consider exponentially decreasing weights. In Scenario 2, we consider an uneven arrangement of the relevant lags.

We explore additional scenarios to investigate outcomes when weight and dependence are incompatible, as well as cases where they are compatible but follow rarely observed patterns. In Scenario 1.3, we assign equal weights while preserving a decreasing dependence structure. In Scenario 1.4, we retain exponentially decreasing weights but reverse the direction of dependence. In Scenario 1.5, both weights and dependence are set to increase. In Scenario 1.6, we set both weights and dependence to be equal.

We first examine two cases where the weight parameters and the dependence parameters are compatible. As shown in (a), (b) of Figure 6.1, the results appear reasonable; that is, the estimates are consistent with the true values, with minor discrepancies. Nevertheless, the differences are minimal, and the 95% posterior credible intervals cover the true value for both weight and dependence across all lags.

We then explore additional scenarios to investigate the outcomes when they are not compatible. As shown in (c) and (d) of Figure 6.1, the results appear unusual, with some noticeable discrepancies at later lags. The 95% posterior credible intervals cover the true value for both

weight and dependence for most lags.

Moving on to the remaining cases where weights and dependence are compatible, though they follow patterns that are rarely observed in real-world settings. As shown in (e) and (f) of Figure 6.1, the results appear reasonable, with minimal discrepancies. The 95% posterior credible intervals cover the true value for both weight and dependence for most lags.

In these scenarios, greater weight on a lag yields narrower 95% posterior credible interval (CI) for that lag, while lesser weight results in wider CI. If more weight is placed on a lag, it contributes more to the current value. This increased contribution provides the model with more information to estimate its influence, resulting in narrower CI. Conversely, with less information available to estimate its influence, the CI widens and approaches the prior distribution.

6.2.3 Parameters for Marginal Distributions

Scenario 3 to 6 in Table 6.2 are used to evaluate the shape and the rate parameter for the gamma marginal distribution. Scenario 7 through 9 are used to evaluate these parameters in cases with high skewness.

In Scenario 3 to 9, we revert to the same settings for weight and dependence as used in Scenario 1. That is, we fix $w_i \propto \exp(-i)$, $i = 1, \dots, 5$ and $\rho_l = (0.7, 0.5, 0.3, 0.1, 0.1)$.

The slice sampler may encounter difficulties when the target distribution is not evaluable. In particular, skewness of the target distribution may reduce the efficiency of the slice sampler

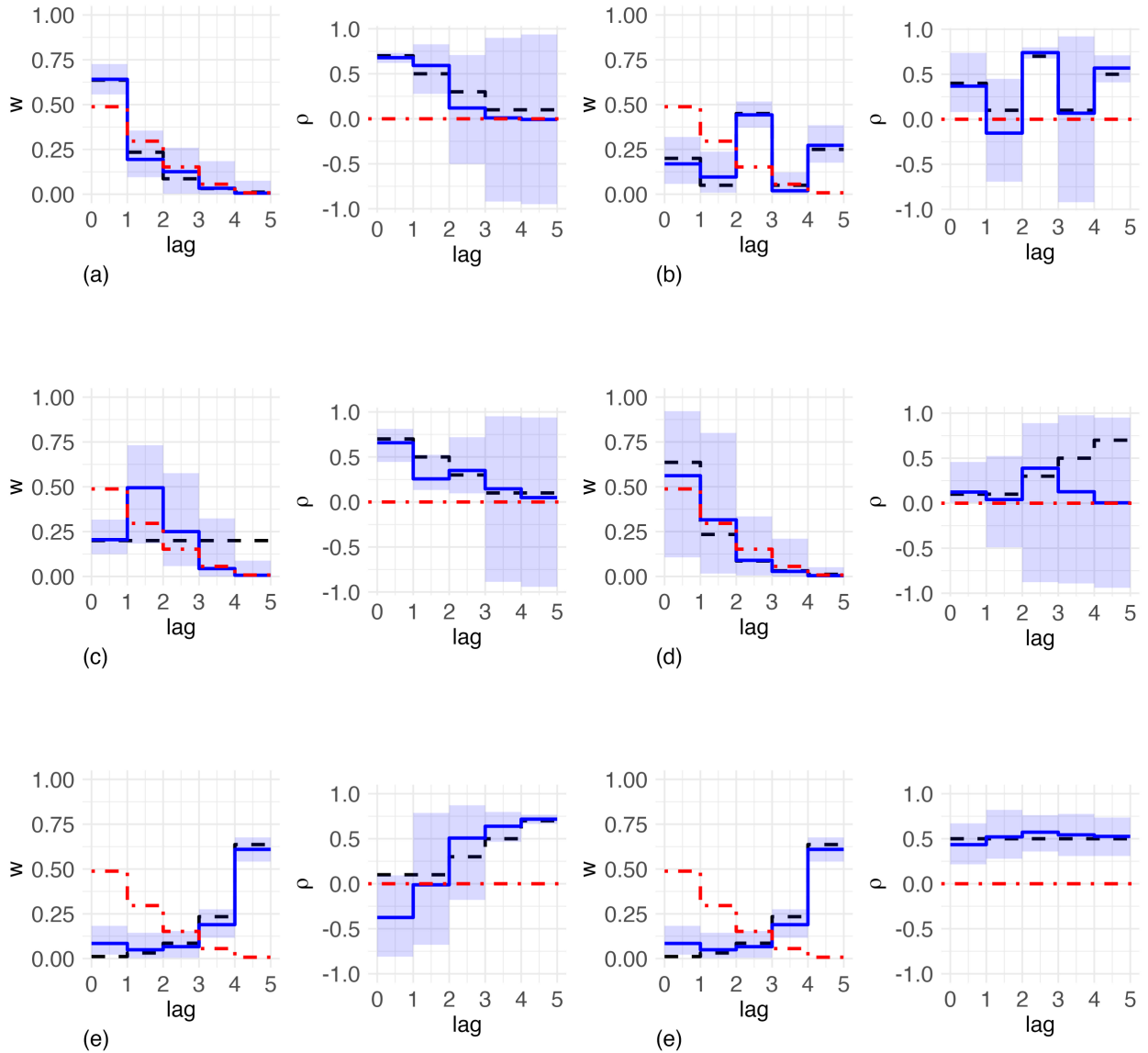


Figure 6.1: (a), (b) Results for Scenarios 1 and 1.2: default setup; (c), (d) Scenarios 1.3 and 1.4: incompatible weight and dependence; (e), (f) Scenarios 1.5 and 1.6: compatible, but rarely observed patterns. (Left) Dashed lines are true weights, dot-dashed lines are prior means, solid lines are posterior means, and polygons are 95% posterior credible intervals. (Right) Dashed (black) lines are true dependence, dot-dashed (red) lines are prior means, solid (blue) lines are posterior means, and (purple) polygons are 95% posterior credible intervals.

Table 6.6: Results for Scenario 3-6

.	Mean (SD)	R (Upper CI)	Naive SE	Time-series SE
$\alpha = 4$	4.2837 (0.1972)	1 (1)	0.0011	0.0012
$\beta = 1$	0.9969 (0.0479)	1 (1)	0.0003	0.0003
$\alpha = 9$	8.2139 (0.3833)	1 (1)	0.0021	0.0025
$\beta = 1$	0.9033 (0.0433)	1 (1)	0.0002	0.0003
$\alpha = 2$	1.8826 (0.0863)	1 (1)	0.0005	0.0005
$\beta = 1/2$	0.491 (0.0249)	1 (1)	0.0001	0.0001
$\alpha = 9$	9.1979 (0.4195)	1 (1)	0.0023	0.0029
$\beta = 2$	2.06 (0.0961)	1 (1)	0.0005	0.0007

Table 6.7: Results for Scenario 7-9

.	Mean (SD)	R (Upper CI)	Naive SE	Time-series SE
$\alpha = 2$	2.1738 (0.0977)	1 (1)	0.0005	0.0006
$\beta = 1$	0.9868 (0.0487)	1 (1)	0.0003	0.0003
$\alpha = 2$	1.8476 (0.0841)	1 (1)	0.0005	0.0005
$\beta = 2$	1.7937 (0.091)	1 (1)	0.0005	0.0005
$\alpha = 2$	1.8825 (0.0859)	1 (1)	0.0005	0.0005
$\beta = 4$	3.9277 (0.1976)	1 (1)	0.0011	0.0011

by inducing correlations between successive samples ([Planas and Rossi 2024](#)). To investigate this effect, we explore additional scenarios to identify where the algorithm may fail, focusing on Scenarios 7 through 9, which exhibit increasing skewness and are highlighted in Figure 4.1.

As shown in Table 6.6, the results appear reasonable; that is, convergence has been achieved and the estimates are consistent with the true values. As shown in Table 6.7, the results also appear reasonable. Additional plots (Figure B.7, Figure B.8) can be found in the Appendix B Section B.1.3.

Table 6.8: Setups and Prior Specifications for Scenario 1: α and β .

.	Prior for α	Prior for β	Description
1	$Gamma(49, 7)$	$Gamma(1, 1)$	Informative prior for both α and β .
2	$Gamma(4.9, 0.7)$	$Gamma(1, 1)$	Diffuse prior for α . Informative prior for β .
3	$Gamma(49, 7)$	$Gamma(0.1, 0.1)$	Informative prior for α . Diffuse prior for β .
4	$Gamma(10, 1)$	$Gamma(1, 1)$	Shifted prior for α . Informative prior for β .
5	$Gamma(49, 7)$	$Gamma(4, 1)$	Informative prior for α . Shifted prior for β .

6.2.4 Sensitivity Analysis

For the prior sensitivity analysis, we re-run Scenario 1 using five different sets of priors. Table 6.8 presents the setups and descriptions of these prior specifications. Figure 6.2 illustrates some examples.

Results appear reasonable, and the estimates are consistent with the true values, indicating that the model is robust to the choice of prior.

6.2.5 Coverage Assessment

To compute coverage rates, for each of the 40 replicates, we first combine the four chains of 8000 posterior samples per parameter, then calculate the 95% credible interval from the combined samples, and record whether the true parameter value falls within this interval. The overall coverage is the proportion of replicates in which the true value is contained within the interval.

As shown in Tables (Table 6.9 and Table 6.10), the 95% credible intervals for all parameters successfully contain the true values in most replicates across both scenarios. Most parameters

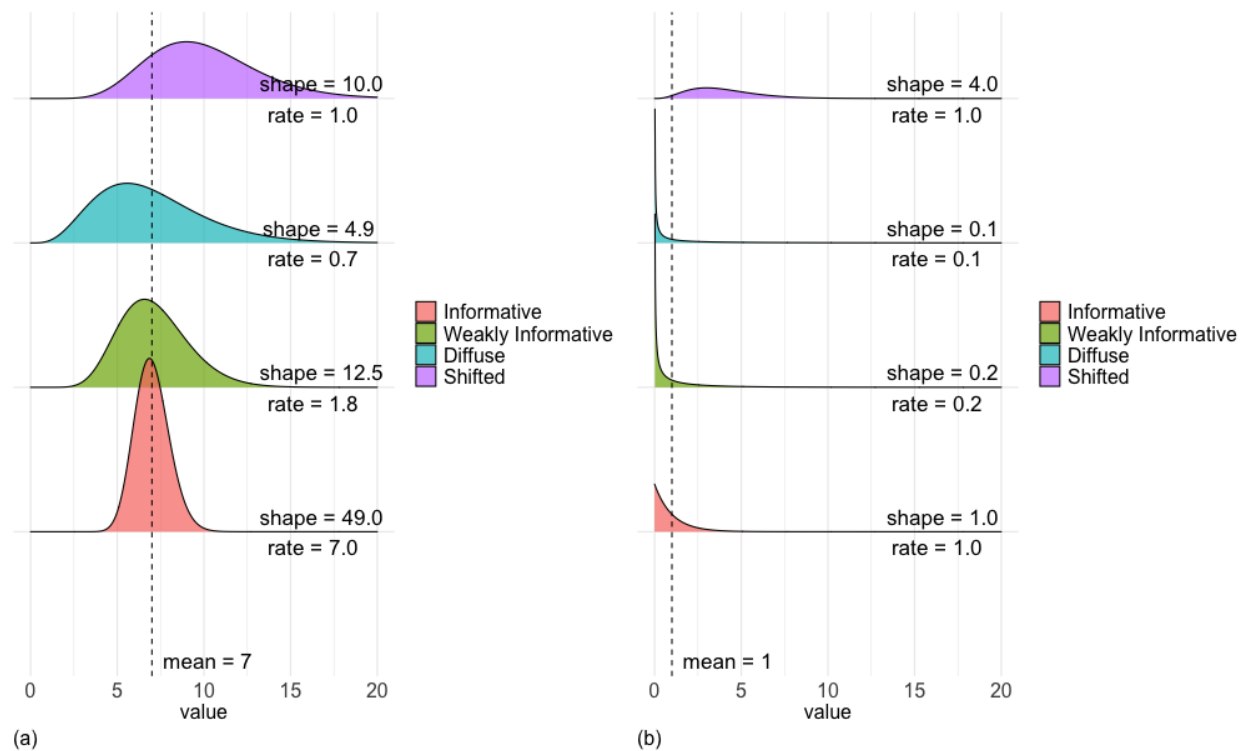


Figure 6.2: Examples of Prior Distributions for Scenario 1: (a) Priors for α , with the true value equal to 7, and (b) priors for β , with the true value equal to 1.

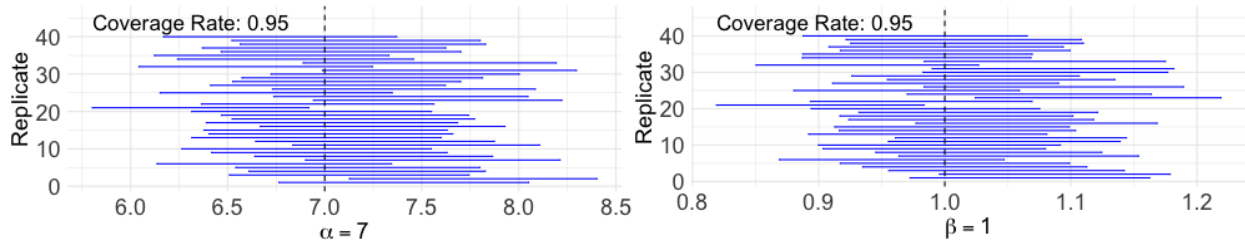
Table 6.9: Coverage Rates for All Parameters Across 40 Replicates for Scenario 1.

α	β	w_1	w_2	w_3	w_4	w_5	ρ_1	ρ_2	ρ_3	ρ_4	ρ_5
0.95	0.95	0.97	0.97	1.00	1.00	1.00	0.90	0.97	1.00	0.97	1.00

Table 6.10: Coverage Rates for All Parameters Across 40 Replicates for Scenario 2.

α	β	w_1	w_2	w_3	w_4	w_5	ρ_1	ρ_2	ρ_3	ρ_4	ρ_5
0.95	0.95	1.00	1.00	0.97	0.97	0.95	1.00	0.97	0.95	1.00	0.95

achieve full coverage, with a few slightly below 1, indicating that the credible intervals reliably capture the true parameter values. Importantly, the lengths of the credible intervals vary across parameters, reflecting differences in estimation uncertainty. Figure 6.3 and Figure 6.4 show these intervals.

Figure 6.3: Coverage Rates for α and β Across 40 Replicates for Scenario 1.

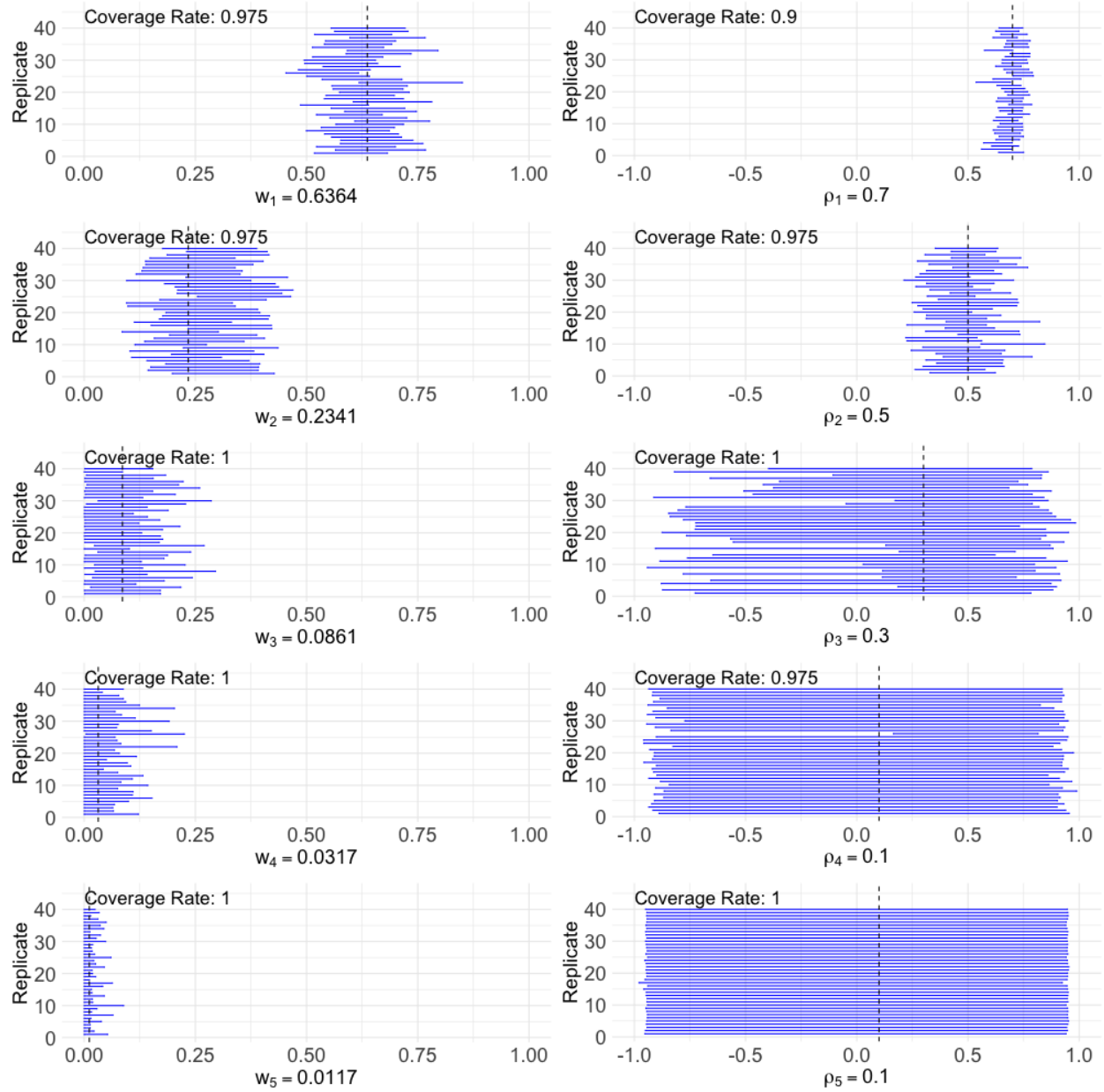


Figure 6.4: Coverage Rates for w and ρ Across 40 Replicates for Scenario 1.

Chapter 7: Prediction

Table 7.1 summaries the 95% one-step ahead posterior predictive intervals for Scenario 1 through 9. As presented in this table, the model appropriately captures the predictive uncertainty across all scenarios. Figure 7.1 illustrate these intervals for Scenario 1 and 2. The differences in the observed patterns arise from the specific configurations of the weight and dependence parameters in each scenario; Scenario 1 employs exponentially decreasing weight and dependence, while Scenario 2 adopts an uneven arrangement of weight and dependence across lags. Additional plots illustrating the intervals for Scenarios 3 through 9 (Figure D.1, Figure D.2) are provided in the Appendix D.

Table 7.1: Empirical coverage of the 95% predictive intervals for Gamma Scenario 1-9 (s1–s9).

	s1	s2	s3	s4	s5	s6	s7	s8	s9
Coverage	0.9539	0.9524	0.9514	0.9474	0.9539	0.9479	0.9534	0.9459	0.9549

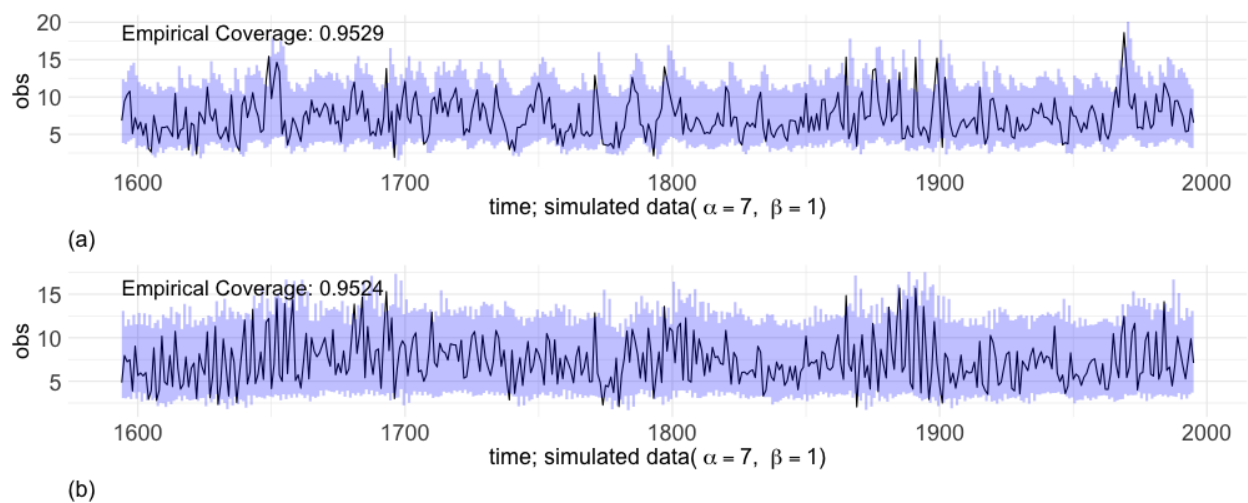


Figure 7.1: 95% one-step ahead posterior predictive intervals for (a) Gamma Scenario 1 and (b) Scenario 2.

Chapter 8: Discussion

In this part of the dissertation, we review a broad class of stationary MTD models and propose a novel copula-based MTD model that builds upon the existing framework. We also present the algorithms and simulation studies, which demonstrate promising results across various scenarios. The advantage of our proposed approach is that, by incorporating copulas into the existing MTD models, the dependence structure and the marginal distribution can be modeled separately, allowing the marginal distribution to be any continuous form.

In real-world settings, some data exhibit zero-inflation and requires modeling with a mixture model with a point mass at zero. For example, medical costs, insurance claims, precipitation amounts, as well as transportation safety measures such as lane departure severity scores ([Mills 2013](#)) and vehicle deceleration during braking ([Feng 2020](#)). Failure to address these issues undermines model robustness and results. Furthermore, the copula approach may encounter issues when handling a large number of zeros. In such case, the marginal distribution needs to be re-constructed. This motivates the methodological developments introduced in Part II, where we develope a model that addresses the issues of zero-inflation.

Moreover, a previous study ([Hassan 2021](#)) found comparable predictive performance for disease spread between the probabilistic MTD model and the deep learning long short-term memory (LSTM) network. We aim to compare our approach to this alternative method.

This comparative analysis is presented in Part III, where we compare the performance of our proposed MTD models against the LSTMs through simulation studies and real-world data applications.

Part II

Models for Forecasting Zero-Inflated Skewed Time Series

Chapter 9: Introduction

Zero-inflated data are characterized by an excess of zero values. In these data types, observations often feature a point mass at zero, followed by values from a separate distribution that can be discrete, continuous, or otherwise non-zero. Zero-inflated count data frequently occur in a wide range of domains, including finance, economics, healthcare, transportation, and ecology. While zero-inflated count data have been studied extensively, zero-inflated continuous, or semicontinuous, data also arise frequently in practice. Examples of semicontinuous data are medical expenditures (Duan et al. 1983; Neelon et al. 2015, 2016a, 2016b; Liu et al. 2019), insurance claims (Shi and Yang 2018; Yang 2022), precipitation amounts (Hyndman and Grunwald 2000; Abraham and Tan 2009; Dzupire et al. 2018; Kaewprasert et al. 2024), lane departure severity scores (Mills 2013), and vehicle deceleration during braking (Feng 2020).

There are two classes of models designed to handle data with excessive zeros: two-component, zero-inflated (ZI) models (Lambert 1992) and two-part, hurdle models (Mullahy 1986). Both models employ a mixture of a binary component modeling zeros and a separate component modeling non-zero values, which can be either count or continuous. The key distinction lies in the source of zeros. In ZI models, zeros may arise from both the binary and non-zero components, whereas in hurdle models, zeros occur exclusively in the binary component, with the non-zero component restricted to non-zero values.

Building upon the architecture of the MTD model introduced in 2022 by Zheng et al. (2022), in Part I we proposed the copula-based Gamma MTD model, which enables flexible dependence modeling and accommodates arbitrary continuous marginals, thereby enhancing modeling capabilities and flexibility. However, while this framework addresses the challenge of constructing a flexible transition kernel for non-Gaussian marginal distributions, it remains limited in handling excessive zeros commonly observed in real-world continuous data.

To address this limitation, we propose reconstructing the marginal distribution to account for zero-inflation. Our approach is similar to hurdle models in that it models zero and non-zero values separately. Unlike hurdle models, however, it applies a soft threshold that replaces zeros with small non-zero values rather than generating exact zeros. Building on the continuous extension (CE) approach (Denuit and Lambert 2005), this technique transforms zero-inflated marginal distributions into continuous distributions, thereby mitigating the identifiability issues that copulas face when modeling discrete or mixed marginals (Genest and Nešlehová 2007). This CE-based reformulation enables copulas to effectively capture complex dependence while accurately modeling zero-inflated continuous marginals. The proposed copula-based zero-inflated MTD model extends the copula-based MTD model by accommodating zero-inflation, thereby enhancing its applicability and flexibility for handling mixed data with excess zeros.

The rest of the chapter is organized as follows. We review several zero-inflated (ZI) count and continuous models for dependent data, as well as the continuous extension (CE) approach in Chapter 10. We present the proposed model in Chapter 11 and provide an overview of the MCMC algorithm for parameter estimation in Chapter 12. We present the results of various

simulations conducted to assess the accuracy and performance of the proposed model in Chapter 13 and discuss the model’s predictive capabilities, including uncertainty quantification, in Chapter 14. Finally, we conclude with a discussion in Chapter 15. Appendix G provides the instruction for installing the extended `mtd` R package.

Chapter 10: Background

In this section, we discuss existing approaches and a related framework that forms the basis of our proposed method. We first review the zero-inflated count and zero-inflated continuous models, which are widely used for handling zero-inflated data. We then introduce the continuous extension (CE) approach, an existing framework that has been applied to zero-inflated continuous data in spatial contexts, but not previously to our specific problem setting.

10.1 Zero-Inflated Count Models

Zero-inflated count data are prevalent across diverse domains such as finance, economics, healthcare, transportation, and ecology. Examples include claim frequencies in automobile insurance (Chowdhury et al. 2019; Zhang et al. 2022; Bermúdez and Karlis 2022; Simmachan and Boonkrong 2024; Slime et al. 2025), the number of business service firms within an airport economic zone (Jiang et al. 2018), the frequency of medical service use (Pizer and Prentice 2011; Chatterjee et al. 2018), crash counts or accident frequencies (Dong et al. 2014; Hao et al. 2016; Liu et al. 2018; Mathew and Benekohal 2021), and species abundances (Martin et al. 2005).

Accordingly, there is a rich literature on zero-inflated count models in these domains. For a comprehensive review of zero-inflated count regression models, as well as zero-inflated count

time series, spatial, and multivariate models, we refer the reader to Young, Roemmele, and Yeh (2022) and Young, Roemmele, and Shi (2022), respectively.

Our primary goal is to develop models for zero-inflated continuous time series data. To provide a foundation for this discussion, we review two zero-inflated count time series models in the next section.

10.2 Zero-Inflated Count Models for Dependent Data

10.2.1 State Space Models

Yang et al. (2015) propose a state space or dynamic model for zero-inflated count time series. Feng (2020) extends this framework to continuous-valued zero-inflated time series, resulting in the development of the dynamic semi-continuous zero-inflated (DSCZI) model.

Both the dynamic model and the MTD model include a latent state and can be classified as state space models. However, they differ in how they capture time dependence. In particular, the dynamic model introduces a continuous latent process that evolves over time according to a autoregressive (AR) process of order p , which can be equivalently represented as a p -dimentional AR(1) process. In contrast, the MTD framework represents time dependence via a set of discrete latent variables, each selecting a lag-specific kernel among L kernels. These latent variables determine which lag-specific kernel governs the current state through a random but non-dynamically evolving mechanism. As a result, while the dynamic model represents temporal evolution via a continuous, hidden state process, the MTD model captures

time dependence through the dynamics embedded in the lag-specific kernels, with selection governed by a set of discrete, static latent variables.

While the standard MTD framework assumes latent variables are independent across time, some MTD variants incorporate a dynamic latent state that evolves over time, governing by a temporal process. For example, Bartolucci and Farcomeni (2010) propose a model in which the discrete latent variables follow a hidden Markov chain and note that further generalizations, though possible, often result in models with a large number of parameters and require computationally intensive algorithms for fitting. In addition, Yang et al. (2015) relies on an expectation maximization (EM) algorithm for estimation, but with the advancement of modern computing, they suggest a full Bayesian framework using a MCMC approach for future work. In contrast, the MTD model already implements a full Bayesian framework using MCMC, allowing for efficient posterior inference.

10.2.2 Copula-Based Markov Models

Alqawba et al. (2019) and Alqawba and Diawara (2021) propose the copula-based Markov zero-inflated count time series model, utilizing marginal distributions such as the zero-inflated Poisson (ZIP), zero-inflated negative binomial (ZINB), and zero-inflated Conway-Maxwell-Poisson (ZICMP).

Similarly, the MTD and NNMP models, discussed in Chapter 3, belong to the class of first-order Markov models. However, copulas were not incorporated into these frameworks until the later work of Zheng et al. (2023b) and Zheng et al. (2023a). Even then, in the

discrete spatial NNMP models, Zheng et al. (2023a) utilize copulas in a different manner. More specifically, Alqawba et al. (2019) and Alqawba and Diawara (2021) directly compute the joint PMF of (X_t, X_{t-1}) and express it using a copula function adapted for discrete variables, from which the conditional probability is obtained by dividing by the marginal of x_{t-1} . In contrast, Zheng et al. (2023a) adopt the continuous extension approach, associating each discrete variable with a continuous variable. This enables the direct use of copulas in a continuous setting to construct the transition kernel in a structured mixture. Once the continuous variables are introduced, the conditional probability is specified as a mixture over L transition kernels, each constructed from the bivariate random vector (U_l, V_l) , with the dependence between U_l and V_l captured by a copula function.

Although copula-based Markov models have been widely applied to count and zero-inflated count data in both time series and spatial contexts, their application to zero-inflated continuous data remains largely unexplored.

10.3 Zero-Inflated Continuous models

Zero-inflated continuous data frequently appear in domains such as healthcare, insurance, environment, and transportation. While existing literature has primarily focused on zero-inflated count data, there has been relatively less attention given to zero-inflated continuous data. Nevertheless, these studies suggest promising potential for broader applications. For example, Mills (2013) conducts two-part tests for zero-inflated Gamma (ZIG) and zero-inflated log-normal (ZILN) models and applies them to assess driving risk in individuals with neurological conditions. Zhou et al. (2020) develope a two-part hidden Markov model

and apply it to analyze data from the Alzheimer’s Disease Neuroimaging Initiative (ADNI) to enhance prognosis and support early treatment. Feng (2020) applies a dynamic semi-continuous zero-inflated (DSCZI) time series model to analyze adaptive cruise control data to investigate drivers’ braking behavior, informing the in-vehicle assistance design. Sun (2020) compares the spatial Gaussian copula model with the kriging and the spatial random forests for zero-inflated forestry inventory prediction, crucial for ecosystem management. More recently, Kaewprasert et al. (2022) and Kaewprasert et al. (2024) construct Bayesian and fiducial intervals and apply them to rainfall data from northern Thailand, informing the design of disaster warning systems. Zou and Young (2024) construct fiducial-based intervals for the ZIG distribution and apply them to lipid profiles in a lung cancer study, enhancing screening and staging accuracy.

The DSCZI model by Feng (2020) is built based on the dynamic framework by Yang et al. (2015), as discussed in Section 10.2. Conditioning on the latent state, the model uses logistic regression to model the zero values and a Gamma distribution for the positive responses. For parameter estimation, the DSCZI model utilizes the data cloning method (Lele et al. 2007, 2010; Al-Wahsh and Hussein 2019), which leverages Markov chain Monte Carlo (MCMC) sampling to approximate maximum likelihood estimates, avoiding gradient-based methods due to the intractable marginal likelihood and latent variable complexity.

Although data cloning provides a practical approach for intractable likelihoods and is robust to the choice of prior distributions, it can be computationally expensive and sensitive to the choice of the number of clones (Lele et al. 2007). Moreover, convergence diagnostics can be challenging, and identifiability issues may persist even after cloning (Lele et al. 2007).

In contrast, MCMC draws samples from the full posterior distribution, providing a more comprehensive quantification of parameter uncertainty.

10.4 The Continuous Extension Approach

The continuous extension (CE) approach was first proposed by Denuit and Lambert (2005). Under the CE framework, Madsen (2009) introduces a discrete spatial Gaussian copula regression model and applies it to the Japanese beetle grub data, while Zheng et al. (2023a) develop a discrete spatial copula NNMP regression model to study North American Breeding Bird Survey data. Using this approach, each discrete random variable, Y_i , is associated with a continuous variable, Y_i^* , defined as

$$Y_i^* = Y_i - U_i, \quad (10.1)$$

where U_i follows a continuous uniform distribution on $(0, 1)$, independent of both Y_i and U_j , for $i \neq j$. The resulting Y_i^* is a continuous random variable. Not only does this continuous extension of Y_i preserves all information, but Y_i^* and Y_j^* also retain the dependence structure of Y_i and Y_j , as shown by Denuit and Lambert (2005).

Our work once again builds upon the MTD time series model by Zheng et al. (2022) and draws inspiration from the NNMP and the discrete NNMP spatial models developed by the same authors (Zheng et al. 2023b, 2023a). Additional motivation comes from the work of Monleon et al. (2019) and Sun (2020), which extend the spatial Gaussian copula model of

Madsen (2009) by adapting the CE approach for zero-inflated continuous data. Building onto these models, we propose to reconstruct the marginal distribution to accomodate for zero-inflation. We present the proposed model in the next chapter.

Chapter 11: Proposed Method: Copula-Based Zero-Inflated Gamma MTD Models

The proposed model extends the copula-based Gamma MTD model to handle zero-inflated data by reconstructing the marginal distribution. By transforming semi-continuous distributions into continuous distributions, the proposed approach addresses the issues encountered with non-continuity in the copula model, thus maintaining the same effectiveness and flexibility in modeling dependence structures as described in Chapter 4.

As stated in Definition 1, if X_j is continuous for all j , then copula function C is unique and differentiable. The joint probability density function of X_j , $f(x_j)$, can be factored into the product of the copula density, c , and the density of X_j , f_j , $j = 1, \dots, p$. However, in the case of zero-inflated gamma distribution, X_j is semi-continuous, i.e., it exhibits a point mass at zero combined with a continuous distribution over positive values.

Building on the CE framework for discrete values, zero values are replaced with non-zero values drawn from a continuous uniform distribution. The resulting distribution is continuous, effectively smoothing the zero values while preserving the overall distributional structure, including its dependence structure. We defer the details of the marginal distribution reconstruction to Section 11.2.

We use an asterisk (*) to denote that a density is CE-based. Without the asterisk, the

notation corresponds to the Gamma MTD model introduced in Part I. Based on a pre-specified stationary marginal density f_X^* , we define copulas $C_l^* = C_l$ over continuous random vectors (U_l^*, V_l^*) , with marginals $f_{U_l^*} = f_X^*$ and $f_{V_l^*} = f_X^*$, analogous to copulas in the Gamma MTD model. For $t > L$, the proposed copula-based zero-inflated Gamma MTD (ZIGamma MTD) model specifies the conditional distribution in the same form as given in (4.1) in Chapter 4.

As before, a variety of copula families are available, and the proposed model can be readily extended by reconstructing the zero-inflated continuous marginal distribution in a similar manner, provided that the resulting distribution remains within the class of continuous distributions.

11.1 Copula

We consider the Gaussian copula with the dependence parameter ρ , as described in Section 4.1. As previously noted, while the marginal distributions can be arbitrary, they are required to be continuous. In the subsequent section, we outline a technique to transform semi-continuous distributions into continuous distributions.

11.2 Marginal Distribution

To construct zero-inflated Gamma for the marginal distribution, the Gamma distribution is first reparametrized in terms of the mean, μ , and the scale parameter, β . Specifically,

$$f(y; \mu, \beta) = \frac{1}{\Gamma(\frac{\mu}{\beta})\beta^{\frac{\mu}{\beta}}} y^{\frac{\mu}{\beta}-1} \exp(-\frac{y}{\beta}) \quad y \geq 0, \quad (11.1)$$

where $\frac{\mu}{\beta} > 0$ denotes the shape and $\beta > 0$ the scale parameter.

Zero values are then replaced with non-zero values drawn from a uniform distribution. Specifically,

$$0 \leftarrow U_i. \quad (11.2)$$

where U_i follows a continuous uniform distribution on $(0, \epsilon)$ with ϵ is a data-driven parameter representing the smallest observed non-zero values. The resulting distribution, denoted as ZIGamma(μ, β, P, ϵ), is expressed as:

$$f(x; \mu, \beta, P, \epsilon) = \begin{cases} \text{Unif}(0, \epsilon) & \text{with probability } P \\ \text{ShiftedGamma}(\mu, \beta; \epsilon) & \text{with probability } 1 - P, \end{cases} \quad (11.3)$$

where μ denotes the mean and β the scale parameter of the shifted Gamma distribution, $P \in [0, 1]$ the zero-inflated probability, and $\epsilon > 0$ the threshold parameter. The shifted Gamma distribution, ShiftedGamma($\mu, \beta; \epsilon$), is a standard Gamma distribution with mean μ and scale β that is shifted to the right by ϵ , with the support $[\epsilon, \infty)$. It is expressed as:

$$f(y; \mu, \beta, \epsilon) = \frac{1}{\Gamma(\frac{\mu}{\beta})\beta^{\frac{\mu}{\beta}}} (y - \epsilon)^{\frac{\mu}{\beta}-1} \exp(-\frac{y - \epsilon}{\beta}) \quad y \geq \epsilon, \quad (11.4)$$

where $\frac{\mu}{\beta} > 0$ denotes the shape, $\beta > 0$ the scale, and $\epsilon > 0$ the threshold parameter.

Figure 11.1 shows the probability density function (PDF) of the zero-inflated gamma distribution, along with the corresponding cumulative distribution function (CDF) for fixing the parameters $\mu = 7$ and $\beta = 1$, while varying the parameters ϵ and P ($\epsilon = 0.1, 0.4$; $P = 0.1, 0.5, 0.7$). Each row of the figure corresponds to a different value of P : $P = 0.1$, 0.5, and 0.7 from top to bottom. Within each row, plot (a) shows the case for $\epsilon = 0.1$, with the left and right panels depicting the PDF and CDF, respectively. Plot (b) shows the corresponding curves for $\epsilon = 0.4$.

As also shown in the right panels in Figure 11.1, the CDF is continuous and no longer exhibits a point mass at zero, i.e., there is no longer a discontinuous jump at zero. Comparing the left and right panels we can see parameter ϵ controls the degree of the slope near the origin, where smaller value of ϵ results in steep increase in the CDF, while larger value leads to a more gradual increase. Comparing left panels from top ($P = 0.1$) to bottom ($P = 0.7$) we see the contribution of the shifted gamma distribution decreases as P increases. In other words, zero values become increasingly dominant over positive values with higher P . Additional plots are provided in the Appendix A.

While we use a Gaussian copula with a zero-inflated Gamma marginal distribution to illustrate the structure of the proposed model, the proposed model can be readily extended

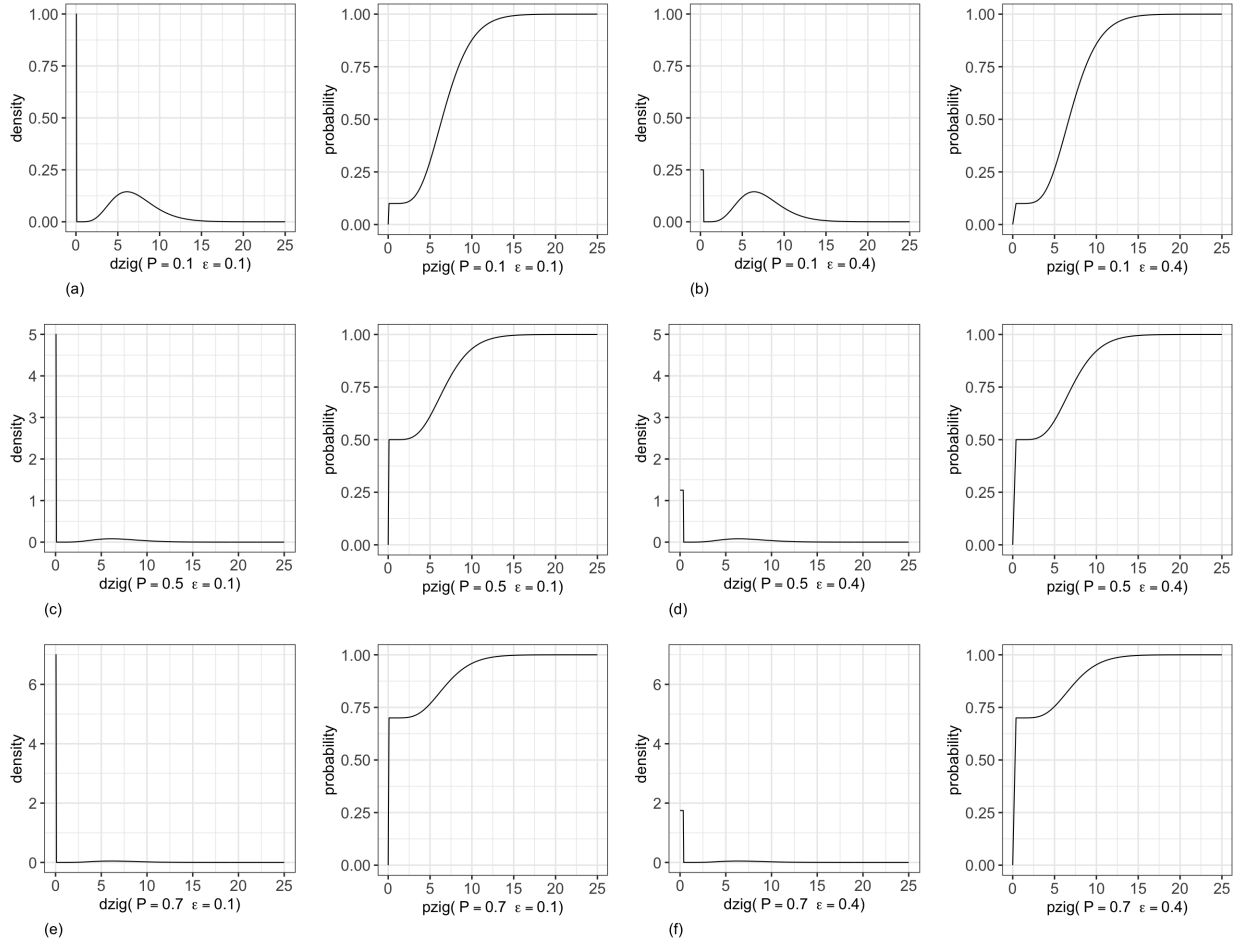


Figure 11.1: (a), (b): $ZIGamma(\mu = 7, \beta = 1, P = 0.1, \epsilon = 0.1, 0.4)$; (c), (d): $ZIGamma(\mu = 7, \beta = 1, P = 0.5, \epsilon = 0.1, 0.4)$; (e), (f): $ZIGamma(\mu = 7, \beta = 1, P = 0.7, \epsilon = 0.1, 0.4)$. (Left) Probability density function (PDF) and (Right) cumulative distribution function (CDF) of the zero-inflated gamma distribution with varying parameters.

by reconstructing the marginal distribution similarly. For example, one could construct a Gaussian copula with a zero-inflated log-normal (ZILN) MTD model or a Gumble copula with a zero-inflated Gamma (ZIGamma) MTD model, among other configurations. As copula modeling constitutes a substantial research area beyond the scope of this work, we refer the reader to Joe (2014) for more details.

Chapter 12: Overview of MCMC Algorithms

The full Bayesian model is completed by the specification of prior distributions for the parameters μ , β , P , ϵ , ρ , and w , where μ , β , P and ϵ are parameters of the zero-inflated gamma marginals, and ρ and w are the dependence and weight parameters, respectively. For the copula-based zero-inflated Gamma MTD model, the priors are specified as $Gamma(\mu|u_\mu, v_\mu)$, $Gamma(\beta|u_\beta, v_\beta)$, $Unif(P|0, 1)$, $Beta(\epsilon|5, 5)$ scaled to the interval $[0, 2\epsilon_0]$, and $Unif(\rho_l|-1, 1)$, respectively. For the cdf-based weights, the prior is $CDP(w|\alpha_0, a_0, b_0)$.

The parameters μ , β , P , ϵ , and ρ are updated using a slice sampler (Neal 2003). Following the definition in (4.1), denote $f_l(x_t|x_{t-l})$ as $f_l(x_t|x_{t-l}) = c_l(x_t, x_{t-l})f_X(x_t)$, where f_l is the transition kernel, c_l is the copula density, and f_X is the stationary marginal density. The posterior full conditional distributions for the marginal parameters μ , β , P , and ϵ are proportional to $Gamma(\mu|u_\mu, v_\mu) \prod_{t=L+1}^n f_l(x_t|x_{t-l})$ and $Gamma(\beta|u_\beta, v_\beta) \prod_{t=L+1}^n f_l(x_t|x_{t-l})$, $Unif(P|0, 1) \prod_{t=L+1}^n f_l(x_t|x_{t-l})$, and $ScaledBeta(5, 5; 0, 2\epsilon_0) \prod_{t=L+1}^n f_l(x_t|x_{t-l})$, respectively. The posterior full conditional distribution for each of the dependence parameters ρ is proportional to $Unif(\rho_l|-1, 1) \prod_{t:z_t=l} c_l(x_t, x_{t-l})$.

For the latent variables $\{z_t\}_{t=L+1}^n$, the posterior full conditional for each z_t is a discrete distribution on $\{1, \dots, L\}$, where the probability of $z_t = l$, denoted by q_l , is proportional to $w_l c_l(x_t, x_{t-l})$, for $l = 1, \dots, L$. The posterior full conditional distribution for weight parameters

w , under the cdf-based prior, is $Dirichlet(\alpha)$, where $\alpha = (\alpha_0 a_1 + M_1, \dots, \alpha_0 a_L + M_L)$.

Algorithm 2 (Figure 12.1) requires data, mtd order, hyperparameters of the priors for μ , β , ϵ , w , and starting values for μ , β , P , ϵ , ρ . It also requires tuning parameters for the slice sampler, including step size and upper bounds for μ , β , and ϵ , along with the general MCMC settings such as number of iterations, burn-in period, and thinning interval. The algorithm outputs posterior samples of μ , β , P , ϵ , ρ and w . Asterisk (**) denotes steps that differ from Algorithm 1 (Figure 5.1).

Algorithm 2 MCMC Algorithm for Parameter Estimation for Zero-Inflated Gamma MTD Models

Require: data y , mtd order L , priors for μ, β, ϵ, w , starting for $\mu, \beta, P, \epsilon, \rho$, tuning for slice sampler, mcmc settings

Ensure:

```

 $\mu$ : a vector of marginal parameters with dimension nsample = (niter − nburn)/nthin
 $\beta$ : a vector of marginal parameters with dimension nsample
 $P$ : a vector of zero-inflated probability parameters with dimension nsample
 $\epsilon$ : a vector of threshold parameters with dimension nsample
 $\rho$ : a matrix of dependence parameters with dimension  $L \times \text{nsample}$ 
 $w$ : a matrix weight parameters with dimension  $L \times \text{nsample}$ 
Initialize  $\mu, \beta, P, \epsilon, \rho, \{z_t\}_{t=L+1}^n, w$ 
for each MCMC iteration iter = 1,...,niter do
    update  $\mu$                                  $\triangleright$  Sample  $\mu$  using a slice sampler **
    update  $\beta$                                  $\triangleright$  Sample  $\beta$  using a slice sampler **
    update  $P$                                  $\triangleright$  Sample  $P$  using a slice sampler **
    update  $\epsilon$                                  $\triangleright$  Sample  $\epsilon$  using a slice sampler **
    update  $\rho$                                  $\triangleright$  Sample  $\rho_l, l = 1, \dots, L$  using a slice sampler **
    update  $\{z_t\}_{t=L+1}^n$                    $\triangleright$  Sample  $z_t, t = L + 1, \dots, n$  with probability  $q_l$  **
    update  $w$                                  $\triangleright$  Sample  $w_l, l = 1, \dots, L$  from Dirichlet(·)
end for
Discard the first nburn iterations and retain every nthin iteration
  
```

Figure 12.1: MCMC Algorithm for Parameter Estimation for Zero-Inflated Gamma MTD Models

Chapter 13: Simulation Studies

13.1 Simulation Settings

The goal of simulation studies is to assess accuracy and performance of the proposed model in Chapter 11. We explore a range of configurations by varying the parameters for weight, dependence, and marginal distribution, with particular emphasis on the zero-inflated probability.

With weight parameters w , dependence parameters for Gaussian copula ρ , mean μ , scale β , zero-inflated probability P , and threshold parameter ϵ , we generate $n = 2000$ observations from the copula-based ZIGamma MTD model. For model fitting, we set the order $L = 5$ and consider the Gaussian copula with zero-inflated gamma marginals.

We run the Gibbs sampler for 165,000 iterations, discard the first 5000 iterations as burn-in, and collect samples every 20 iterations, resulting in 8000 iterations per MCMC chain. To ensure that we can assess MCMC convergence and obtain more precise estimates of parameters, we also run four MCMC chains with 8000 iterations each for all of the following scenarios in Tables (Table 13.1, Table 13.2), which contain the description and the summary of scenarios, respectively.

In all scenarios, we use the cdf-based Dirichlet process (CDP) prior on the weights. Other

Table 13.1: Description of Scenarios for Zero-Inflated Gamma Model

Section 13.2.1: Convergence Diagnostics
- Focuses on convergence diagnostics using the Gelman-Rubin statistic and additional diagnostic tools.
- Scenario 1: Follows the same setup as the original studies.
Section 13.2.2: Weight, Dependence Parameters, w, ρ
- Focuses on weight and dependence parameters for the copula.
- Scenarios 1, 2: Follow the same setup as the original studies.
Section 13.2.3: Mean, Scale, Zero-Inflated Probability, Threshold Parameters, μ, β, P, ϵ
- Examines varying parameters for the marginal distribution.
- Scenarios 3-6: Present the usual cases.
- Scenarios 7-9: Focus on unusual cases with highly skewed distributions.

Table 13.2: Summary of Scenarios for Zero-Inflated Gamma Model

Scenario	w	ρ	μ	β	P	ϵ
1	$w_i \propto \exp(-i), i = 1, \dots, 5$	(0.7, 0.5, 0.3, 0.1, 0.1)	7	1 0.1 0.1 0.5 0.5 0.7 0.7	0.1 0.1 0.1 0.1 0.4 0.4 0.1 0.4	0.1 0.4 0.1 0.1 0.4 0.4 0.1 0.4
2	(0.2, 0.05, 0.45, 0.05, 0.25)	(0.4, 0.1, 0.7, 0.1, 0.5)	7	1 0.1 0.1 0.5 0.5 0.7 0.7	0.1 0.1 0.1 0.1 0.4 0.4 0.1 0.4	0.1 0.4 0.1 0.1 0.4 0.4 0.1 0.4
3	$w_i \propto \exp(-i), i = 1, \dots, 5$	(0.7, 0.5, 0.3, 0.1, 0.1)	4	1
4			9	1
5			4	2
6			9/2	1/2
7	$w_i \propto \exp(-i), i = 1, \dots, 5$	(0.7, 0.5, 0.3, 0.1, 0.1)	2	1
8			1	1/2
9			1/2	1/4

prior choices, such as the Dirichlet prior and the truncated stick-breaking (SB) prior are readily available, but the original MTD studies has shown that SB and CDP priors give more precise estimates.

All scenarios were initially analyzed using a single replicate. Scenarios 1 and 2 were further evaluated with multiple replicates to assess coverage and robustness. Each replicate consisted of a new synthetic dataset generated with the same underlying parameters but different random seeds. Specifically, we ran the models on 40 independently generated replicates for Scenarios 1 and 2 to evaluate the consistency and robustness of the results, ensuring comparability across scenarios.

13.2 Simulation Results

13.2.1 Convergence Diagnostics

Scenario 1 in Table 13.2 serves as an example to show and track convergence and has the same setup for w and ρ as Scenario 1 in the original MTD studies.

Tables (Table 13.3, Table 13.4, Table 13.5) present the posterior estimates and convergence diagnostics for the parameters related to weight, dependence, and marginal distribution, respectively. We defer the discussion of the estimates of the posterior mean and standard deviation (mean and SD) until a later section. There is no evidence of lack of convergence for all parameters (Gelman-Rubin statistic R and its upper CI ≤ 1.1). The simulation error of the estimates is also negligible for all parameters (Naive SE and Time-series SE are close

Table 13.3: Estimates and Gelman-Rubin Diagnostics for Scenario 1's w at Each Lag ($P = 0.1$ and $\epsilon = 0.1$)

.	Mean (SD)	R (Upper CI)	Naive SE	Time-series SE
$w_1 = 0.636$	0.6395 (0.0425)	1 (1)	0.0002	0.0003
$w_2 = 0.234$	0.1905 (0.0636)	1.01 (1.01)	0.0004	0.0013
$w_3 = 0.086$	0.1315 (0.0739)	1 (1)	0.0004	0.0021
$w_4 = 0.032$	0.0346 (0.0529)	1.01 (1.03)	0.0003	0.0017
$w_5 = 0.012$	0.0039 (0.0171)	1 (1)	0.0001	0.0004

Table 13.4: Estimates and Gelman-Rubin Diagnostics for Scenario 1's ρ at Each Lag ($P = 0.1$ and $\epsilon = 0.1$)

.	Mean (SD)	R (Upper CI)	Naive SE	Time-series SE
$\rho_1 = 0.700$	0.6847 (0.0274)	1 (1)	0.0002	0.0002
$\rho_2 = 0.500$	0.606 (0.1426)	1.01 (1.01)	0.0008	0.0027
$\rho_3 = 0.300$	0.1168 (0.2389)	1 (1)	0.0013	0.0018
$\rho_4 = 0.100$	0.0147 (0.4675)	1 (1)	0.0026	0.0027
$\rho_5 = 0.100$	-0.0046 (0.5659)	1 (1)	0.0032	0.0032

to zero).

Gelman–Rubin convergence diagnostic and ACF plots (Figure C.1, Figure C.2, Figure C.3) can be found in Appendix C Section C.1.1. In Scenario 1, the chains converge more rapidly for the parameters related to the marginal distribution, achieving convergence at around 2000 iterations. The chains converge more slowly for the parameters related to weight and dependence, especially at later lags. Nevertheless, all weight and dependence parameters reach convergence by 8000 iterations. Similar patterns emerge across all other scenarios. Trace and density plots (Figure C.4, Figure C.5, Figure C.6) are also included in Appendix C Section C.1.1.

Table 13.5: Estimates and Gelman–Rubin Diagnostics for Scenario 1 (varying P and ϵ), with true parameter values fixed at $\mu = 7$ and $\beta = 1$. The table includes all combinations of $P = 0.1, 0.5, 0.7$ and $\epsilon = 0.1, 0.4$. Specifically, the top two rows correspond to $P = 0.1$ with $\epsilon = 0.1$ and 0.4 ; the middle two rows to $P = 0.5$ with $\epsilon = 0.1$ and 0.4 ; and the final two rows to $P = 0.7$ with $\epsilon = 0.1$ and 0.4 .

.	Mean (SD)	R (Upper CI)	Naive SE	Time-series SE
μ	7.35 (0.1132)	1 (1)	0.0006	0.0006
β	1.0082 (0.0433)	1 (1)	0.0002	0.0002
P	0.0769 (0.0085)	1 (1)	0.0000	0.0000
ϵ	0.1 (7e-04)	1 (1)	0.0000	0.0000
μ	7.1454 (0.12)	1 (1)	0.0007	0.0007
β	1.0994 (0.0472)	1 (1)	0.0003	0.0003
P	0.1091 (0.0103)	1 (1)	0.0001	0.0001
ϵ	0.4017 (0.0019)	1 (1)	0.0000	0.0000
μ	6.9447 (0.1207)	1 (1)	0.0007	0.0007
β	1.0659 (0.0542)	1 (1)	0.0003	0.0003
P	0.5248 (0.0172)	1 (1)	0.0001	0.0001
ϵ	0.1001 (1e-04)	1 (1)	0.0000	0.0000
μ	6.8454 (0.1154)	1 (1)	0.0006	0.0006
β	1.0086 (0.0512)	1 (1)	0.0003	0.0003
P	0.5064 (0.0173)	1 (1)	0.0001	0.0001
ϵ	0.4 (4e-04)	1 (1)	0.0000	0.0000
μ	6.988 (0.1303)	1 (1)	0.0007	0.0007
β	0.9593 (0.0594)	1 (1)	0.0003	0.0003
P	0.6879 (0.016)	1 (1)	0.0001	0.0001
ϵ	0.0999 (1e-04)	1 (1)	0.0000	0.0000
μ	6.8482 (0.1373)	1 (1)	0.0008	0.0008
β	1.0506 (0.0665)	1 (1)	0.0004	0.0004
P	0.7048 (0.0154)	1 (1)	0.0001	0.0001
ϵ	0.4002 (3e-04)	1 (1)	0.0000	0.0000

13.2.2 Weight and Dependence Parameters for Copula

Scenarios 1 and 2 in Table 13.2 are employed to demonstrate the effectiveness of weight and dependence construction, as well as their interplay.

Scenario 1 and 2 share the same setup for w and ρ as the original MTD studies, where weight and dependence are compatible. In Scenario 1, we consider exponentially decreasing weights. In Scenario 2, we consider an uneven arrangement of the relevant lags.

As shown in (a), (b) of Figure 13.1, the results appear reasonable; that is, the estimates are consistent with the true values, with minor discrepancies. Nevertheless, the differences are minimal, and the 95% posterior credible intervals cover the true value for both weight and dependence across all lags.

Consistent with the results of the Gamma MTD model, placing greater weight on a lag yields narrower 95% posterior credible interval (CI) for that lag. When less information is available to estimate its influence, the CI widens and approaches the prior distribution.

13.2.3 Parameters for Marginal Distributions

Scenario 3 to 6 in Table 13.2 are used to evaluate the mean and the scale parameter for the zero-inflated gamma marginal distribution. Scenario 7 through 9 are used to evaluate these parameters in cases with high skewness.

In Scenario 3 to 9, we revert to the same settings for weight and dependence as used in Scenario 1. That is, we fix $w_i \propto \exp(-i)$, $i = 1, \dots, 5$ and $\rho_l = (0.7, 0.5, 0.3, 0.1, 0.1)$.

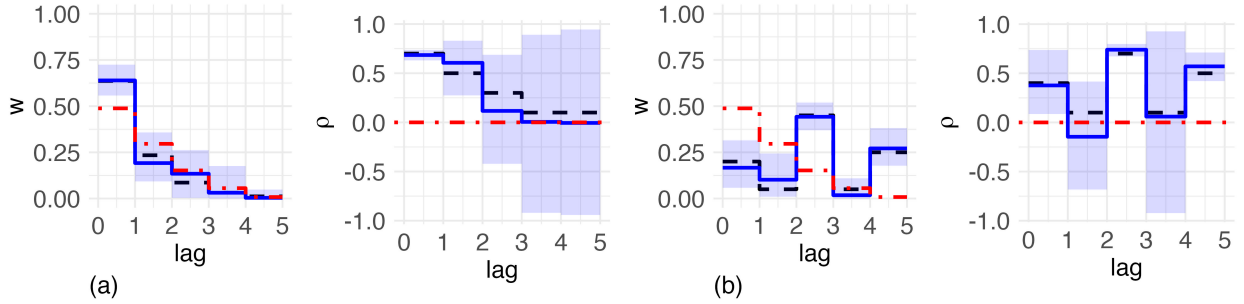


Figure 13.1: (a), (b) Results for Scenarios 1 and 2: default setup for w and ρ ($P = 0.1$ and $\epsilon = 0.1$). (Left) Dashed (black) lines are true weights, dot-dashed (red) lines are prior means, solid lines are posterior means, and (purple) polygons are 95% posterior credible intervals. (Right) Dashed (black) lines are true dependence, dot-dashed (red) lines are prior means, solid (blue) lines are posterior means, and (purple) polygons are 95% posterior credible intervals.

For the ZIGamma MTD model, the slice sampler faces similar challenges when the target distribution is not evaluable. Skewness of the target distribution may reduce sampling efficiency by inducing correlations between successive draws (Planas and Rossi 2024). To investigate this effect, we explore additional scenarios to identify where the algorithm may fail, focusing on Scenarios 7 through 9, which exhibit increasing skewness similar to that illustrated in Figure 4.1.

We present the results of Scenario 3 and Scenario 7 as examples. Each scenario consists of six cases, covering all combinations of $P = 0.1, 0.5, 0.7$, and $\epsilon = 0.1, 0.4$. As shown in Tables (Table 13.6, Table 13.7), the results appear reasonable; that is, convergence has been achieved and the estimates are consistent with the true values.

To demonstrate how plots showing the marginal results for the Gamma MTD model in Appendix B Section B.1.3 can be generated for the ZIGamma MTD model, we include example plots for Scenario 1 in Appendix C Section C.1.3: the simulated data in Figure C.7

and the results overlaid on the simulated data in Figure C.8.

13.2.4 Coverage Assessment

To compute coverage rates, for each of the 40 replicates, we first combine the four chains of 8000 posterior samples per parameter, then calculate the 95% credible interval from the combined samples, and record whether the true parameter value falls within this interval. The overall coverage is the proportion of replicates for which the true value is contained within the interval.

As shown in Tables (Table 13.8 and Table 13.9), the 95% credible intervals for all parameters successfully contain the true values in most replicates across both scenarios. Most parameters achieve full coverage, with a few slightly below 1, indicating that the credible intervals reliably capture the true parameter values. Importantly, the lengths of the credible intervals vary across parameters, reflecting differences in estimation uncertainty.

Table 13.6: Estimates and Gelman–Rubin Diagnostics for Scenario 3 (varying P and ϵ), with true parameter values fixed at $\mu = 4$ and $\beta = 1$. The table includes all combinations of $P = 0.1, 0.5, 0.7$ and $\epsilon = 0.1, 0.4$. Specifically, the top two rows correspond to $P = 0.1$ with $\epsilon = 0.1$ and 0.4 ; the middle two rows to $P = 0.5$ with $\epsilon = 0.1$ and 0.4 ; and the final two rows to $P = 0.7$ with $\epsilon = 0.1$ and 0.4 .

.	Mean (SD)	R (Upper CI)	Naive SE	Time-series SE
μ	4.2622 (0.0862)	1 (1)	0.0005	0.0005
β	1.0153 (0.0446)	1 (1)	0.0002	0.0003
P	0.0769 (0.0085)	1 (1)	0.0000	0.0000
ϵ	0.1 (7e-04)	1 (1)	0.0000	0.0000
μ	4.2545 (0.0927)	1 (1)	0.0005	0.0029
β	1.0345 (0.1744)	1 (1)	0.0010	0.0285
P	0.0778 (0.0116)	1 (1)	0.0001	0.0011
ϵ	0.4003 (0.0328)	1 (1)	0.0002	0.0041
μ	4.2381 (0.0952)	1 (1)	0.0005	0.0005
β	1.051 (0.0532)	1 (1)	0.0003	0.0003
P	0.476 (0.0178)	1 (1)	0.0001	0.0001
ϵ	0.0999 (1e-04)	1 (1)	0.0000	0.0000
μ	4.2375 (0.0951)	1 (1)	0.0005	0.0005
β	1.0511 (0.0532)	1 (1)	0.0003	0.0003
P	0.4761 (0.0178)	1 (1)	0.0001	0.0001
ϵ	0.3996 (4e-04)	1 (1)	0.0000	0.0000
μ	4.2018 (0.1017)	1 (1)	0.0006	0.0006
β	1.0101 (0.0604)	1 (1)	0.0003	0.0003
P	0.6674 (0.016)	1 (1)	0.0001	0.0001
ϵ	0.1 (1e-04)	1 (1)	0.0000	0.0000
μ	4.2017 (0.1022)	1 (1)	0.0006	0.0006
β	1.0102 (0.0608)	1 (1)	0.0003	0.0003
P	0.6673 (0.016)	1 (1)	0.0001	0.0001
ϵ	0.4001 (3e-04)	1 (1)	0.0000	0.0000

Table 13.7: Estimates and Gelman–Rubin Diagnostics for Scenario 7 (varying P and ϵ), with true parameter values fixed at $\mu = 2$ and $\beta = 1$. The table includes all combinations of $P = 0.1, 0.5, 0.7$ and $\epsilon = 0.1, 0.4$. Specifically, the top two rows correspond to $P = 0.1$ with $\epsilon = 0.1$ and 0.4 ; the middle two rows to $P = 0.5$ with $\epsilon = 0.1$ and 0.4 ; and the final two rows to $P = 0.7$ with $\epsilon = 0.1$ and 0.4 .

.	Mean (SD)	R (Upper CI)	Naive SE	Time-series SE
μ	2.181 (0.0623)	1 (1)	0.0003	0.0003
β	1.0256 (0.0475)	1 (1)	0.0003	0.0003
P	0.0771 (0.0085)	1 (1)	0.0000	0.0000
ϵ	0.1 (6e-04)	1 (1)	0.0000	0.0000
μ	2.0907 (0.0676)	1 (1)	0.0004	0.0008
β	1.1278 (0.0826)	1 (1)	0.0005	0.0113
P	0.1065 (0.0144)	1 (1)	0.0001	0.0016
ϵ	0.3865 (0.0581)	1 (1)	0.0003	0.0112
μ	1.9803 (0.0656)	1 (1)	0.0004	0.0004
β	1.0664 (0.0586)	1 (1)	0.0003	0.0003
P	0.525 (0.0172)	1 (1)	0.0001	0.0001
ϵ	0.1001 (1e-04)	1 (1)	0.0000	0.0000
μ	1.9212 (0.0616)	1 (1)	0.0003	0.0003
β	1.0043 (0.0542)	1 (1)	0.0003	0.0003
P	0.5064 (0.0173)	1 (1)	0.0001	0.0001
ϵ	0.4 (4e-04)	1 (1)	0.0000	0.0000
μ	1.99 (0.0701)	1 (1)	0.0004	0.0004
β	0.9605 (0.0624)	1 (1)	0.0003	0.0003
P	0.6879 (0.0159)	1 (1)	0.0001	0.0001
ϵ	0.0999 (1e-04)	1 (1)	0.0000	0.0000
μ	1.9303 (0.0735)	1 (1)	0.0004	0.0004
β	1.0389 (0.0704)	1 (1)	0.0004	0.0004
P	0.7057 (0.0153)	1 (1)	0.0001	0.0001
ϵ	0.4002 (3e-04)	1 (1)	0.0000	0.0000

Table 13.8: Coverage Rates for All Parameters Across 40 Replicates for Scenario 1 (varying P and ϵ), with true parameter values fixed at $\mu = 7$ and $\beta = 1$. The table includes all combinations of $P = 0.1, 0.5, 0.7$ and $\epsilon = 0.1, 0.4$. Specifically, the top two rows correspond to $P = 0.1$ with $\epsilon = 0.1$ and 0.4 ; the middle two rows to $P = 0.5$ with $\epsilon = 0.1$ and 0.4 ; and the final two rows to $P = 0.7$ with $\epsilon = 0.1$ and 0.4 .

μ	β	P	ϵ	w_1	w_2	w_3	w_4	w_5	ρ_1	ρ_2	ρ_3	ρ_4	ρ_5
0.95	0.93	0.95	0.93	0.93	0.93	1.00	1.00	1.00	0.88	1.00	1.00	0.97	1.00
0.97	0.97	0.97	0.93	0.95	0.95	0.97	1.00	0.97	0.97	1.00	1.00	0.97	1.00
0.95	0.95	0.93	0.97	0.88	0.95	1.00	1.00	0.93	0.93	1.00	1.00	1.00	1.00
0.97	0.93	0.95	1.00	0.95	1.00	1.00	1.00	0.93	0.88	0.97	1.00	1.00	1.00
0.95	0.95	0.93	0.97	1.00	1.00	1.00	1.00	0.95	0.93	1.00	1.00	1.00	1.00
0.93	1.00	1.00	0.93	0.95	0.93	0.95	0.97	0.95	1.00	0.97	1.00	0.97	1.00

Table 13.9: Coverage Rates for All Parameters Across 40 Replicates for Scenario 2 (varying P and ϵ), with true parameter values fixed at $\mu = 7$ and $\beta = 1$. The table includes all combinations of $P = 0.1, 0.5, 0.7$ and $\epsilon = 0.1, 0.4$. Specifically, the top two rows correspond to $P = 0.1$ with $\epsilon = 0.1$ and 0.4 ; the middle two rows to $P = 0.5$ with $\epsilon = 0.1$ and 0.4 ; and the final two rows to $P = 0.7$ with $\epsilon = 0.1$ and 0.4 .

μ	β	P	ϵ	w_1	w_2	w_3	w_4	w_5	ρ_1	ρ_2	ρ_3	ρ_4	ρ_5
0.93	0.95	0.93	0.90	1.00	0.97	0.97	1.00	0.97	1.00	0.97	0.97	1.00	0.97
0.88	0.95	0.95	0.88	1.00	1.00	0.97	1.00	0.93	0.97	0.95	0.97	1.00	1.00
0.93	0.95	0.95	0.95	1.00	1.00	0.97	1.00	0.95	1.00	0.97	1.00	1.00	0.97
0.95	0.97	0.88	0.97	1.00	1.00	0.93	1.00	0.97	1.00	1.00	1.00	1.00	0.97
0.95	0.95	0.90	0.97	1.00	1.00	0.97	1.00	0.88	1.00	0.95	0.95	1.00	0.90
0.97	0.95	0.97	0.95	1.00	1.00	1.00	1.00	0.97	1.00	0.97	0.97	1.00	1.00

Chapter 14: Prediction

Table 14.1 and Table 14.2 summarize the 95% one-step ahead posterior predictive intervals for Scenario 1 and 2, respectively. The overall coverage can obscure important differences in predictive performance. To provide a clearer picture, we decompose the coverage into **below** (i.e., the coverage for values less than or equal to ϵ) and **above** (i.e., the coverage for values greater than ϵ). As shown in these tables, when the zero-inflated probability is low (e.g., $P = 0.1$), the empirical coverage **above** is a more informative metric for assessing predictive performance. As P increases (e.g., $P = 0.5, 0.7$), the empirical coverage **below** becomes increasingly dominant.

When P is small, a large proportion of observations fall above ϵ , providing more information to estimate coverage in the upper range. As P increases, more observations concentrate below ϵ , making the coverage in the near-zero range the primary indicator of the overall performance. This shift reflects the change in the underlying data distribution, where increasing P results in a higher proportion of near-zero values. Similar patterns are observed across all scenarios considered in the simulation study. Figure 14.1 and Figure 14.2 convey the same findings but present the empirical coverage as time series for Scenario 1 and 2, respectively. Additional plots for Scenario 3 through 9 are provided in the Appendix E.

Table 14.1: Empirical coverage of the 95% predictive intervals for ZIGamma Scenario 1 (varying P and ϵ). Each row label indicates the combination of P (zero-inflated probability) and ϵ (threshold value) used in the simulation. Reported values show overall empirical coverage, with decomposed coverage below and above the threshold.

	Coverage	Below	Above
P01Eps01	0.9549	0.6944	0.9751
P01Eps04	0.9148	0.3973	0.9786
P05Eps01	0.9278	0.9876	0.8615
P05Eps04	0.9484	0.9681	0.9285
P07Eps01	0.8677	0.9943	0.5726
P07Eps04	0.9298	0.9888	0.7828

Table 14.2: Empirical coverage of the 95% predictive intervals for ZIGamma Scenario 2 (varying P and ϵ). Each row label indicates the combination of P (zero-inflated probability) and ϵ (threshold value) used in the simulation. Reported values show overall empirical coverage, with decomposed coverage below and above the threshold.

	Coverage	Below	Above
P01Eps01	0.9479	0.6382	0.9734
P01Eps04	0.9243	0.4038	0.9849
P05Eps01	0.9283	0.9972	0.8458
P05Eps04	0.9519	0.9661	0.9374
P07Eps01	0.9108	0.9972	0.6953
P07Eps04	0.9333	0.9885	0.7778

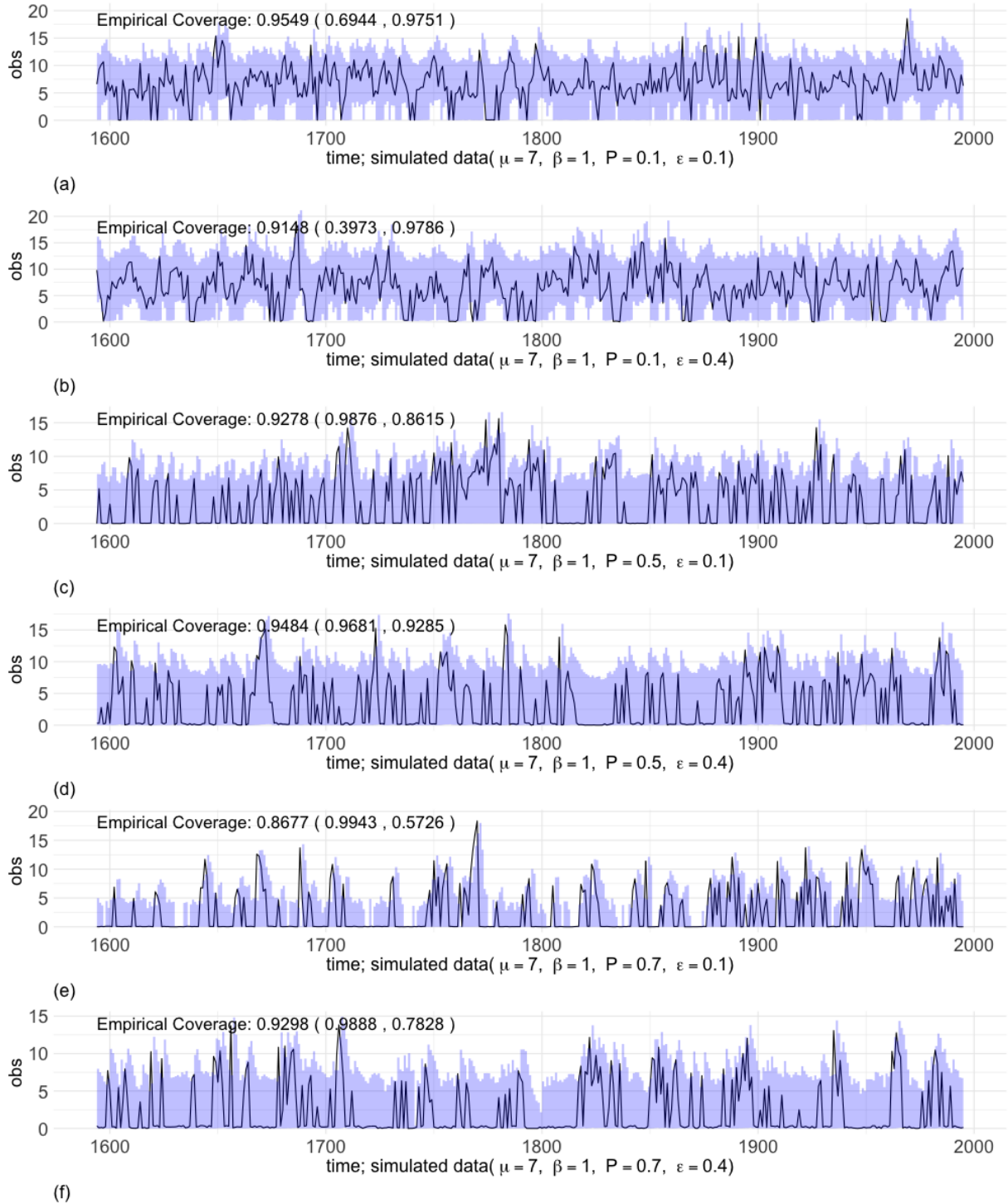


Figure 14.1: 95% one-step ahead posterior predictive intervals for ZIGamma Scenario 1 (varying P and ϵ). Reported values show overall empirical coverage, with decomposed coverage below and above the threshold shown in parentheses: coverage (coverage for data $\leq \epsilon$, coverage for data $> \epsilon$).

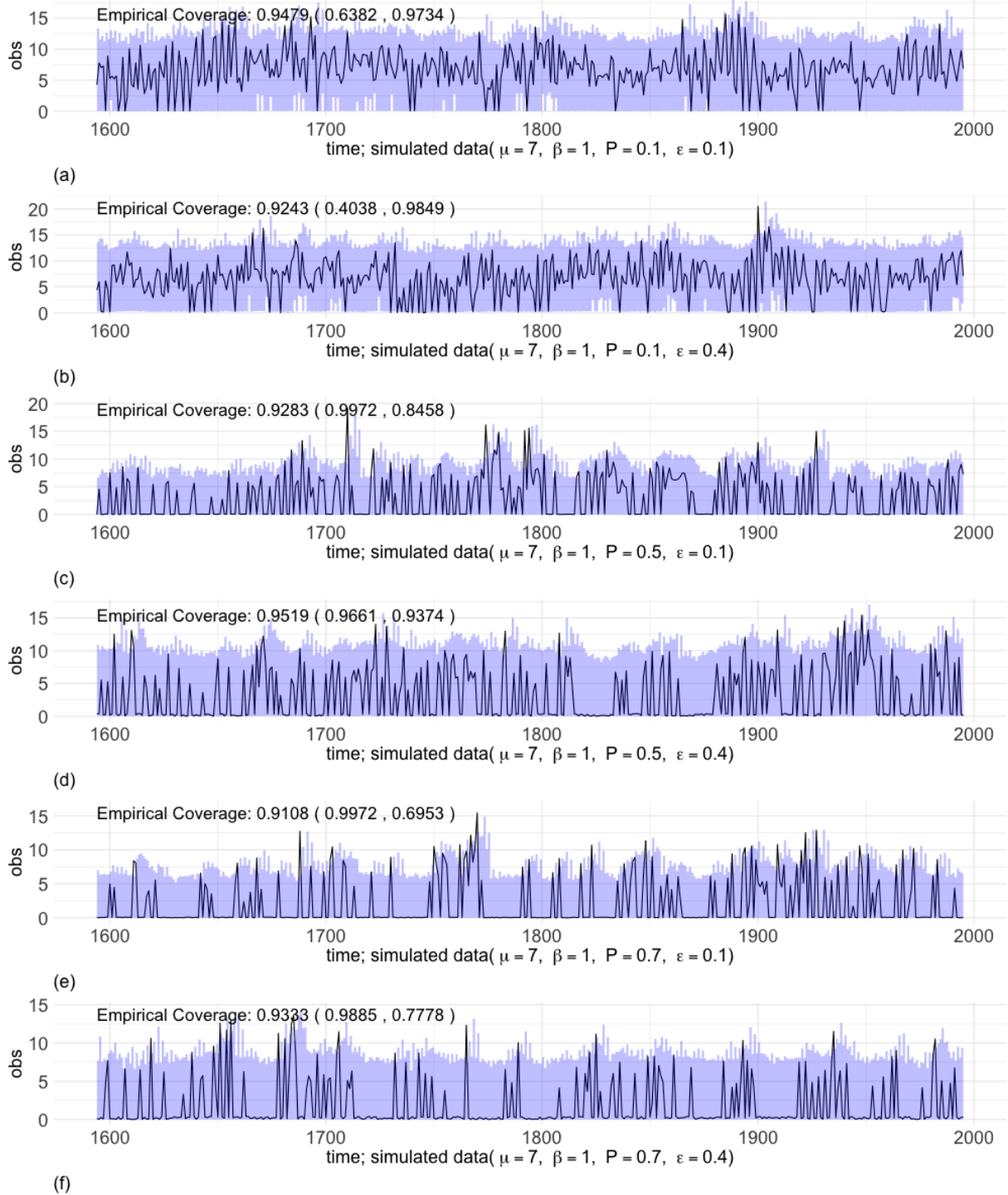


Figure 14.2: 95% one-step ahead posterior predictive intervals for ZIGamma Scenario 2 (varying P and ϵ). Reported values show overall empirical coverage, with decomposed coverage below and above the threshold shown in parentheses: coverage (coverage for data $\leq \epsilon$, coverage for data $> \epsilon$).

Chapter 15: Discussion

In this part of the dissertation, we review existing models for zero-inflated dependent count and continuous data, as well as the continuous extension approach, and propose a novel copula-based zero-inflated MTD model that extends the existing framework. We also present the algorithms and simulation studies, which demonstrate promising results across various scenarios. The advantage of our proposed approach is that, by reconstructing semi-continuous distributions into continuous forms, it preserves the effectiveness of copula modeling for capturing dependence structures, while retaining flexibility in the selection of marginal distributions in zero-inflated continuous settings.

We treat the threshold parameter as a variable rather than fixing it. The threshold is a nuanced parameter that can influence model outcome, and fixing it arbitrarily might overlook important variations in performance. Future work could include a sensitivity analysis to evaluate how changes in the threshold affect model performance.

In real-world settings, dependence structures often exhibit features such as tail dependence or asymmetry that cannot be adequately captured by the Gaussian copula. Further research should explore alternative copula families, such as the Clayton or Gumbel copulas, along with efficient estimation techniques and practical applications, to better capture complex dependence patterns in empirical data.

Although the framework can be readily extended to handle non-stationary time series and incorporate predictors (Zheng et al. 2022), these features are not currently implemented. Consequently, it cannot adequately model non-stationary data with trends and seasonality, limiting its practical effectiveness. In addition, the lack of support for covariate prevents the model from jointly capturing the effects of past observations and relevant covariate. A key future direction is to extend the framework for non-stationary and regression-based settings. Such an extension would enable the model to handle changing dynamics and incorporate both sources of information, thereby improving its flexibility and applicability to real-world data.

Finally, we use MCMC as our primary sampling method, but alternative approaches such as Variational Inference or Sequential Monte Carlo could also be explored. These alternatives offer different trade-offs between computational efficiency and approximation accuracy. Future work could involve a comparison of these methods to assess how the choice of sampling strategy impacts model performance.

Part III

**Copula-Based Markov MTD Models
vs. Deep Learning LSTM Networks**

Chapter 16: Introduction

Recurrent Neural Networks (RNNs) ([Rumelhart et al. 1986](#)), and their variants, Long Short-Term Memory (LSTMs), are widely used for modeling sequence data because of their ability to capture both short- and long-term dependencies. In natural language processing, they have been successfully applied to tasks such as handwriting recognition ([Graves et al. 2008](#)), language modeling ([Mikolov 2012](#)), speech recognition ([Chan et al. 2015; Chiu et al. 2017](#)), and machine translation ([Sutskever et al. 2014; Bahdanau et al. 2014](#)). Beyond language, RNNs and LSTMs have also shown effective in complex time series forecasting and have been employed for applications including financial market prediction ([Siami-Namini et al. 2019; Muncharaz 2020; Pirani et al. 2022](#)), energy forecasting ([Manero et al. 2018; Sandhu et al. 2019; Yunjun Yu et al. 2019; Paramasivan 2021](#)), weather and climate modeling ([Salman et al. 2018; Haq 2022](#)), and epidemiological trend analysis ([Chimmula and Zhang 2020; Wang et al. 2020](#)).

However, previous studies comparing LSTMs to traditional models often claim LSTM superiority, a conclusion that can be misleading when the benchmarks chosen are inappropriate. For example, LSTMs are frequently compared to autoregressive integrated moving average (ARIMA) models, even when the assumptions underlying ARIMA models such as stationarity and normally distributed errors are not satisfied ([Hewamalage et al. 2023a](#)). An early survey also reported mixed results, showing that RNNs including LSTMs outperform classical

benchmarks on some datasets and metrics, but not consistently (Hewamalage et al. 2021). Similar concerns have also been raised in discussions of newer foundation-model approaches (Bergmeir 2024b). These observations highlight the need to evaluate deep learning models against more flexible probabilistic alternatives.

In line with this, both probabilistic and deep learning models have been shown to be effective for forecasting univariate time series. For example, a prior study (Hassan 2021) demonstrated that the probabilistic MTD model and the deep learning LSTM network achieved similar predictive accuracy in modeling disease spread, with both slightly outperforming classical ARIMA models. These findings suggest that both probabilistic and deep learning approaches hold promise, yet their relative strengths under varying data conditions remain underexplored in the univariate setting within the statistics and machine learning (ML) literature.

To address the concerns about benchmark limitations and to investigate the relative performance of probabilistic and deep learning models, we conduct a rigorous comparison of LSTM and MTD models in the univariate setting. Unlike prior work that benchmarks LSTMs primarily against mis-specified linear models such as ARIMA, we evaluate LSTM against a probabilistic alternative that does not require restrictive assumptions and is better suited to non-linear, non-Gaussian dynamics. Our controlled simulations focus on stationary but non-Gaussian data-generating processes, systematically varying conditions such as marginal skewness, dependency structure, and zero-inflation to assess each model’s strengths and weaknesses. We then complement these simulations with a real-world data application to provide a grounded assessment of practical forecasting performance.

The rest of the chapter is organized as follows. We review RNN and LSTM architectures and their foundational concepts, and provide an overview of training, hyperparameter tuning, and evaluation metrics in Chapter 17. Simulation results comparing MTDs and LSTMs are presented in Chapter 18, followed by results from the real-world data application in Chapter 19. Finally, we conclude with a discussion in Chapter 20.

Chapter 17: Background

17.1 Recurrent Neural Network (RNN) Architecture

17.1.1 Recurrent Unit

An Recurrent Neural Network (RNN) is composed of repeating cells or units that unfold or unroll over time, where each unit passes recurrent information stored in the hidden state from one time step to the next. Figure 17.1 presents a visual representation of an RNN unit.

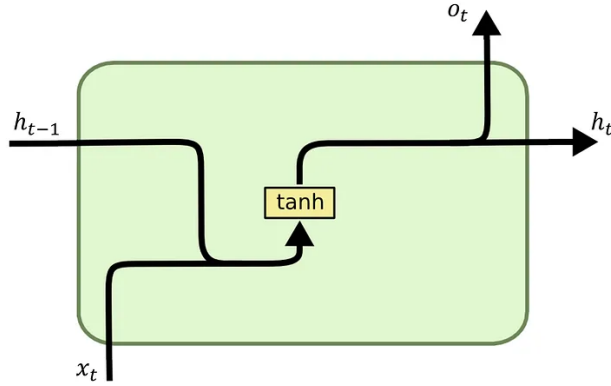


Figure 17.1: Architecture of an RNN unit, reproduced from Olah (2015). x_t is the input, h_t is the hidden state, and o_t is the output. tanh is the activation function, squashing values to $(-1, 1)$ for stability and zero-centered output.

An RNN unit computes a weighted combination of input data, x_t , and the previous hidden state, h_{t-1} , applies an activation function, and updates the hidden state to h_t . Let x_t , h_t , and o_t denote the input data, the hidden state, and the output at time t , respectively. Then,

an RNN unit can be expressed as:

$$\begin{aligned} h_t &= f(W_{ih}h_{t-1} + W_{ix}x_t + b_i), \\ o_t &= g(W_{oh} \cdot h_t + b_o), \end{aligned} \tag{17.1}$$

where W_{ix} , W_{ih} and W_{oh} denote the weight matrices, and b_i and b_o the bias vectors. The subscripts i and o indicate their steps in RNN: i refer to the input/hidden step (first line in (17.1)), and o to the output step (second line in (17.1)). f and g denote the activation functions for the hidden layer and output layer, respectively. f is typically set to the logistic sigmoid function, denoted as σ , which outputs values in range $(0, 1)$ to act as a gate that controls how much information passes through. g is the hyperbolic tangent function, denoted as \tanh , which outputs values in range $(-1, 1)$ to generate output in a stable, zero-centered range.

17.1.2 Problems with Long-Term Dependence

When trained on long sequences, RNNs are prone to the well-documented vanishing gradient issue ([Bengio et al. 1994](#)). Both vanishing and exploding issues can introduce instability during training and hinder the ability of standard RNNs to capture long-term dependence in sequence data. In the vanishing case, gradients become too small to effectively update network weights, while in the exploding case, gradients grow excessively large, leading to unstable weight updates.

To capture long-term dependence in sequence data while alleviating the vanishing gradient problem, Hochreiter and Schmidhuber (1997) introduce the Long Short-Term Memory (LSTM) unit. Since this introduction, several LSTM variants have been developed. Notable variants include LSTM with a forget gate (Gers et al. 2000), LSTM with peephole connections (Gers and Schmidhuber 2000), and gated recurrent unit (GRU) (Cho et al. 2014).

While LSTMs effectively address the vanishing gradient problem and capture long-term dependencies, recent advances in sequence modeling have introduced transformer-based foundation models, which approach the problem with a fundamentally different architecture.

17.1.3 A Note on Foundation Models such as Transformers

Foundation models, or large pre-trained models, are general-purpose AI systems trained on large, diverse datasets to learn broad patterns before fine-tuning on specific tasks. This pretraining framework has enabled their widespread adoption across domains. Their rise followed the success of large language models like BERT (Devlin et al. 2019) and GPT-3 (Brown et al. 2020). Typically built on the transformer architecture (Vaswani et al. 2017), these models have excelled in natural language processing (NLP) and computer vision, with extensions to multi-modal and reinforcement learning. Recently, foundation models have been increasingly applied to forecasting tasks, particularly in time series analysis. Notable domain-specific models include TimeGPT-1 by Nixtla (Garza et al. 2024), Lag-Llama (Rasul et al. 2024), TimesFM by Google Research (Das et al. 2024), Tiny Time Mixers by IBM Research (Ekambaram et al. 2024), Moirai by Salesforce (Woo et al. 2024), and Chronos by Amazon Web Services(Ansari et al. 2024).

These trends highlight the growing preference for transformer architectures in sequence modeling. Unlike RNNs and LSTMs, which process data *sequentially* via BPTT, transformers leverage multi-head attention with positional encoding to capture dependencies *in parallel*. Recurrent units are replaced with stacked encoder and decoder layers, each followed by feed-forward neural network layers, resulting in improved training efficiency and stability. For an overview of the transformer architecture and its applications in time series forecasting, see Ahmed et al. (2023). For a comprehensive survey of foundation models, see Liang et al. (2024).

As with many deep learning architectures, transformer-based models require large datasets to train effectively and are prone to overfitting, whereas simpler architectures like LSTMs often perform well on smaller datasets, offering easier training and tuning for practical forecasting tasks. Developing robust and interpretable transformer architectures remains a challenge, and benchmarking issues persist (Hewamalage et al. 2023b; Bergmeir 2024a). Nonetheless, transformers hold strong potential for advancing areas of ML, including time series forecasting.

Despite the emergence of transformer-based models, LSTMs remain a practical and effective choice for our experiments, and our discussion focus on the LSTM architecture with a forget gate (Gers et al. 2000). We distinguish between two related decisions: the choice of LSTM variant and the choice of network architecture.

First, we select the LSTM with a forget gate because it is the version that is implemented in PyTorch, a widely used framework for deep learning research and development. Furthermore,

while several variants of the vanilla LSTM exist, such as the LSTM with peephole connections (Gers and Schmidhuber 2000) and gated recurrent unit (GRU) (Cho et al. 2014), a comprehensive study has shown that these variants generally offer comparable performance (Greff et al. 2016). For a comprehensive list of vanilla LSTM variants, we refer the reader to Yong Yu et al. (2019) and Hewamalage et al. (2021).

Second, we choose LSTMs over transformer-based architectures because LSTMs are better suited for smaller datasets, require fewer computational resources, and are easier to train and tune. In contrast, transformer-based foundation models often demand much larger datasets and substantial computing power to perform optimally, making LSTMs a more practical choice for our forecasting experiments. Moreover, LSTMs provide a simpler foundation for sequence modeling, forming the conceptual basis for transformer architectures. By starting with LSTMs, we gain more control over the training process and a clearer understanding of model behavior.

17.2 Long Short-Term Memory (LSTM) Network Architecture

17.2.1 LSTM Units

An Long Short-Term Memory (LSTM) unit extends an RNN by introducing a cell state and three gates: the forget gate, the input gate, and the output gate. The cell state carries long-term dependence, while the hidden state encodes short-term patterns. The gates regulate the flow of information by determining how much of the previous cell state should be forgotten, how much new information should be added, and how much of the updated cell state should

be passed to the hidden state at each time step. Figure 17.2 presents a visual representation of an LSTM unit.

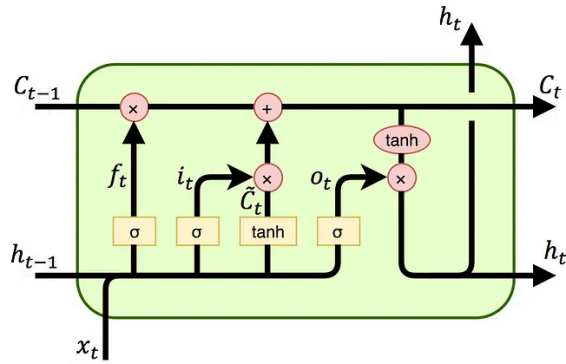


Figure 17.2: Architecture of an LSTM unit with a forget gate, reproduced from Olah (2015). x_t is the input, h_t the hidden state, and c_t the cell state. f_t , i_t , and o_t are the forget, input, and output gates, respectively. σ is used to squash values to $(0, 1)$ for gating, while \tanh squashes values to $(-1, 1)$ for stability and zero-centered output.

An LSTM unit processes the input data, x_t , and the previous hidden state, h_{t-1} , and the cell state, c_{t-1} , through several gating mechanisms, updates the cell state to c_t and the hidden state to h_t . Let c_t and h_t denote the cell and the hidden state vector. Let f_t , i_t , and o_t represent the forget, the input, and the output gate vector at time t , respectively. Then, an LSTM unit can be expressed as:

$$\begin{aligned}
f_t &= \sigma(W_{fh}h_{t-1} + W_{fx}x_t + b_f), \\
i_t &= \sigma(W_{ih}h_{t-1} + W_{ix}x_t + b_i), \\
\tilde{c}_t &= \tanh(W_{ch}h_{t-1} + W_{cx}x_t + b_c), \\
c_t &= f_t \cdot c_{t-1} + i_t \cdot \tilde{c}_t, \\
o_t &= \sigma(W_{oh}h_{t-1} + W_{ox}x_t + b_o), \\
h_t &= o_t \cdot \tanh(c_t),
\end{aligned} \tag{17.2}$$

where W denotes the weight matrices, b the bias vectors, σ the logistic sigmoid function, and \tanh the hyperbolic tangent function.

The internal structure of an LSTM unit consists of several components that work together to regulate information flow at each time step t :

1. The forget gate, f_t , controls the extent to which information is discarded or retained. The forget gate outputs values in range $(0, 1)$, where 0 means the information is completely discarded, and 1 means it is fully retained. The values never reach 0 or 1, since the range is exclusive.
2. The input gate, i_t , regulates the amount of new information to add. The input gate outputs values in range $(0, 1)$, where 0 means no information is added, and 1 means it is nearly fully added. The values never reach 0 or 1, since the range is exclusive.
3. The network computes the candidate values, \tilde{c} , which represents the proposed new

information.

4. Next, the cell state, c_t , is updated by combining the previous cell state, c_{t-1} , and the candidate values, \tilde{c} . As previously mentioned, f_t controls how much irrelevant information to discard, while i_t determines how much new information to incorporate when updating the cell state.
5. Then, the output gate, o_t , determines the extent to which the cell state, c_t , is exposed to the hidden state, h_t .
6. The hidden state, h_t , is updated by taking the cell state, c_t , and scaling it with the output gate, o_t . This resulting hidden state, h_t , is the final output of the LSTM network at time t .

To produce the output, \hat{y}_t , a fully connected layer, where every neuron is connected to every neuron in the previous layer, is applied to the hidden state, h_t . This layer performs a linear transformation, effectively mapping the high-dimensional representation learned by the LSTM to the target output space. For regression tasks, the output is typically a single scalar representing the prediction, and no non-linear activation is applied, allowing the network to generate an unconstrained real value.

17.3 Training, Hyperparameter Tuning, and Metrics

During training, forward pass involves passing input data, x_t , through the network to generate a predicted value, \hat{y}_t , for each time step from $t = 1$ to T , as outlined in the steps above

in Section 17.2.1. The error is then calculated using a loss function, which measures the discrepancy between the predicted output, \hat{y}_t , and the target value, y_t . The total loss is computed by summing up the loss over time:

$$\mathcal{L}(\hat{y}, y) = \sum_{t=1}^T \ell(\hat{y}_t, y_t), \quad (17.3)$$

where \mathcal{L} represents the overall loss accumulated over time and ℓ_i the loss at each time step t .

Backpropagation involves propagating the error backward through the network, from time step $t = T$ to 1, and computing the gradients of the objective function with respect to each parameter in the network. These gradients guide how the network parameters should be updated in order to minimize the loss. For sequence-based models, such as RNNs, LSTMs, and GRUs, the Backpropagation Through Time (BPTT) procedure (Werbos 1988; Werbos 1990) is employed as an extension of the standard backpropagation algorithm. BPTT unfolds the network across time steps, allowing the computation of gradients for the entire sequence of inputs. For the specific derivation of LSTM gradients, we refer the reader to Chen (2016) and Sherstinsky (2020).

Once the gradients are computed using BPTT, standard gradient-based optimization techniques, such as Stochastic Gradient Descent (SGD) and Adaptive Moment Estimation (Adam) (Kingma and Ba 2014), can be used to update the parameters in the direction that minimizes loss. The following update rule reflects the basic form of SGD, where parameters are adjusted

using the gradient, scaled by the learning rate:

$$\theta \leftarrow \theta - \alpha \nabla_{\theta} \mathcal{L}, \quad (17.4)$$

where $\theta = \{W_{fx}, W_{ix}, W_{\tilde{c}x}, W_{ox}, W_{fh}, W_{ih}, W_{\tilde{c}h}, W_{oh}, b\}$ in (17.2) denotes the set of network parameters, with b representing all bias vectors collectively, α the learning rate, and $\nabla_{\theta} \mathcal{L}$ the gradient of the loss function with respect to θ .

The process of forward pass, backpropagation, and parameter updates is repeated over multiple epochs until convergence. Convergence is typically determined by stopping criterion such as early stopping based on validation loss, reaching a predefined number of epochs, and when the improvement in loss between epochs falls below a specified threshold ([Goodfellow et al. 2016](#)).

Hyperparameter tuning plays a crucial role in improving model performance. Key hyperparameters include, for example:

1. Batch Size
2. Number of Epochs
3. Learning Rate
4. Number of Hidden Units or Cell Dimension
5. Number of Hidden Layers, etc.

Batch size refers to the number of training samples or sequences processed simultaneously by the network in one forward and backward pass before updating its parameters. An epoch is one complete pass through the entire training dataset, during which the network processes all batches once, performing one forward and one backward pass per batch. The number of epochs refers to the number of passes the network iterates over the full dataset to achieve optimal training of the RNN.

The learning rate controls how much the network's parameters are adjusted during training in response to the gradients of the loss function. The effectiveness of the learning rate often depends on the optimizer used.

The cell dimension and the number of hidden layers are two additional hyperparameters that define the structure of the RNN architecture. The cell dimension refers to the size of the hidden state vector, which corresponds to the number of neurons or nodes inside each RNN cell. The number of hidden layers determines how many recurrent layers are stacked on top of each other.

Hyperparameter tuning can be performed manually through hand tuning or automatically using methods such as grid search and random search ([Bergstra and Bengio 2012](#)). Manual search, also known as manual hyperparameter tuning, involves adjusting hyperparameters based on commonly used defaults, insights from prior literature, and feedback from model performance, while automated tuning involves systematically searching the hyperparameter space. Grid search exhaustively evaluates all possible combinations within a predefined set of hyperparameter values, while random search samples hyperparameter values randomly from

Table 17.1: Common metrics for evaluating forecasting models.

Metric	Definition	Formula
RMSE	Root Mean Squared Error	$\sqrt{\frac{1}{T} \sum_{t=1}^T (y_t - \hat{y}_t)^2}$
MAE	Mean Absolute Error	$\frac{1}{T} \sum_{t=1}^T y_t - \hat{y}_t $
MAPE	Mean Absolute Percentage Error	$\frac{100}{T} \sum_{t=1}^T \left \frac{y_t - \hat{y}_t}{y_t} \right $
SMAPE	Symmetric MAPE	$\frac{100}{T} \sum_{t=1}^T \frac{ y_t - \hat{y}_t }{(y_t + \hat{y}_t)/2}$
MASE	Mean Absolute Scaled Error	$\frac{\frac{1}{T} \sum_{t=1}^T y_t - \hat{y}_t }{\frac{1}{T-1} \sum_{t=2}^T y_t - y_{t-1} }$

specified distributions for evaluation.

Evaluation metrics are essential for assessing performance and guiding improvements. Table 17.1 presents a list of common metrics used for evaluating forecasting models.

Root Mean Squared Error (RMSE), like Mean Squared Error (MSE), penalizes outliers, but is more interpretable, since it is expressed in the same units as the target value. Mean Absolute Error (MAE) treats all errors linearly, so it is less sensitive to outliers compared to MSE or RMSE.

MSE, RMSE, and MAE are scale-dependent metrics. In contrast, Mean Absolute Percentage Error (MAPE), Symmetric MAPE (SMAPE), and Mean Absolute Scaled Error (MASE) are scale-independent, allowing for comparison across datasets with different units. Finally, Mean Absolute Scaled Error (MASE) addresses some of the limitations of MAPE and SMAPE by scaling errors relative to a naive forecast, serving as an additional metric for evaluating forecast accuracy.

Chapter 18: Simulation Studies

18.1 Network Configuration

In this section, we provide an overview of network architecture, training process, hyperparameter tuning, and evaluation metrics for the LSTM network used in our study.

Our design choices are informed by the findings of Hewamalage et al. (2021), which guide the appropriate settings for the LSTM network. The architecture consists of an input layer, followed by one to two LSTM layers, and concludes with a dense layer to balance model complexity and performance.

The network is trained using Backpropagation Through Time (BPTT) (Mozer 2013; Robinson and Fallside 1987; Werbos 1988). Although the open-source Cocob (COntinuous COin Betting) optimizer is reported to perform the best, we use the built-in Adam optimizer for its practical convenience and competitive performance. The learning rate is initially set to 0.001, consistent with recommended ranges for Adam. The batch size and cell dimension are initially set to 32 and 64, respectively, to balance training efficiency with model capacity, forming the foundation of our chosen configuration. In Section 18.3.1.3, we vary these hyperparameters to explore their impact on model performance, but find no improvement. Consequently, we reuse the original configuration for subsequent experiments, including the data application.

Finally, model performance is evaluated using RMSE, MAE, MAPE, SMAPE, and MASE, consistent with the metrics discussed in Chapter 17.

18.2 Experimental Setup

The goals of the simulation studies are threefold: (1) to compare the predictive performance of the LSTM and MTD models, both generally for gamma data and specifically for zero-inflated gamma data, (2) to assess the stability and robustness of their performance, and (3) to investigate the impact of hyperparameters on LSTM performance.

To compare the predictive performance of the LSTM and MTD models under various conditions, we run both models on Gamma Scenario 1–9 (see Table 6.2 of Part I for details) and assess their performance using RMSE as the primary evaluation metric. Each model is trained and tested under identical data splits with a ratio of 0.8 to ensure a fair comparison.

To assess the stability and robustness of model performance, we run both the LSTM and MTD models on 10 independently generated replicates of Gamma Scenario 1 (see Table 6.2 of Part I for details). Each replicate consists of a new synthetic dataset generated using the same underlying parameters but with different random seeds. This setup allows us to quantify the variability in model outcomes arising from randomness in data generation and model training, and to evaluate whether the observed performance differences between the LSTM and MTD models are statistically significant.

To investigate the impact of hyperparameters on LSTM performance, we run the network with a variety of configurations on Gamma Scenario 1 with 10 independently generated

replicates for each configuration. The configurations explore key hyperparameters including the learning rate, the batch size, the number of layers, and the number of hidden units. Specifically, we evaluate the following LSTM configurations:

1. Learning rate: 0.1, 0.01, and 0.001
2. Batch size: 1, 8, 16, 32, 64, and 128
3. Number of layers: 1, 2, and 3
4. Hidden cell dimensions: 32, 64, and 128

This setup allows us to assess the sensitivity of LSTM performance to hyperparameter choices, identify optimal configurations that yield consistent and robust results, and inform the selection of settings for experiments conducted in Chapter 19.

For the zero-inflated Gamma settings, we focus exclusively on Scenario 1 (see Table 13.2 of Part II for details), since each scenario includes six cases defined by all combinations of $P = 0.1, 0.5, 0.7$, and $\epsilon = 0.1, 0.4$, where P represents the zero-inflated probability and ϵ denotes the threshold value. We similarly run both models and evaluate their performance using RMSE, allowing us to specifically examine model behavior on zero-inflated data. Additionally, we compute RMSE **below** (i.e., RMSE for data less than or equal to ϵ) and **above** (i.e., RMSE for data greater than ϵ) to assess predictive accuracy in the lower and upper ranges, respectively. As discussed in Chapter 14, when P is small, a large proportion of observations fall above ϵ , providing more information to estimate the value in the upper range. As P increases, more observations concentrate below ϵ , making the RMSE in the

near-zero range the primary indicator of the overall performance. These additional metrics provide insight into model performance for low and high-value regions, particularly relevant in the context of zero-inflated distributions.

18.3 Results

18.3.1 Prediction for Gamma Scenarios

18.3.1.1 Experiment 1: Model Performance Comparison For Gamma Scenarios

As discussed in Table 6.1 of Part I, Scenarios 1 and 2 follow the original MTD setup: Scenario 1 uses exponentially decreasing weights, which are typically observed in real-world data, and Scenario 2 uses unevenly arranged relevant lags. Scenarios 3 to 9 follow the same weight pattern as Scenario 1. Scenarios 3 to 6 evaluate gamma shape and rate, and Scenarios 7 to 9 consider high-skew cases.

Table 18.1 summarizes the RMSE comparisons between LSTM and MTD based on one-step ahead predicted means for Scenarios 1 through 9. The predicted results from LSTM and MTD are similar. RMSEs for MTD are lower in Scenarios 2, 3, 4, and 6, though the differences are minimal. Conversely, LSTM yields slightly lower RMSEs in Scenarios 7 to 9, though the differences are again minimal. RMSEs are the highest for both models in Scenario 2. Table 18.2 presents the corresponding bias comparisons across the same scenarios. Overall, biases are small, with positive values indicating overestimation and negative values underestimation.

Table 18.1: RMSE Comparison of LSTM and MTD for Gamma Scenarios 1–9 (s1–s9).

.	LSTM	MTD
s1	1.3326	1.3569
s2	2.3001	2.1988
s3	1.0700	1.0446
s4	1.6846	1.5282
s5	1.0215	1.1296
s6	0.8263	0.7649
s7	0.7452	0.7617
s8	0.3675	0.3808
s9	0.1837	0.1902

Table 18.2: Bias Comparison of LSTM and MTD for Gamma Scenarios 1–9 (s1–s9).

.	LSTM	MTD
s1	0.0347	0.0749
s2	0.2533	0.1611
s3	0.1487	0.0614
s4	-0.0691	0.0836
s5	0.0733	0.0684
s6	0.1508	0.0422
s7	0.2311	0.0467
s8	0.0224	0.0233
s9	0.0289	0.0117

Figure 18.1 illustrates these means for Scenario 1 and 2. Figure 18.2 presents a zoomed-in view of the same plot, focusing on a subset of the test data ($n = 200$). As shown in Plot (a), both models predict well, with LSTM performing comparably to MTD. However, as shown in Plot (b), both models appear to struggle more in Scenario 2 compared to their performance in Scenario 1. Additional plots illustrating the predicted means for Scenarios 3 through 9 (Figure F.1, Figure F.2) are provided in the Appendix F Section F.1.

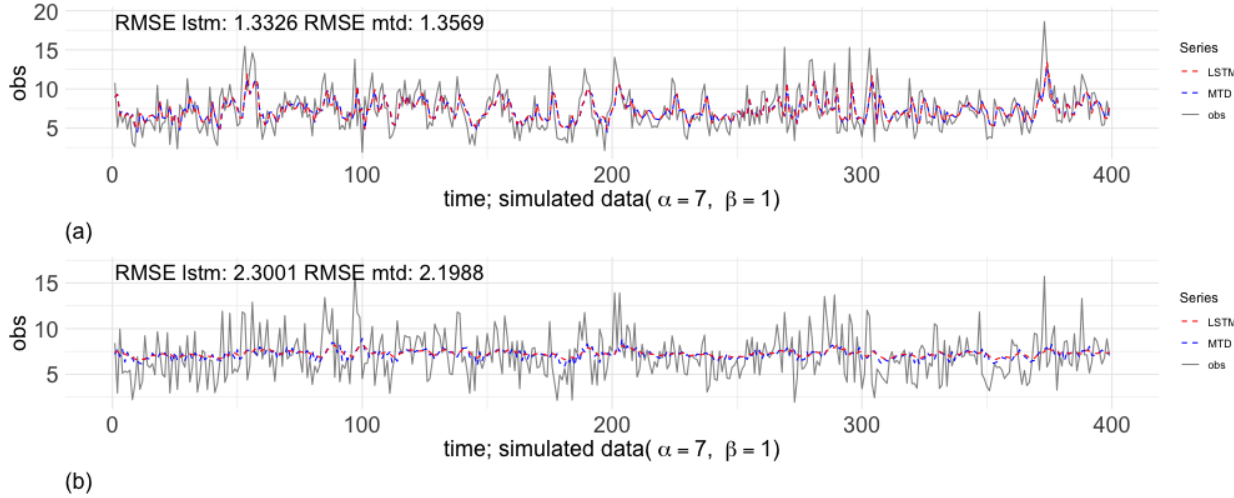


Figure 18.1: One-step-ahead predicted means for (a) Gamma Scenario 1 and (b) Scenario 2: Solid (black) lines are true values. Dashed (red) lines are LSTM predicted means and dashed (blue) lines are MTD predicted means.

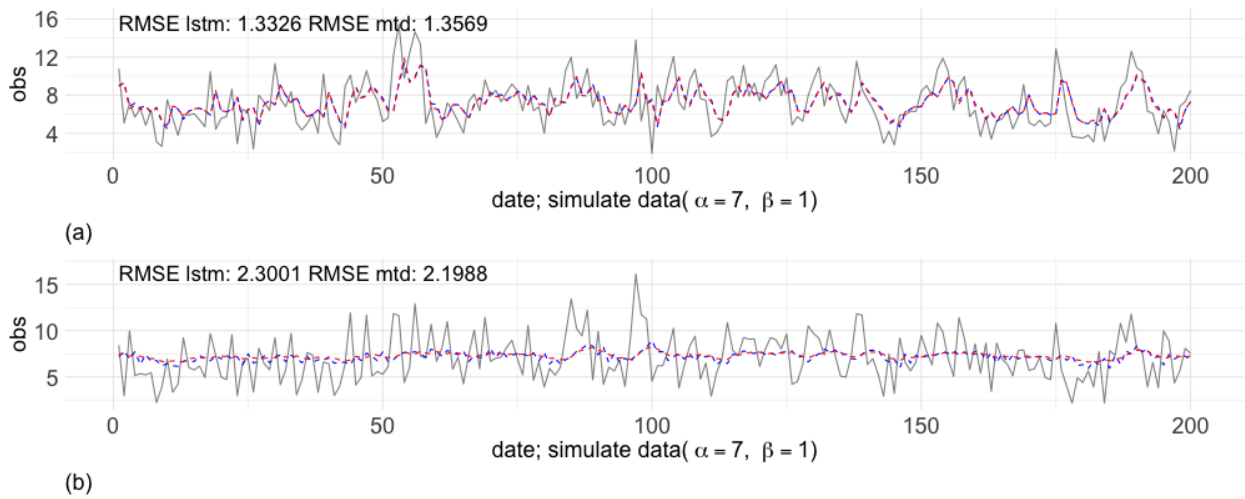


Figure 18.2: Zoomed-in view of one-step ahead predicted means for (a) Gamma Scenario 1 and (b) Scenario 2: Solid (black) lines are true values. Dashed (red) lines are LSTM predicted means and dashed (blue) lines are MTD predicted means.

18.3.1.2 Experiment 2: Stability and Robustness Analysis

Using Scenario 1 with 10 replicates, we conduct additional analyses to evaluate model performance and assess whether the performance differences between LSTM and MTD are significant. Results from the paired t-test indicated a mean difference in RMSE of 0.1290 ($p\text{-value} = 0.005175$, $\text{df} = 9$), with MTD consistently yielding lower RMSEs. Figure 18.3 illustrates these findings.

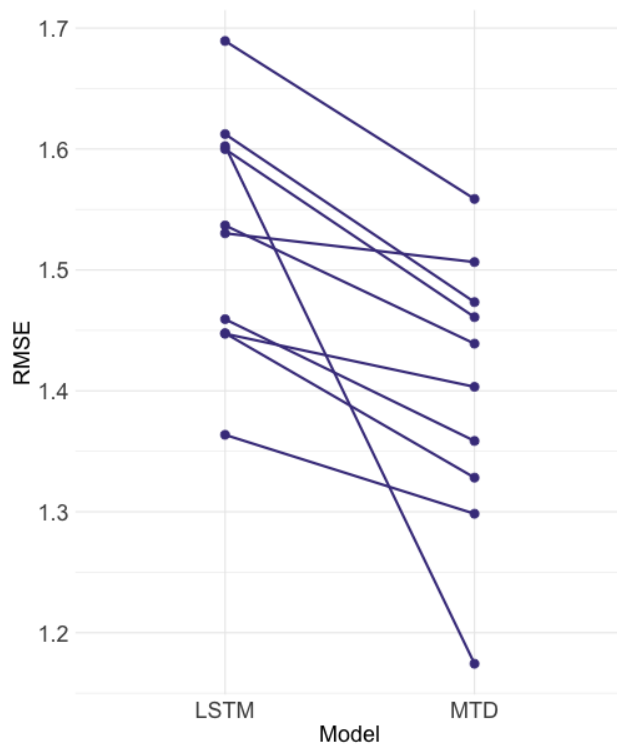


Figure 18.3: Relative Performance of LSTM and MTD models for Gamma Scenario 1 (Mean RMSE for LSTM = 1.5290; Mean RMSE for MTD = 1.4000). Data points are connected by lines to indicate results from the same replicate.

18.3.1.3 Experiment 3: Impact of Hyperparameters on LSTM Performance

Reusing Scenario 1 with 10 replicates, we perform additional analyses to determine whether hyperparameter tuning is necessary. For each hyperparameter, we conduct a repeated-measures ANOVA, treating hyperparameter levels as the treatment factor and replicate ID, representing different simulated data replicates, as the random effect. If the overall p-value is smaller than 0.05, we follow up with the Bonferroni-corrected pairwise comparisons to identify which pairs differ significantly.

Among these configurations, the p-value is statistically significant for batch size ($\text{Pr}(> F) = 4.4e - 06$, $df = 2, 24$), and pairwise comparisons indicate that RMSEs differ significantly only between batch size 64 and all other batch sizes (1, 8, 16, 32, and 128), as well as between batch size 128 and all other batch sizes (1, 8, 16, 32, and 64). The p-value is also significant for cell dimensions ($\text{Pr}(> F) = 0.0113$, $df = 2, 24$); however, pairwise comparisons reveal significant differences in RMSE only between cell dimensions of 32 and 64, as well as between 32 and 128, but not between 64 and 128. Figure 18.4 illustrates these findings.

These results indicate that further hyperparameter tuning yields minimal performance gains. Notably, reducing the batch size slows down model training, although the model still completes within minutes, but does not produce a practical improvement in RMSE. Therefore, we adopt the default configuration for subsequent experiments: learning rate = 0.001, batch size = 32, number of layers = 1, and cell dimension = 64.

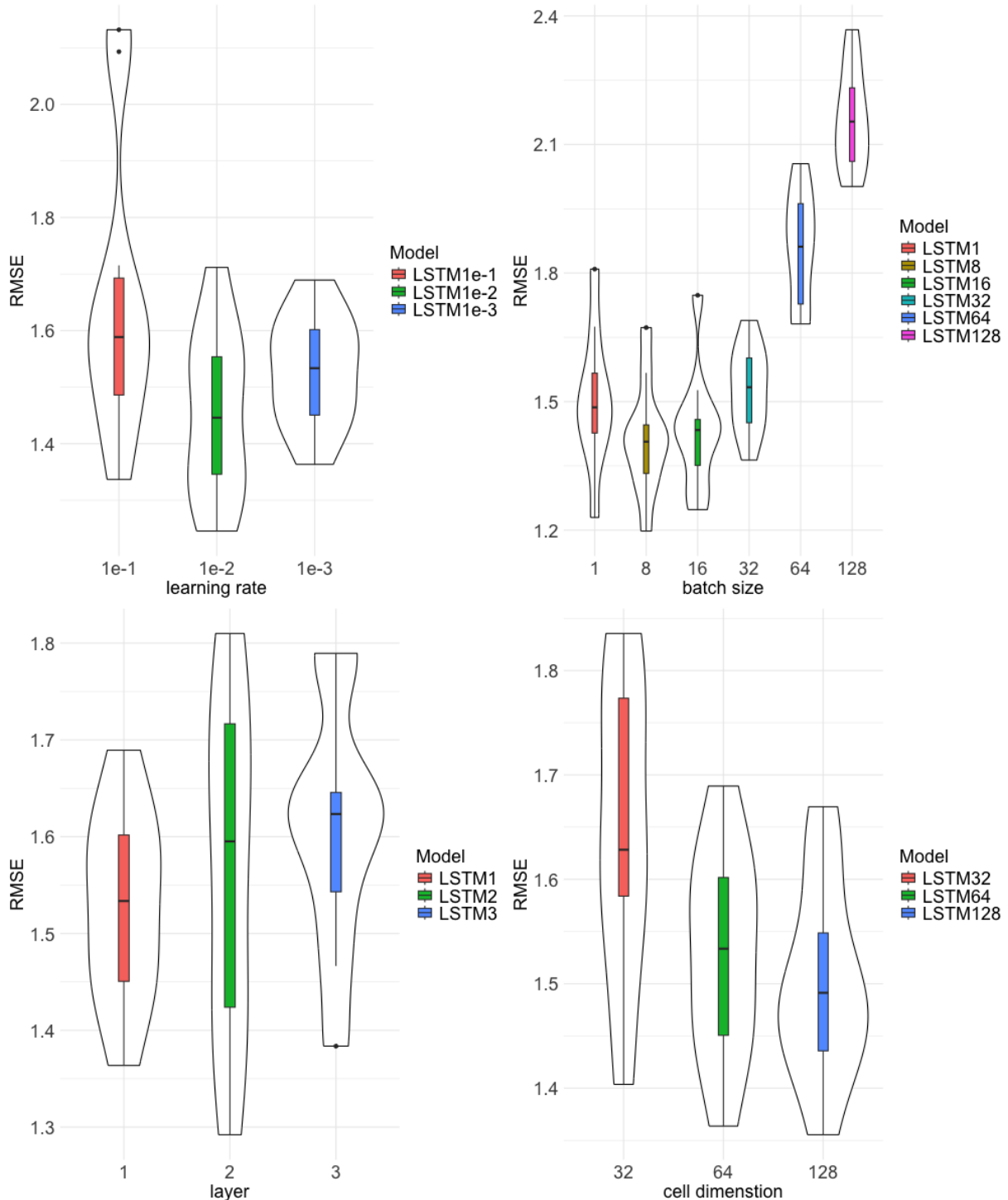


Figure 18.4: Relative performance of LSTM networks with varying learning rates ($0.1, 0.01, 0.001$), batch sizes (1, 8, 16, 32, 64, 128), number of layers (1–3), and cell dimensions (32, 64, 128) for Gamma Scenario 1.

18.3.2 Prediction for Zero-inflated Gamma Scenarios

18.3.2.1 Experiment 4: Model Performance Comparison For Zero-inflated Gamma Scenarios

Table 18.3 summarizes the RMSE comparisons between LSTM and MTD based on one-step ahead predicted means for Scenario 1, with rows correspond to all combinations of $P_i = 0.1, 0.5, 0.7$, and $\epsilon = 0.1, 0.4$, where P is the zero-inflated probability and ϵ is the threshold value. LSTM generally achieves lower overall RMSEs compared to MTD.

However, patterns similar to those in Chapter 14 of Part II reappear. The overall RMSE can obscure important differences in predictive performance. To provide a clearer picture, we decompose the RMSE into **below** (which captures accuracy on values less than or equal to ϵ) and **above** (which reflects predictive accuracy for values exceeding ϵ) in Table 18.4. Specifically, for zero-inflated gamma data with low zero-inflation probability (e.g., $P = 0.1$), the RMSE **above** is a more informative measure of performance. As P increases, this relationship reverses, and the RMSE **below** becomes more relevant. As shown in Table 18.4, when $P = 0.1$, MTD outperforms LSTM in RMSE **above**. This trend persists at higher levels of zero-inflation (e.g., $P = 0.5, 0.7$), where MTD again yields lower values for RMSE **below** than LSTM. Table 18.5 presents the corresponding bias comparisons across the same scenario. Similar pattern emerges.

Figure 18.5 illustrates these patterns for Scenario 1. Figure 18.6 presents a zoomed-in view of the same plot, focusing on a subset of the test data ($n = 200$). Results for Scenario

Table 18.3: RMSE Comparison of LSTM and MTD for ZIGamma Scenarios 1. Each row label indicates the combination of P (zero-inflated probability) and ϵ (threshold value) used in the simulation.

.	LSTM	MTD
P01Eps01	1.7221	1.7302
P01Eps04	2.0843	2.6386
P05Eps01	2.1102	2.8361
P05Eps04	2.1788	2.1922
P07Eps01	2.2762	3.0739
P07Eps04	2.0916	2.5798

Table 18.4: RMSE Comparison of LSTM and MTD for ZIGamma Scenarios 1 Above and Below. Each row label indicates the combination of P (zero-inflated probability) and ϵ (threshold value) used in the simulation. Reported values show decomposed RMSE below and above the threshold.

.	LSTM Below	MTD Below	LSTM Above	MTD Above
P01Eps01	3.6285	4.2964	1.4910	1.3668
P01Eps04	3.2122	5.9082	1.8826	1.7945
P05Eps01	2.0551	0.7752	2.1655	3.9641
P05Eps04	2.0495	1.6675	2.3426	2.7477
P07Eps01	1.2984	0.3677	3.5798	5.4580
P07Eps04	1.2583	0.5346	3.3044	4.6465

2 (Table F.1, Table F.2, Table F.3, Table F.4, Figure F.3, Figure F.4) are provided in Appendix F Section F.2 and are similar to those in Scenario 1.

Table 18.5: Bias Comparison of LSTM and MTD for ZIGamma Scenarios 1. Each row label indicates the combination of P (zero-inflated probability) and ϵ (threshold value) used in the simulation.

.	LSTM	MTD
P01Eps01	-0.0958	0.1713
P01Eps04	-0.4361	1.2466
P05Eps01	0.1945	-1.5305
P05Eps04	0.3950	-0.1121
P07Eps01	-0.1006	-1.4796
P07Eps04	0.0023	-0.9728

Table 18.6: Bias Comparison of LSTM and MTD for ZIGamma Scenarios 1 Above and Below. Each row label indicates the combination of P (zero-inflated probability) and ϵ (threshold value) used in the simulation. Reported values show overall RMSE, with decomposed RMSE below and above the threshold.

.	LSTM Below	MTD Below	LSTM Above	MTD Above
P01Eps01	3.6105	4.2598	-0.3655	-0.1262
P01Eps04	3.1820	5.8832	-0.9206	0.6257
P05Eps01	2.0234	0.6896	-1.6904	-3.8186
P05Eps04	2.0416	1.5973	-1.8362	-2.4284
P07Eps01	1.2785	0.2471	-3.1124	-5.2506
P07Eps04	1.2235	0.4784	-2.8609	-4.3752

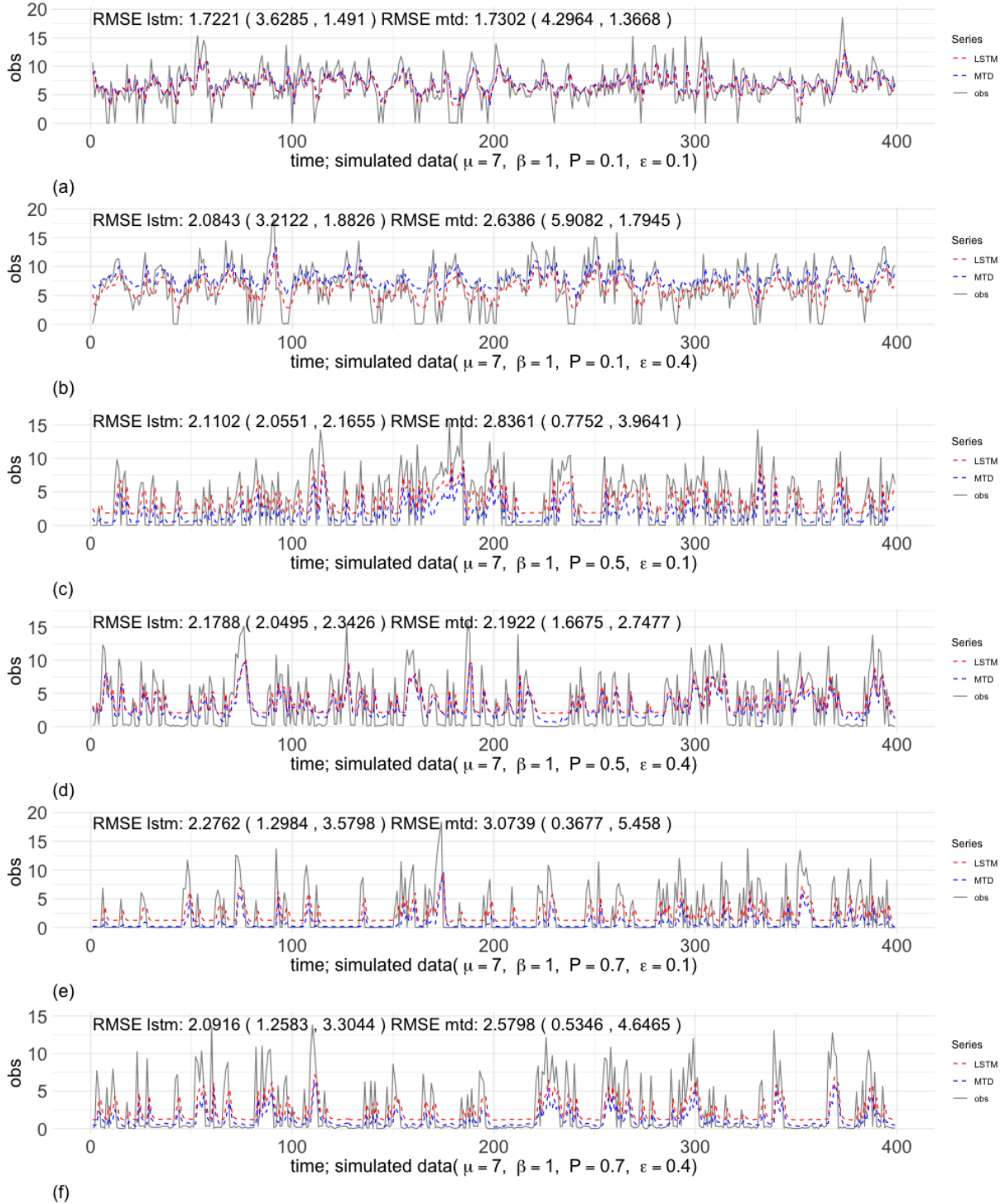


Figure 18.5: One-step ahead predicted means for ZIGamma Scenario 1: Solid (black) lines are true values. Dashed (red) lines are LSTM predicted means and dashed (blue) lines are MTD predicted means. Reported values show overall RMSE, with decomposed RMSE below and above the threshold shown in parentheses: RMSE (RMSE for data $\leq \epsilon$, RMSE for data $> \epsilon$).

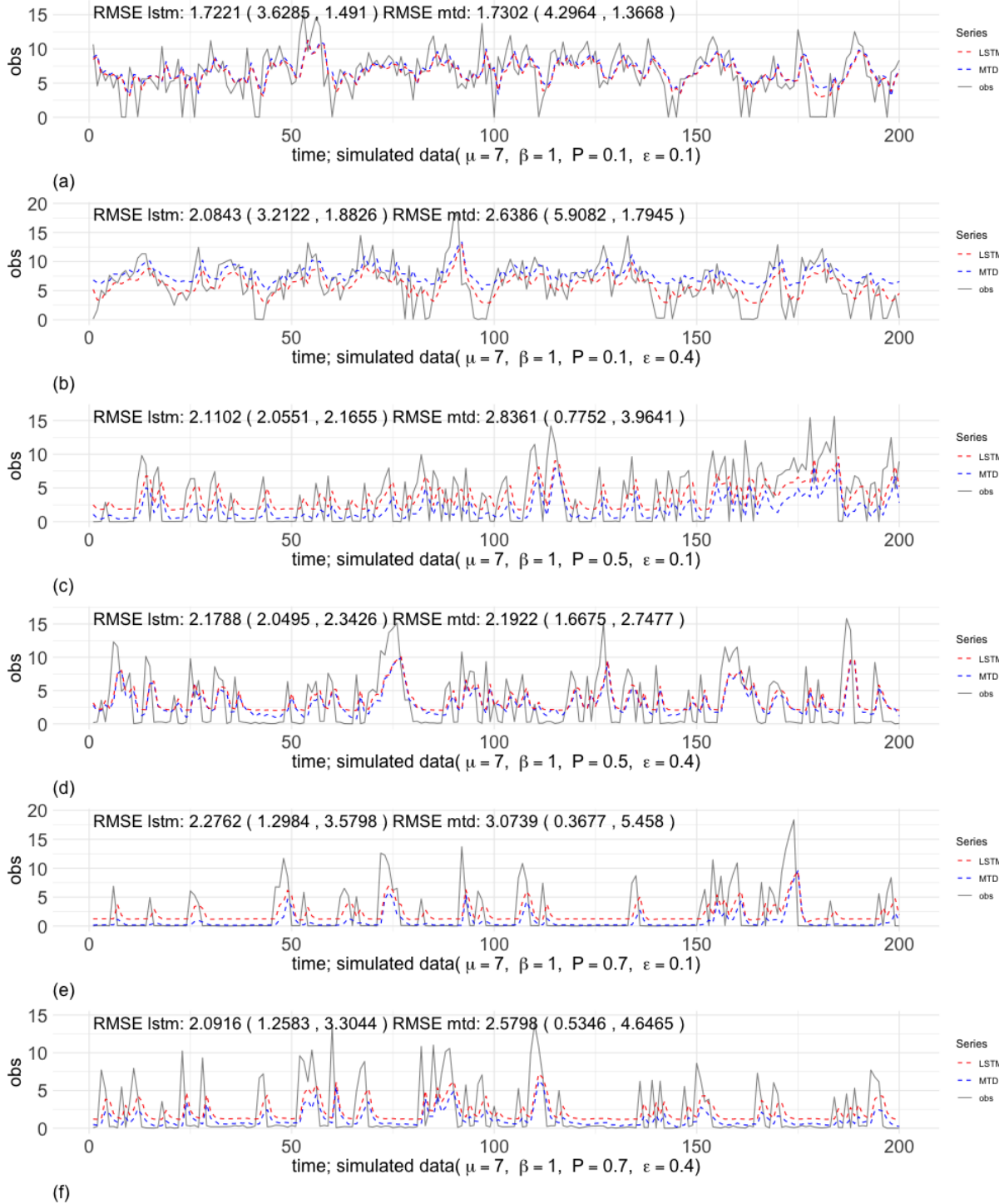


Figure 18.6: Zoomed-in view of one-step ahead predicted means for ZIGamma Scenario 1: Solid (black) lines are true values. Dashed (red) lines are LSTM predicted means and dashed (blue) lines are MTD predicted means. Reported values show overall RMSE, with decomposed RMSE below and above the threshold shown in parentheses: RMSE (RMSE for data $\leq \epsilon$, RMSE for data $> \epsilon$).

Chapter 19: Data Applications: NASA MERRA-2 Wind Speeds Data

19.1 Experimental Setup

19.1.1 Data Access and Description

Wind speed is a key proxy variable in energy forecasting, and accurate prediction of wind speed is crucial for reliable power generation. The MERRA-2 wind speed data were accessed and downloaded from the NASA GES DISC Earthdata API ([Global Modeling and Assimilation Office \(GMAO\) 2015](#)) via Python. Wind speed components at multiple heights (50 m, 10 m, 2 m) for the Limon Wind Energy Center, the largest wind farm in Colorado, were extracted and interpolated using an adapted R script ([Mosshammer 2016; Baumgartner and Schmidt 2016](#)). Figure 19.1 shows the time series of hourly wind speeds (m/s) at these heights during 2024.

The datasets used for the experiments are:

1. wind speeds (m/s) at heights of 50 m above ground level
2. wind speeds (m/s) at heights of 10 m above ground level
3. wind speeds (m/s) at heights of 2 m above ground level

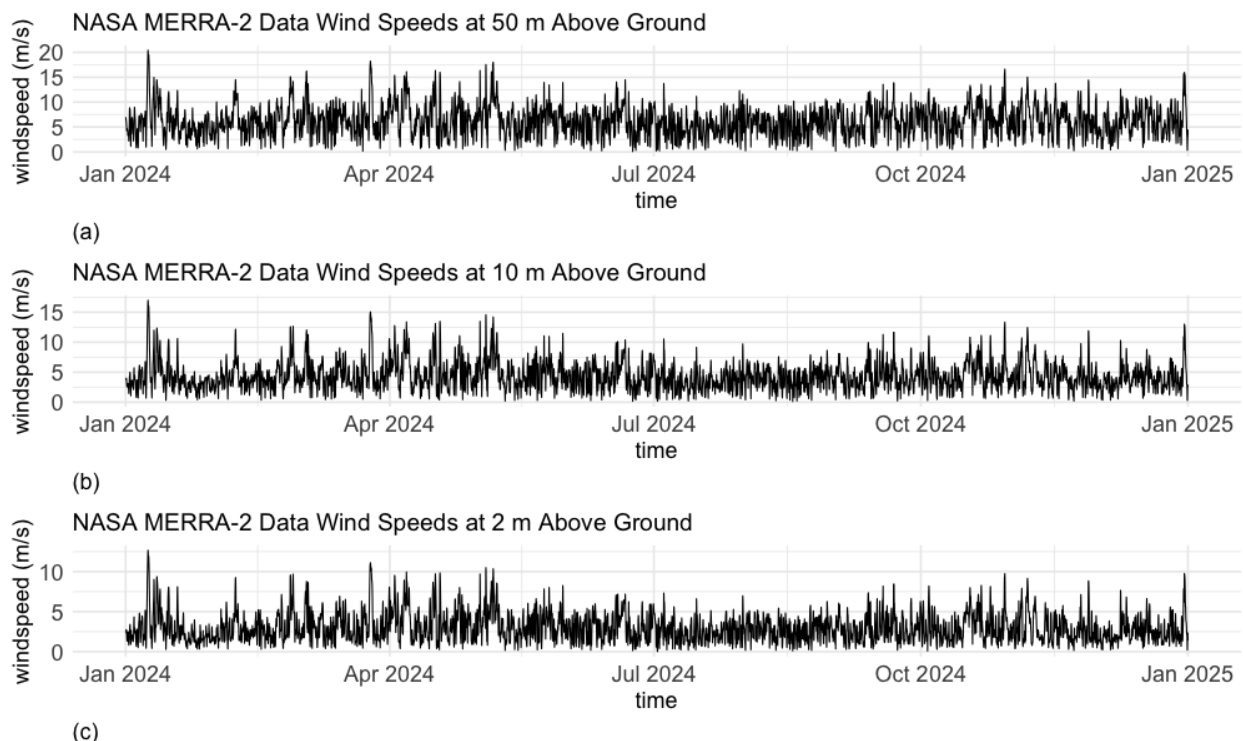


Figure 19.1: Time series plot of observed hourly wind speeds (m/s) at heights of (a) 50 m, (b) 10 m, and (c) 2 m above ground level at the Limon Wind Energy Center, Colorado, for the year 2024. Data sourced from MERRA-2 via the NASA GES DISC Earthdata API.

19.1.2 Model Configuration and Implementation

For MTD, the hyperparameter settings are detailed in Chapter 5. MTD is implemented in R and executed on a high-performance computing (HPC) cluster. Training is performed following the procedure described in Algorithm 1 (Figure 5.1). For MTD, one-step-ahead prediction is performed using the preceding observed values to forecast each test observation, with the predictive distribution obtained by averaging over all posterior MCMC samples.

For LSTM, we reuse the default configuration for subsequent experiments: learning rate = 0.001, batch size = 32, number of layers = 1, and cell dimension = 64. LSTM is implemented in PyTorch and trained on a standard workstation.

During training, each iteration of the LSTM loop involves:

1. Perform a forward pass to obtain predictions.
2. Calculate the loss between predictions and targets.
3. Compute gradients of the loss with respect to network parameters via backpropagation.
4. Update the parameters using the Adam optimizer.
5. Return the training loss.

For LSTM, one-step-ahead prediction is performed by feeding the model the sequence of past observed values at each test time point, generating the predicted value, and repeating the process across the entire test set.

Table 19.1: Comparison of LSTM and MTD for predicting wind speeds (m/s) at 50 m above ground level.

.	LSTM	MTD
RMSE	0.6359	0.3508
MAE	0.6021	0.2692
MAPE	11.1103	4.2550
SMAPE	9.9305	4.2051
MASE	0.6595	0.3660

19.2 Results

19.2.1 Prediction Results

In the initial configuration, the LSTM network are trained using an L2 loss function and evaluated against the MTD model using RMSE. For MAE evaluation, a separate LSTM is trained with an L1 loss function. In contrast, MTD does not rely on training with an explicit loss function.

To facilitate a more rigorous and independent comparison, we incorporate additional error metrics, namely MAPE, SMAPE, and MASE to evaluate and compare the performance of the LSTM and MTD models. All LSTM models are trained using an L2 loss function, except for the one evaluated with MAE, which is trained using an L1 loss function.

As shown in Tables (Table 19.1, Table 19.2, Table 19.3), MTD consistently outperforms the LSTM models across all evaluated metrics and training configurations for wind speeds at 50 m, 10 m, and 2 m above ground level. Since all reported MASE values are less than 1, this indicates that both models outperform the naïve forecasting benchmark on average.

Table 19.2: Comparison of LSTM and MTD for predicting wind speeds (m/s) at 10 m above ground level.

.	LSTM	MTD
RMSE	0.4607	0.2376
MAE	0.3692	0.1614
MAPE	11.2891	4.0688
SMAPE	10.2499	3.9569
MASE	0.6194	0.2873

Table 19.3: Comparison of LSTM and MTD for predicting wind speeds (m/s) at 2 m above ground level.

.	LSTM	MTD
RMSE	0.4011	0.2215
MAE	0.2696	0.1543
MAPE	11.6386	6.5935
SMAPE	12.6050	6.2548
MASE	0.6660	0.3537

To strengthen the comparison, we conduct an additional experiment by increasing the LSTM input window size, W , and the MTD order, L , from 5 to 15 (i.e., longer look-back steps). We then re-evaluate these models using RMSE, MAE, MAPE, and SMAPE.

As shown in Tables (Table 19.4, Table 19.5, Table 19.6), the performance of the LSTM network shows slight improvement with a larger window size, though the gains are minimal. In contrast, the MTD model shows no performance gain, but still consistently outperform the LSTM across all metrics.

Given that batch size appears to be an important hyperparameter for LSTM, we further test values of 8, 16, 64, 128, and 256, compared to the baseline of 32. Nevertheless, none of these settings yield better performance than the MTD model. Corresponding training and

Table 19.4: Comparison of LSTM and MTD with 5 vs. 15 look-back steps for predicting wind speeds (m/s) at 50 m above ground level. W denotes the LSTM input window size and L denotes the MTD order; both represent look-back steps.

.	LSTM ($W = 5$)	MTD ($L = 5$)	LSTM ($W = 15$)	MTD ($L = 15$)
RMSE	0.6359	0.3508	0.6185	0.3568
MAE	0.6021	0.2692	0.5923	0.2753
MAPE	11.1103	4.2550	10.4424	4.3487
SMAPE	9.9305	4.2051	9.9404	4.3002
MASE	0.6595	0.3660	0.6618	0.3743

Table 19.5: Comparison of LSTM and MTD with 5 vs. 15 look-back steps for predicting wind speeds (m/s) at 10 m above ground level. W denotes the LSTM input window size and L denotes the MTD order; both represent look-back steps.

.	LSTM ($W = 5$)	MTD ($L = 5$)	LSTM ($W = 15$)	MTD ($L = 15$)
RMSE	0.4607	0.2376	0.4740	0.2407
MAE	0.3692	0.1614	0.3849	0.1644
MAPE	11.2891	4.0688	10.3323	4.1250
SMAPE	10.2499	3.9569	10.0114	4.0145
MASE	0.6194	0.2873	0.6269	0.2927

Table 19.6: Comparison of LSTM and MTD with 5 vs. 15 look-back steps for predicting wind speeds (m/s) at 2 m above ground level. W denotes the LSTM input window size and L denotes the MTD order; both represent look-back steps.

.	LSTM ($W = 5$)	MTD ($L = 5$)	LSTM ($W = 15$)	MTD ($L = 15$)
RMSE	0.4011	0.2215	0.3873	0.2240
MAE	0.2696	0.1543	0.2714	0.1562
MAPE	11.6386	6.5935	13.2704	6.6896
SMAPE	12.6050	6.2548	12.8026	6.3384
MASE	0.6660	0.3537	0.6536	0.3582

validation loss plots are provided in the Section F.3.

Figure 19.2 illustrates the one-step-ahead predicted mean wind speeds (in m/s) between LSTM and MTD models at heights of 50 m, 10 m, and 2 m above ground level. Figure 19.3 presents a zoomed-in view of the same plot, focusing on a subset of the test data ($n = 200$). Prediction error plots (Figure 19.4, Figure 19.5) are also provided to highlight the differences between model predictions and actual values.

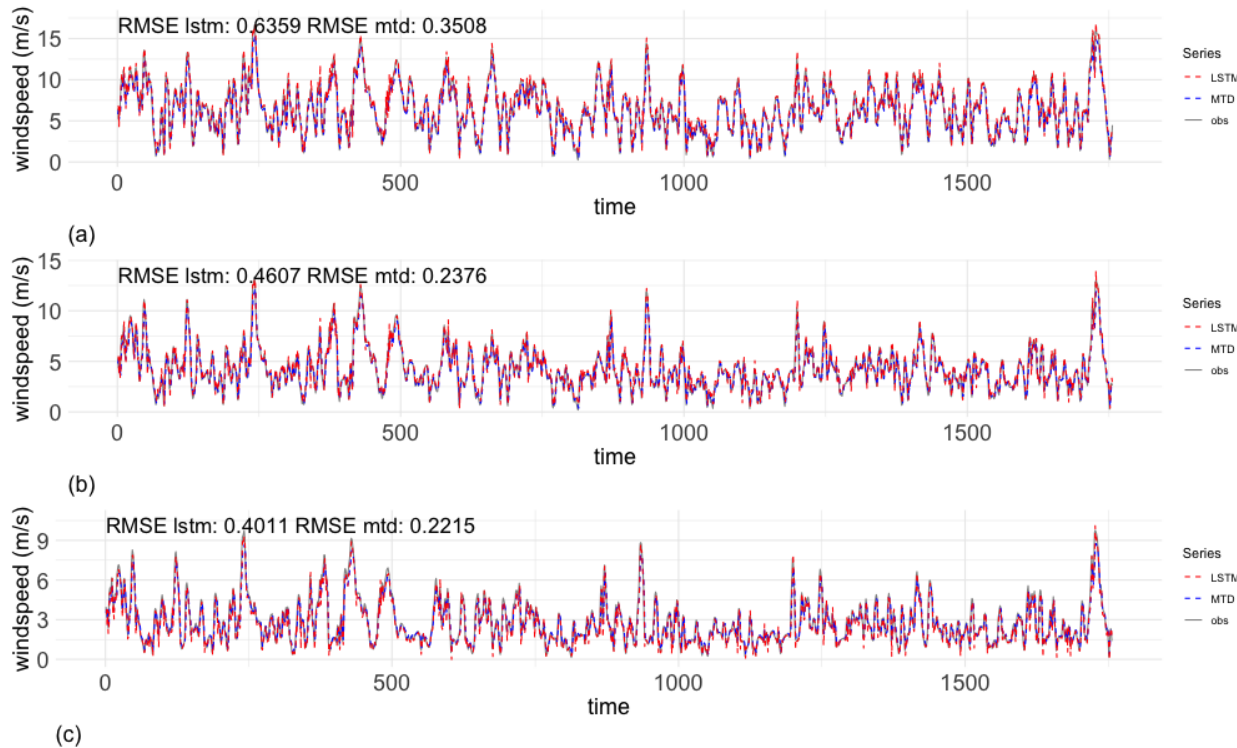


Figure 19.2: One-step ahead predicted means for wind speeds (m/s) at heights of (a) 50 m, (b) 10 m, and (c) 2 m above ground level: Solid (black) lines are true values. Dashed (red) lines are LSTM predicted means and dashed (blue) lines are MTD predicted means.

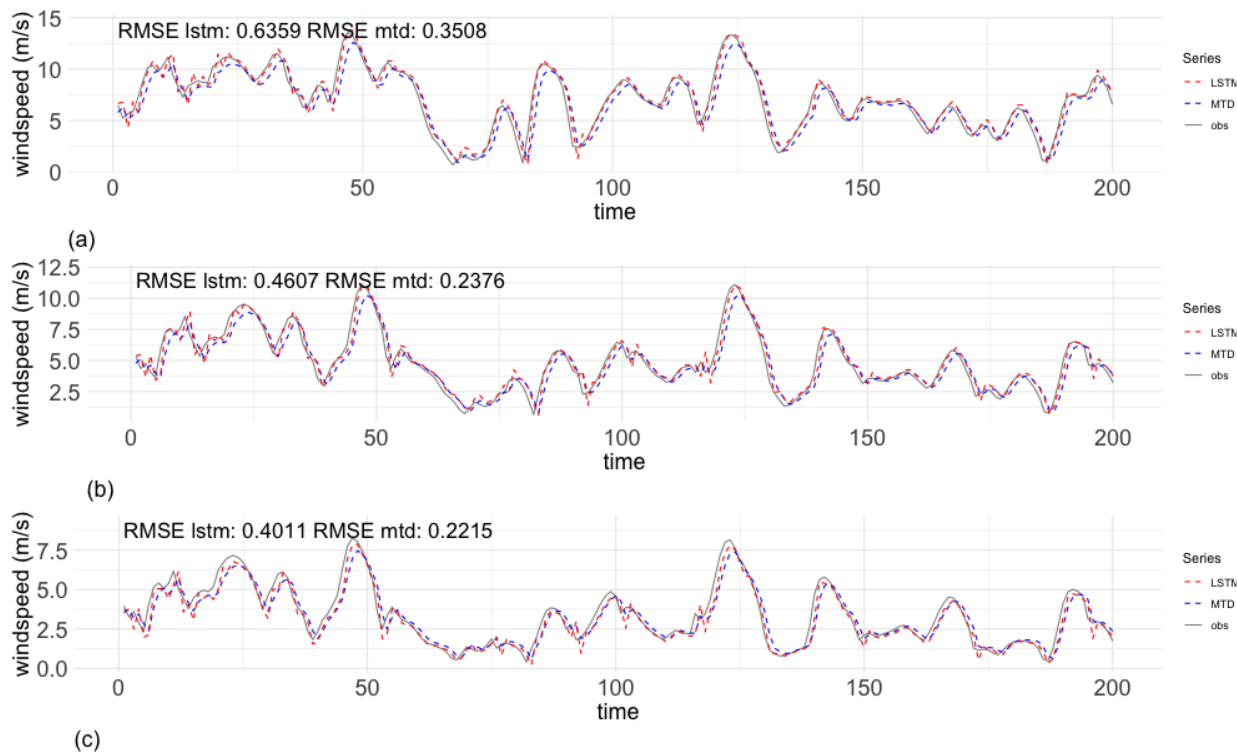


Figure 19.3: Zoomed-in view of one-step ahead predicted means for wind speeds (m/s) at (a) 50 m, (b) 10 m, and (c) 2 m above ground level for $n = 200$. Solid (black) lines represent true values. Dashed (red) lines are LSTM predictions; dashed (blue) lines are MTD predictions.

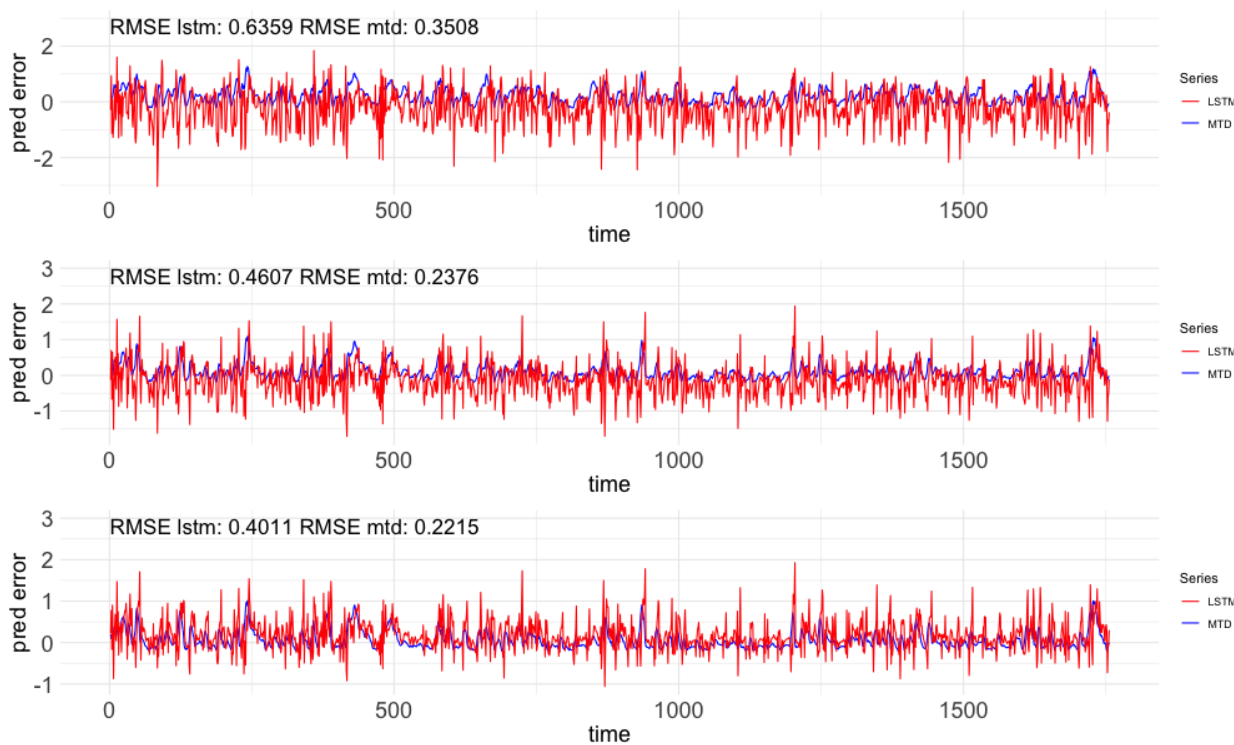


Figure 19.4: One-step ahead prediction errors for wind speeds (m/s) at heights of (a) 50 m, (b) 10 m, and (c) 2 m above ground level: Dashed (red) lines show differences between LSTM predicted means and observed values and dashed (blue) lines show differences between MTD predicted means and observed values.

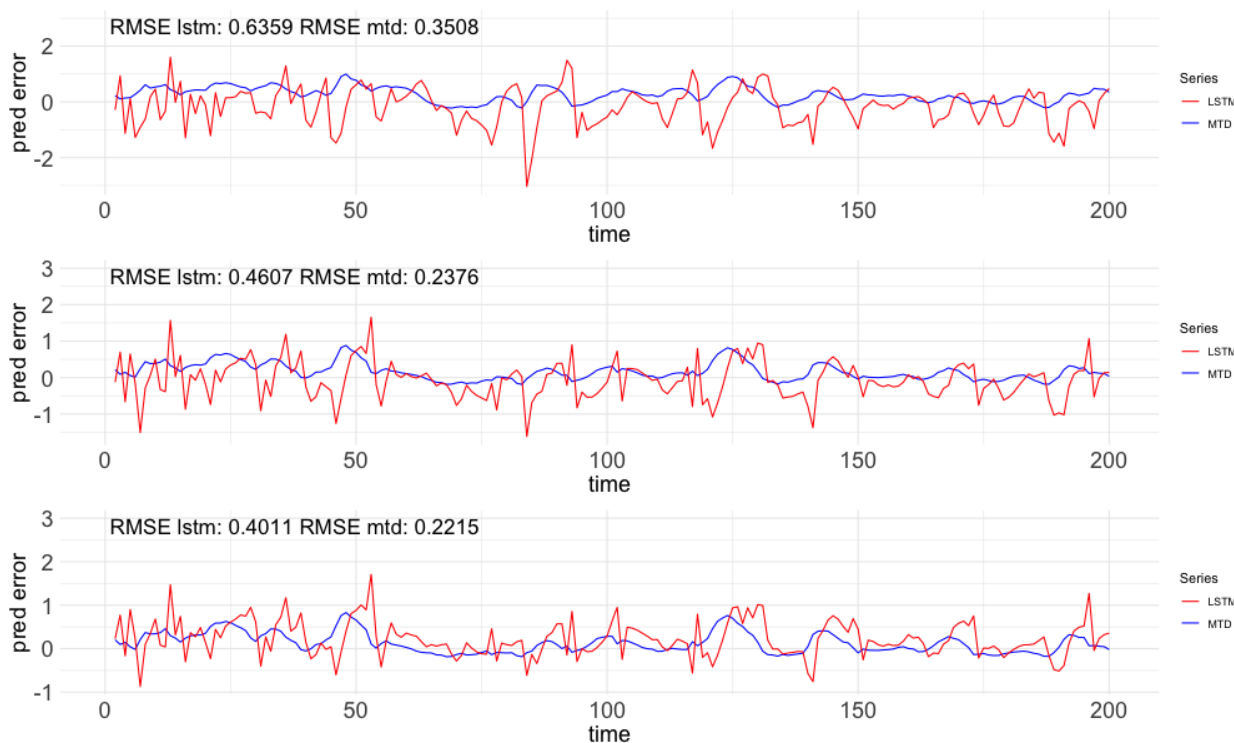


Figure 19.5: Zoomed-in view of one-step ahead prediction errors for wind speeds (m/s) at heights of (a) 50 m, (b) 10 m, and (c) 2 m above ground level: Dashed (red) lines show differences between LSTM predicted means and observed values and dashed (blue) lines show differences between MTD predicted means and observed values.

Table 19.7: Empirical coverage of the 95% predictive intervals for wind speeds (m/s), with look-back steps $L = 5$ vs 15.

.	$L = 5$	$L = 15$
windspeed50mms	0.9522	0.9510
windspeed10mms	0.9562	0.9561
windspeed2mms	0.9567	0.9561

19.2.2 Empirical Coverage of the MTD Model

Empirical coverage is particularly relevant for probabilistic forecasting methods such as MTD, where uncertainty estimation is an integral part of the model output. Therefore, in addition to standard evaluation metrics, MTD is also assessed using this technique to evaluate the reliability of its predictive intervals.

Table 19.7 summarises the 95% one-step ahead posterior predictive intervals for wind speeds (m/s) at heights of 50 m, 10 m, and 2 m above ground level. As shown in the table, the model appropriately captures the predictive uncertainty across wind speeds at all heights. Figure 19.6 and Figure 19.7 illustrate these intervals.

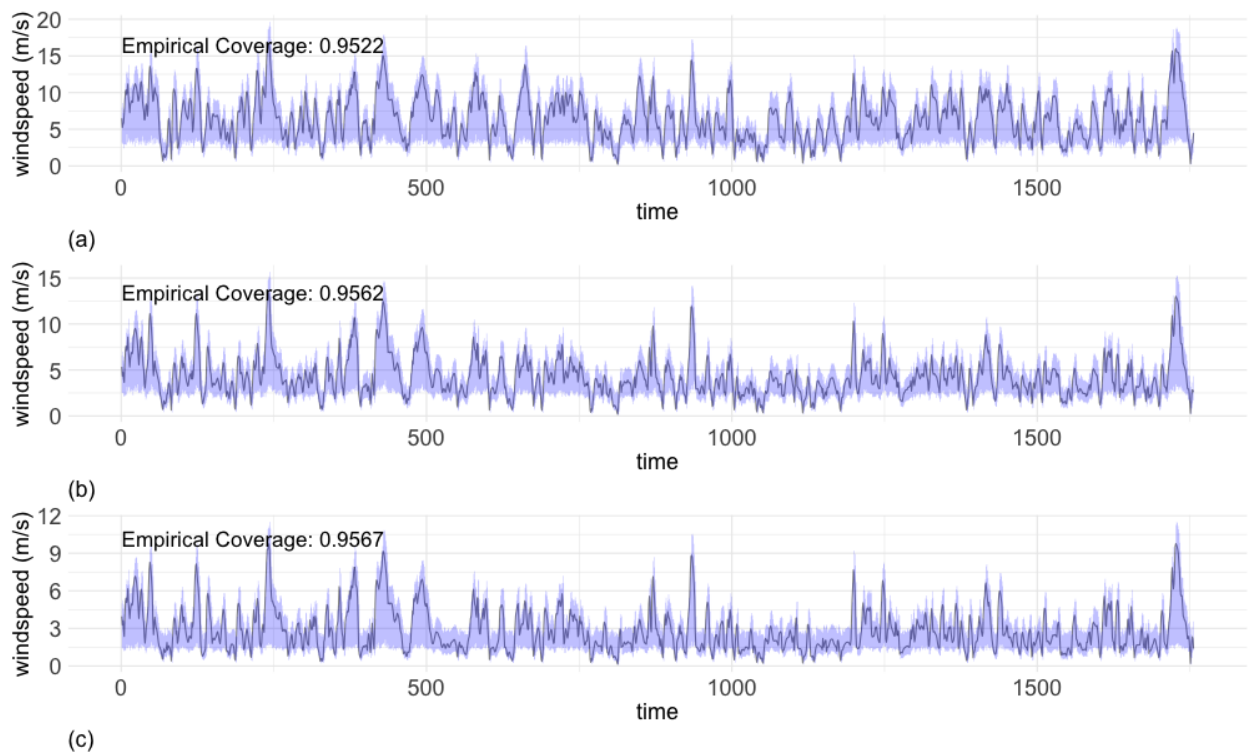


Figure 19.6: 95% one-step ahead posterior predictive intervals for wind speeds (m/s) at heights of (a) 50 m, (b) 10 m, and (c) 2 m above ground level for look-back steps $L = 5$.

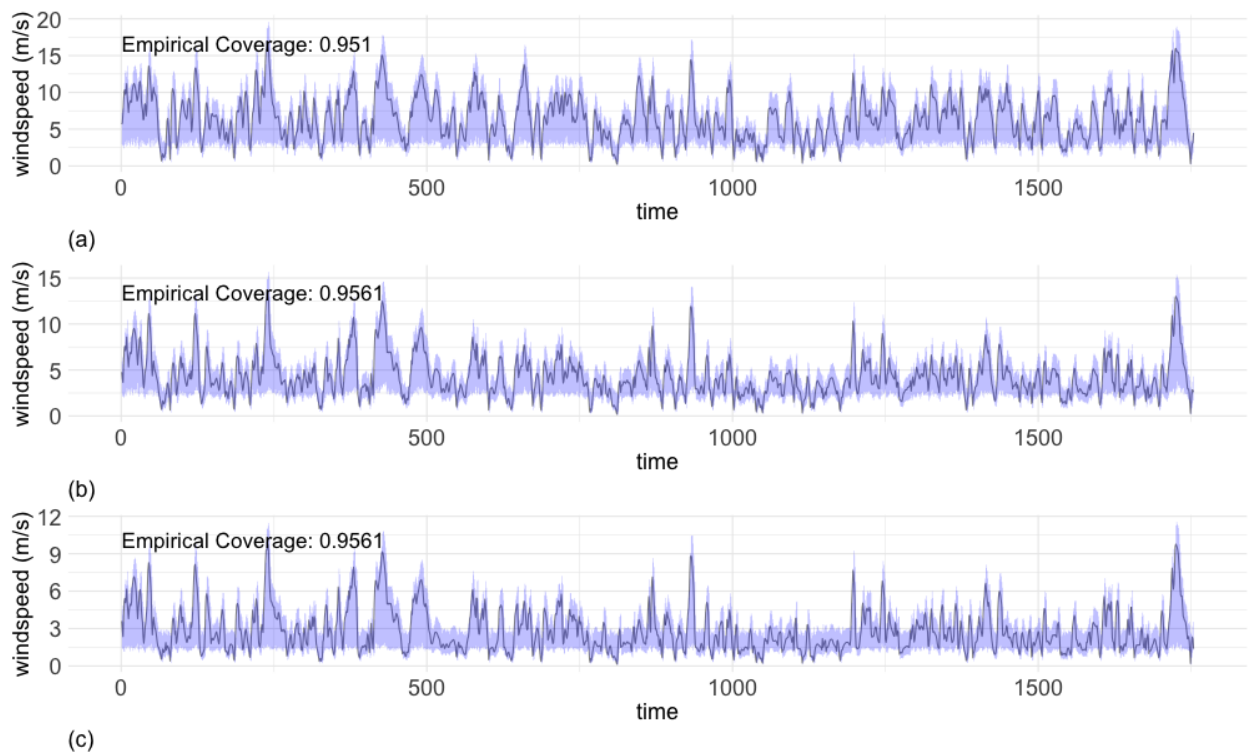


Figure 19.7: 95% one-step ahead posterior predictive intervals for wind speeds (m/s) at heights of (a) 50 m, (b) 10 m, and (c) 2 m above ground level for look-back steps $L = 15$.

Chapter 20: Discussion

In this part of the dissertation, we review LSTMs and evaluate their performance relative to our proposed MTD models. Through simulation studies, we compare both the Gamma MTD and ZIGamma MTD models against the LSTMs. For gamma time series, Gamma MTD and LSTM perform comparably, although further assessment using 10 replicates of Scenario 1 shows that MTD consistently outperforms LSTM. For zero-inflated gamma time series, ZIGamma MTD also outperforms the LSTM, which is expected given the challenges of modeling zero-inflated data, and LSTMs are less specialized for handling this type of data.

In real-world data applications, we focus on comparing the Gamma MTD with LSTMs to assess their practical performance. In this case, Gamma MTD consistently outperforms the LSTM across all evaluation metrics for all three datasets, including wind speed measurements (m/s) at heights of 50 m, 10 m, and 2 m above ground level.

Although the MTD framework can, in principle, be extended to handle non-stationary time series and incorporate predictors incorporating additional model elements into the conditional mean structure ([Zheng et al. 2022](#)), these extensions have not yet been implemented. In addition, it is currently limited to a univariate setting. Consequently, it cannot effectively model non-stationary data, simultaneously capture the effects of past observations and relevant predictors, or account for multivariate dependence. Future research directions

include extending the model to handle non-stationary features, account for variability in wind speed due to factors such as air density, and incorporate the dependence of wind speed across different heights.

Probabilistic models like MTDs offer greater robustness and interpretability due to their probabilistic nature, allowing uncertainty quantification and insights into temporal dependence. Their robustness stem from their ability to capture complex patterns without overfitting, while their structure provides interpretable parameters. However, models such as Gamma MTD and ZIGamma MTD require careful design and specification. In contrast, deep learning networks such as LSTMs are more general-purpose and enable faster computation, though their black-box structure limits interpretability. Therefore, MTD is better suited for explainable and robust modeling, whereas LSTMs are advantageous for large-scale or computationally intensive tasks.

With the growing adoption of transformer architectures, which leverage multi-head attention to model dependence in parallel, future research in sequence modeling should extend these comparisons to include transformer-based models. It is equally important that such comparisons are grounded in appropriate benchmarks and evaluated with suitable metrics to ensure fair and valid conclusions regarding model performance.

Building on the perspectives outlined by Wikle and Zammit-Mangion (2023), who reviewed traditional statistical and modern machine learning approaches for spatial and spatio-temporal data and highlighted the development of hybrid models for latent processes, data, and parameter specifications, a promising avenue for future research is the exploration of hybrid

modeling strategies for time series data. Integrating classical probabilistic models with AI-driven architectures could combine the robustness and interpretability of probabilistic approaches with the flexibility and efficiency of neural networks, providing a rich framework for modeling complex features such as skewness, zero-inflation, and temporal dependence.

Part IV

Conclusion

Chapter 21: Conclusion

In this dissertation, we develop a novel copula-based MTD model that separates the dependence structure from the marginal distribution. This separation enables a choice of copula families that effectively capture dependence and allows the marginal distribution to take any continuous form, providing flexibility in model specification. While we illustrate the approach using the Gamma MTD model, the framework can accommodate a wide range of continuous marginals, such as the lognormal and beta distributions.

Extending this approach, we also propose a copula-based zero-inflated MTD model, which preserves the advantages of copula modeling for capturing dependence while allowing flexible choices of marginal distributions in zero-inflated continuous settings. This extension again demonstrates the framework's generalizability to alternative marginals beyond the gamma distribution. Although we present the the Zero-Inflated Gamma MTD (ZIGamma MTD) model as an example, the same strategy can be applied to construct zero-inflated models with other alternative continuous marginals.

Both the Gamma MTD and ZIGamma models developed in this dissertation utilize a Gaussian copula to capture dependence, though alternative copula families, such as Clayton and Gumbel, can also be employed to better model tail dependence and asymmetry. Future work should explore alternative copula families and assess their impact on model performance.

Furthermore, although the current framework assumes stationarity and does not incorporate predictors, it can be readily extended to non-stationary time series and covariate-dependent models by introducing extra model terms to the conditional mean structure, further enhancing flexibility and realism in modeling complex temporal patterns.

Through simulation studies and real-world applications, we illustrate how MTD and LSTM serve as complementary approaches for modeling complex, skewed, and zero-inflated time series. For gamma time series across various scenarios, Gamma MTD and LSTM perform comparably; however, using 10 replicates of Scenario 1, which features exponentially decreasing weights and a vector of compatible dependence parameters, Gamma MTD outperforms LSTM consistently. For zero-inflated gamma time series, ZIGamma MTD outperforms LSTM consistently, highlighting the advantage of specialized models for handling zero-inflated data.

In real-world datasets, including hourly wind speed measurements at three different heights, Gamma MTD consistently outperforms LSTM, underscoring the robustness and interpretability of probabilistic models. While LSTMs offer general-purpose modeling, computational efficiency, and simpler model design, their black-box nature can limit interpretability and, in some cases, reduce accuracy. In contrast, MTD models provide more robust and explainable temporal modeling but come at the cost of increased computational complexity and more involved model design.

Overall, the proposed copula-based MTD framework provides a flexible, robust, and interpretable approach for modeling complex skewed and zero-inflated time series, demonstrating superior performance compared to LSTM in the settings considered.

Given the growing prominence of transformer architectures in sequence modeling, future research should extend performance comparisons to include transformer-based models. It is equally important to ensure that evaluations are conducted using appropriate benchmarks and metrics. Finally, future work could explore integrated approaches that combine probabilistic models with neural architectures, aiming to leverage the strengths of both frameworks for more accurate, interpretable, and scalable time series modeling.

Part V

Bibliography

Bibliography

- Abraham, Zubin, and Pang-Ning Tan. 2009. “A Semi-Supervised Framework for Simultaneous Classification and Regression of Zero-Inflated Time Series Data with Application to Precipitation Prediction.” *2009 IEEE International Conference on Data Mining Workshops*, 644–49.
- Ahmed, Sabeen, Ian E Nielsen, Aakash Tripathi, Shamoon Siddiqui, Ravi P Ramachandran, and Ghulam Rasool. 2023. “Transformers in Time-Series Analysis: A Tutorial.” *Circuits, Systems, and Signal Processing* 42 (12): 7433–66.
- Alqawba, Mohammed, and Norou Diawara. 2021. “Copula-Based Markov Zero-Inflated Count Time Series Models with Application.” *Journal of Applied Statistics* 48 (5): 786–803.
- Alqawba, Mohammed, Norou Diawara, and N Rao Chaganty. 2019. “Zero-Inflated Count Time Series Models Using Gaussian Copula.” *Sequential Analysis* 38 (3): 342–57.
- Al-Wahsh, H, and A Hussein. 2019. “Estimation of Zero-Inflated Parameter-Driven Models via Data Cloning.” *Journal of Statistical Computation and Simulation* 89 (6): 951–65.

Ansari, Abdul Fatir, Lorenzo Stella, Caner Turkmen, et al. 2024. *Chronos: Learning the Language of Time Series*. <https://arxiv.org/abs/2403.07815>.

Bahdanau, Dzmitry, Kyunghyun Cho, and Yoshua Bengio. 2014. “Neural Machine Translation by Jointly Learning to Align and Translate.” *arXiv Preprint arXiv:1409.0473*.

Bartolucci, Francesco, and Alessio Farcomeni. 2010. “A Note on the Mixture Transition Distribution and Hidden Markov Models.” *Journal of Time Series Analysis* 31 (2): 132–38.

Baumgartner, Johann, and Johannes Schmidt. 2016. *Modellierung Der Aggregierten Leistungsabgabe von Windparks Im Vergleich Zu Gemessenen Leistungswerten Anhand Zwei er Beispielstandorte in Österreich Und Neuseeland*. University of Natural Resources; Life Sciences, Vienna.

Bengio, Yoshua, Patrice Simard, and Paolo Frasconi. 1994. “Learning Long-Term Dependencies with Gradient Descent Is Difficult.” *IEEE Transactions on Neural Networks* 5 (2): 157–66.

Berchtold, André. 2001. “Estimation in the Mixture Transition Distribution Model.” *Journal of Time Series Analysis* 22 (4): 379–97.

Berchtold, André, and Adrian Raftery. 2002. “The Mixture Transition Distribution Model for High-Order Markov Chains and Non-Gaussian Time Series.” *Statistical Science* 17 (3):

328–56.

Bergmeir, Christoph. 2024a. “LLMs and Foundational Models: Not (yet) as Good as Hoped.” *Foresight: The International Journal of Applied Forecasting* 73.

Bergmeir, Christoph. 2024b. “LLMs and Foundational Models: Not (yet) as Good as Hoped.” *Foresight: The International Journal of Applied Forecasting* 73: 33–38.

Bergstra, James, and Yoshua Bengio. 2012. “Random Search for Hyper-Parameter Optimization.” *The Journal of Machine Learning Research* 13 (1): 281–305.

Bermúdez, Lluís, and Dimitris Karlis. 2022. “Copula-Based Bivariate Finite Mixture Regression Models with an Application for Insurance Claim Count Data.” *TEST* 31 (4): 1082–99.

Brown, Tom, Benjamin Mann, Nick Ryder, et al. 2020. “Language Models Are Few-Shot Learners.” *Advances in Neural Information Processing Systems* 33: 1877–901.

Chan, William, Navdeep Jaitly, Quoc V Le, and Oriol Vinyals. 2015. “Listen, Attend and Spell.” *arXiv Preprint arXiv:1508.01211*.

Chatterjee, Saptarshi, Shrabanti Chowdhury, Himel Mallick, Prithish Banerjee, and Broti Garai. 2018. “Group Regularization for Zero-Inflated Negative Binomial Regression

- Models with an Application to Health Care Demand in Germany.” *Statistics in Medicine* 37 (20): 3012–26.
- Chen, Gang. 2016. “A Gentle Tutorial of Recurrent Neural Network with Error Backpropagation.” *arXiv Preprint arXiv:1610.02583*.
- Chimmula, Vinay Kumar Reddy, and Lei Zhang. 2020. “Time Series Forecasting of COVID-19 Transmission in Canada Using LSTM Networks.” *Chaos, Solitons & Fractals* 135: 109864.
- Chiu, Chung-Cheng, Dieterich Lawson, Yuping Luo, et al. 2017. “An Online Sequence-to-Sequence Model for Noisy Speech Recognition.” *arXiv Preprint arXiv:1706.06428*.
- Cho, Kyunghyun, Bart Van Merriënboer, Caglar Gulcehre, et al. 2014. “Learning Phrase Representations Using RNN Encoder-Decoder for Statistical Machine Translation.” *arXiv Preprint arXiv:1406.1078*.
- Chowdhury, Shrabianti, Saptarshi Chatterjee, Himel Mallick, Prithish Banerjee, and Broti Garai. 2019. “Group Regularization for Zero-Inflated Poisson Regression Models with an Application to Insurance Ratemaking.” *Journal of Applied Statistics* 46 (9): 1567–81.
- D’Amico, Guglielmo, Riccardo De Blasis, and Filippo Petroni. 2023. “The Mixture Transition Distribution Approach to Networks: Evidence from Stock Markets.” *Physica A: Statistical*

Mechanics and Its Applications 632: 129335.

Das, Abhimanyu, Weihao Kong, Rajat Sen, and Yichen Zhou. 2024. *A Decoder-Only Foundation Model for Time-Series Forecasting*. <https://arxiv.org/abs/2310.10688>.

Denuit, Michel, and Philippe Lambert. 2005. “Constraints on Concordance Measures in Bivariate Discrete Data.” *Journal of Multivariate Analysis* 93 (1): 40–57.

Devlin, Jacob, Ming-Wei Chang, Kenton Lee, and Kristina Toutanova. 2019. “Bert: Pre-Training of Deep Bidirectional Transformers for Language Understanding.” *Proceedings of the 2019 Conference of the North American Chapter of the Association for Computational Linguistics: Human Language Technologies, Volume 1 (Long and Short Papers)*, 4171–86.

Dong, Chunjiao, Stephen H Richards, David B Clarke, Xuemei Zhou, and Zhuanglin Ma. 2014. “Examining Signalized Intersection Crash Frequency Using Multivariate Zero-Inflated Poisson Regression.” *Safety Science* 70: 63–69.

Duan, Naihua, Willard G Manning, Carl N Morris, and Joseph P Newhouse. 1983. “A Comparison of Alternative Models for the Demand for Medical Care.” *Journal of Business & Economic Statistics* 1 (2): 115–26.

Dzupire, Nelson Christopher, Philip Ngare, and Leo Odongo. 2018. “A Poisson-Gamma Model for Zero Inflated Rainfall Data.” *Journal of Probability and Statistics* 2018 (1):

1012647.

Ekambaram, Vijay, Arindam Jati, Pankaj Dayama, et al. 2024. *Tiny Time Mixers (TTMs): Fast Pre-Trained Models for Enhanced Zero/Few-Shot Forecasting of Multivariate Time Series*. <https://arxiv.org/abs/2401.03955>.

Feng, Tianshu. 2020. *Zero-Inflated Models for Semi-Continuous Transportation Data*. University of Washington.

Garza, Azul, Cristian Challu, and Max Mergenthaler-Canseco. 2024. *TimeGPT-1*. <https://arxiv.org/abs/2310.03589>.

Genest, Christian, and Johanna Nešlehová. 2007. “A Primer on Copulas for Count Data.” *ASTIN Bulletin: The Journal of the IAA* 37 (2): 475–515.

Gers, Felix A, and Jürgen Schmidhuber. 2000. “Recurrent Nets That Time and Count.” *Proceedings of the IEEE-INNS-ENNS International Joint Conference on Neural Networks. IJCNN 2000. Neural Computing: New Challenges and Perspectives for the New Millennium* 3: 189–94.

Gers, Felix A, Jürgen Schmidhuber, and Fred Cummins. 2000. “Learning to Forget: Continual Prediction with LSTM.” *Neural Computation* 12 (10): 2451–71.

Global Modeling and Assimilation Office (GMAO). 2015. *Tavg1_2d_slv_nx: MERRA-2 2D, 1-Hourly, Time-Averaged, Single-Level, Assimilation, Single-Level Diagnostics, V5.12.4*. Goddard Earth Sciences Data; Information Services Center (GES DISC). <https://doi.org/10.5067/VJAFPLI1CSIV>.

Goodfellow, Ian, Yoshua Bengio, Aaron Courville, and Yoshua Bengio. 2016. *Deep Learning*. MIT Press.

Graves, Alex, Marcus Liwicki, Santiago Fernández, Roman Bertolami, Horst Bunke, and Jürgen Schmidhuber. 2008. “A Novel Connectionist System for Unconstrained Handwriting Recognition.” *IEEE Transactions on Pattern Analysis and Machine Intelligence* 31 (5): 855–68.

Greff, Klaus, Rupesh K Srivastava, Jan Koutník, Bas R Steunebrink, and Jürgen Schmidhuber. 2016. “LSTM: A Search Space Odyssey.” *IEEE Transactions on Neural Networks and Learning Systems* 28 (10): 2222–32.

Hao, Wang, Yang Ya-dong, and Ma Yong. 2016. “Research on the Yangtze River Accident Casualties Using Zero-Inflated Negative Binomial Regression Technique.” *2016 IEEE International Conference on Intelligent Transportation Engineering (ICITE)*, 72–75.

Haq, Mohd Anul. 2022. “CDLSTM: A Novel Model for Climate Change Forecasting.” *Computers, Materials & Continua* 71 (2).

Hassan, Mohamed Yusuf. 2021. “The Deep Learning LSTM and MTD Models Best Predict Acute Respiratory Infection Among Under-Five-Year Old Children in Somaliland.” *Symmetry* 13 (7): 1156.

Hewamalage, Hansika, Klaus Ackermann, and Christoph Bergmeir. 2023a. “Forecast Evaluation for Data Scientists: Common Pitfalls and Best Practices.” *Data Mining and Knowledge Discovery* 37 (2): 788–832.

Hewamalage, Hansika, Klaus Ackermann, and Christoph Bergmeir. 2023b. “Forecast Evaluation for Data Scientists: Common Pitfalls and Best Practices.” *Data Mining and Knowledge Discovery* 37 (2): 788–832.

Hewamalage, Hansika, Christoph Bergmeir, and Kasun Bandara. 2021. “Recurrent Neural Networks for Time Series Forecasting: Current Status and Future Directions.” *International Journal of Forecasting* 37 (1): 388–427.

Hochreiter, Sepp, and Jürgen Schmidhuber. 1997. “Long Short-Term Memory.” *Neural Computation* 9 (8): 1735–80.

Hyndman, Rob J, and Gary K Grunwald. 2000. “Applications: Generalized Additive Modelling of Mixed Distribution Markov Models with Application to Melbourne’s Rainfall.” *Australian & New Zealand Journal of Statistics* 42 (2): 145–58.

Jiang, Yonglei, Adolf KY Ng, Yunpeng Wang, Lu Wang, and Bin Yu. 2018. “Locational Characteristics of Firms in the Business Service Industry in Airport Economic Zones: Case of Shanghai Hongqiao International Airport.” *Journal of Urban Planning and Development* 144 (1): 04018001.

Joe, Harry. 2014. *Dependence Modeling with Copulas*. CRC press.

Jordan, Michael I. 2004. “Graphical Models.” *Statistical Science* 19 (1): 140–55.

Kaewprasert, Theerapong, Sa-Aat Niwitpong, and Suparat Niwitpong. 2022. “Simultaneous Confidence Intervals for the Ratios of the Means of Zero-Inflated Gamma Distributions and Its Application.” *Mathematics* 10 (24): 4724.

Kaewprasert, Theerapong, Sa-Aat Niwitpong, and Suparat Niwitpong. 2024. “Bayesian Confidence Intervals for the Ratio of the Means of Zero-Inflated Gamma Distributions with Application to Rainfall Data.” *Communications in Statistics-Simulation and Computation* 53 (12): 5780–96.

Kingma, Diederik P, and Jimmy Ba. 2014. “Adam: A Method for Stochastic Optimization.” *arXiv Preprint arXiv:1412.6980*.

Lambert, Diane. 1992. “Zero-Inflated Poisson Regression, with an Application to Defects in Manufacturing.” *Technometrics* 34 (1): 1–14.

Le, Nhu D, R Douglas Martin, and Adrian Raftery. 1996. “Modeling Flat Stretches, Bursts Outliers in Time Series Using Mixture Transition Distribution Models.” *Journal of the American Statistical Association* 91 (436): 1504–15.

Lele, Subhash R, Brian Dennis, and Frithjof Lutscher. 2007. “Data Cloning: Easy Maximum Likelihood Estimation for Complex Ecological Models Using Bayesian Markov Chain Monte Carlo Methods.” *Ecology Letters* 10 (7): 551–63.

Lele, Subhash R, Khurram Nadeem, and Byron Schmuland. 2010. “Estimability and Likelihood Inference for Generalized Linear Mixed Models Using Data Cloning.” *Journal of the American Statistical Association* 105 (492): 1617–25.

Liang, Yuxuan, Haomin Wen, Yuqi Nie, et al. 2024. “Foundation Models for Time Series Analysis: A Tutorial and Survey.” *Proceedings of the 30th ACM SIGKDD Conference on Knowledge Discovery and Data Mining*, 6555–65.

Liu, Chenhui, Mo Zhao, Wei Li, and Anuj Sharma. 2018. “Multivariate Random Parameters Zero-Inflated Negative Binomial Regression for Analyzing Urban Midblock Crashes.” *Analytic Methods in Accident Research* 17: 32–46.

Liu, Lei, Ya-Chen Tina Shih, Robert L Strawderman, Daowen Zhang, Bankole A Johnson, and Haitao Chai. 2019. “Statistical Analysis of Zero-Inflated Nonnegative Continuous Data.” *Statistical Science* 34 (2): 253–79.

- Madsen, Lisa. 2009. “Maximum Likelihood Estimation of Regression Parameters with Spatially Dependent Discrete Data.” *Journal of Agricultural, Biological, and Environmental Statistics* 14: 375–91.
- Manero, Jaume, Javier Béjar, and Ulises Cortés. 2018. “Wind Energy Forecasting with Neural Networks: A Literature Review.” *Computación y Sistemas* 22 (4): 1085–98.
- Martin, Tara G, Brendan A Wintle, Jonathan R Rhodes, et al. 2005. “Zero Tolerance Ecology: Improving Ecological Inference by Modelling the Source of Zero Observations.” *Ecology Letters* 8 (11): 1235–46.
- Mathew, Jacob, and Rahim F Benekohal. 2021. “Highway-Rail Grade Crossings Accident Prediction Using Zero Inflated Negative Binomial and Empirical Bayes Method.” *Journal of Safety Research* 79: 211–36.
- Mikolov, Tomáš. 2012. *Statistical Language Models Based on Neural Networks*. Brno University of Technology.
- Mills, Elizabeth Dastrup. 2013. *Adjusting for Covariates in Zero-Inflated Gamma and Zero-Inflated Log-Normal Models for Semicontinuous Data*. The University of Iowa.
- Monleon, Vicente J, Lisa Madsen, and Lisa C Wilson. 2019. “Small Area Estimation of Zero-Inflated, Spatially Correlated Forest Variables Using Copula Models.” *Celebrating*

Progress, Possibilities, and Partnerships, 93.

Mosshammer, Sebastian. 2016. *Assessing the Validity of MERRA Reanalysis Data for Simulation of Wind Power Production*. University of Natural Resources; Life Sciences, Vienna.

Mozer, Michael C. 2013. “A Focused Backpropagation Algorithm for Temporal Pattern Recognition.” In *Backpropagation*. Psychology Press.

Mullahy, John. 1986. “Specification and Testing of Some Modified Count Data Models.” *Journal of Econometrics* 33 (3): 341–65.

Muncharaz, Javier Oliver. 2020. “Comparing Classic Time Series Models and the LSTM Recurrent Neural Network: An Application to s&p 500 Stocks.” *Finance, Markets and Valuation* 6 (2): 137–48.

Neal, Radford M. 2003. “Slice Sampling.” *The Annals of Statistics* 31 (3): 705–67.

Neelon, Brian, A James O’Malley, and Valerie A Smith. 2016a. “Modeling Zero-Modified Count and Semicontinuous Data in Health Services Research Part 1: Background and Overview.” *Statistics in Medicine* 35 (27): 5070–93.

Neelon, Brian, A James O’Malley, and Valerie A Smith. 2016b. “Modeling Zero-Modified

Count and Semicontinuous Data in Health Services Research Part 2: Case Studies.” *Statistics in Medicine* 35 (27): 5094–112.

Neelon, Brian, Li Zhu, and Sara E Benjamin Neelon. 2015. “Bayesian Two-Part Spatial Models for Semicontinuous Data with Application to Emergency Department Expenditures.” *Biostatistics* 16 (3): 465–79.

Olah, Christopher. 2015. *Understanding LSTM Networks*. <https://colah.github.io/posts/2015-08-Understanding-LSTMs/>.

Paramasivan, Senthil Kumar. 2021. “Deep Learning Based Recurrent Neural Networks to Enhance the Performance of Wind Energy Forecasting: A Review.” *Revue d’Intelligence Artificielle* 35 (1).

Pirani, Muskaan, Paurav Thakkar, Pranay Jivrani, Mohammed Husain Bohara, and Dweepna Garg. 2022. “A Comparative Analysis of ARIMA, GRU, LSTM and BiLSTM on Financial Time Series Forecasting.” *2022 IEEE International Conference on Distributed Computing and Electrical Circuits and Electronics (ICDCECE)*, 1–6.

Pizer, Steven D, and Julia C Prentice. 2011. “Time Is Money: Outpatient Waiting Times and Health Insurance Choices of Elderly Veterans in the United States.” *Journal of Health Economics* 30 (4): 626–36.

Planas, Christophe, and Alessandro Rossi. 2024. “The Slice Sampler and Centrally Symmetric Distributions.” *Monte Carlo Methods and Applications* 30 (3): 299–313.

Raftery, Adrian. 1985a. “A Model for High-Order Markov Chains.” *Journal of the Royal Statistical Society Series B: Statistical Methodology* 47 (3): 528–39.

Raftery, Adrian. 1985b. “A New Model for Discrete-Valued Time Series: Autocorrelations and Extensions.” *Rassegna Di Metodi Statistici Ed Applicazioni* 3 (4): 149–62.

Raftery, Adrian. 1994. “Change Point and Change Curve Modeling in Stochastic Processes and Spatial Statistics.” *Journal of Applied Statistical Science* 1 (4): 403–23.

Rasul, Kashif, Arjun Ashok, Andrew Robert Williams, et al. 2024. *Lag-Llama: Towards Foundation Models for Probabilistic Time Series Forecasting*. <https://arxiv.org/abs/2310.08278>.

Robinson, Anthony J, and Frank Fallside. 1987. *The Utility Driven Dynamic Error Propagation Network*. Vol. 11. University of Cambridge Department of Engineering Cambridge.

Rumelhart, David E, Geoffrey E Hinton, and Ronald J Williams. 1986. “Learning Representations by Back-Propagating Errors.” *Nature* 323 (6088): 533–36.

Salman, Afan Galih, Yaya Heryadi, Edi Abdurahman, and Wayan Suparta. 2018. “Sin-

- gle Layer & Multi-Layer Long Short-Term Memory (LSTM) Model with Intermediate Variables for Weather Forecasting.” *Procedia Computer Science* 135: 89–98.
- Sandhu, KS, Anil Ramachandran Nair, et al. 2019. “A Comparative Study of ARIMA and RNN for Short Term Wind Speed Forecasting.” *2019 10th International Conference on Computing, Communication and Networking Technologies (ICCCNT)*, 1–7.
- Sherstinsky, Alex. 2020. “Fundamentals of Recurrent Neural Network (RNN) and Long Short-Term Memory (LSTM) Network.” *Physica D: Nonlinear Phenomena* 404: 132306.
- Shi, Peng, and Lu Yang. 2018. “Pair Copula Constructions for Insurance Experience Rating.” *Journal of the American Statistical Association* 113 (521): 122–33.
- Siami-Namini, Sima, Neda Tavakoli, and Akbar Siami Namin. 2019. “A Comparative Analysis of Forecasting Financial Time Series Using Arima, Lstm, and Bilstm.” *arXiv Preprint arXiv:1911.09512*.
- Simmachan, T, and P Boonkrong. 2024. “A Comparison of Count and Zero-Inflated Regression Models for Predicting Claim Frequencies in Thai Automobile Insurance.” *Lobachevskii Journal of Mathematics* 45 (12): 6400–6414.
- Sklar, M. 1959. “Fonctions de répartition à n Dimensions Et Leurs Marges.” *Annales de l'ISUP* 8: 229–31.

- Slime, Mekdad, Abdellah Ould Khal, Abdelhak Zoglat, Mohammed El Kamli, and Brahim Batti. 2025. “Optimizing Automobile Insurance Pricing: A Generalized Linear Model Approach to Claim Frequency and Severity.” *Statistics, Optimization & Information Computing*.
- Sun, Nick. 2020. *Comparison of Gaussian Copula and Random Forests in Zero-Inflated Spatial Prediction for Forestry Applications*.
- Sutskever, Ilya, Oriol Vinyals, and Quoc V Le. 2014. “Sequence to Sequence Learning with Neural Networks.” *Advances in Neural Information Processing Systems* 27.
- Vaswani, Ashish, Noam Shazeer, Niki Parmar, et al. 2017. “Attention Is All You Need.” *Advances in Neural Information Processing Systems* 30.
- Wang, Peipei, Xinqi Zheng, Gang Ai, Dongya Liu, and Bangren Zhu. 2020. “Time Series Prediction for the Epidemic Trends of COVID-19 Using the Improved LSTM Deep Learning Method: Case Studies in Russia, Peru and Iran.” *Chaos, Solitons & Fractals* 140: 110214.
- Werbos, P. J. 1990. “Backpropagation Through Time: What It Does and How to Do It.” *Proceedings of the IEEE* 78 (10): 1550–60. <https://doi.org/10.1109/5.58337>.
- Werbos, Paul J. 1988. “Generalization of Backpropagation with Application to a Recurrent

Gas Market Model.” *Neural Networks* 1 (4): 339–56.

Wikle, Christopher K, and Andrew Zammit-Mangion. 2023. “Statistical Deep Learning for Spatial and Spatiotemporal Data.” *Annual Review of Statistics and Its Application* 10 (1): 247–70.

Woo, Gerald, Chenghao Liu, Akshat Kumar, Caiming Xiong, Silvio Savarese, and Doyen Sahoo. 2024. *Unified Training of Universal Time Series Forecasting Transformers*. <https://arxiv.org/abs/2402.02592>.

Yang, Lu. 2022. “Nonparametric Copula Estimation for Mixed Insurance Claim Data.” *Journal of Business & Economic Statistics* 40 (2): 537–46.

Yang, Ming, Joseph E Cavanova, and Gideon KD Zamba. 2015. “State-Space Models for Count Time Series with Excess Zeros.” *Statistical Modelling* 15 (1): 70–90.

Young, Derek S, Eric S Roemmele, and Xuan Shi. 2022. “Zero-Inflated Modeling Part II: Zero-Inflated Models for Complex Data Structures.” *Wiley Interdisciplinary Reviews: Computational Statistics* 14 (2): e1540.

Young, Derek S, Eric S Roemmele, and Peng Yeh. 2022. “Zero-Inflated Modeling Part i: Traditional Zero-Inflated Count Regression Models, Their Applications, and Computational Tools.” *Wiley Interdisciplinary Reviews: Computational Statistics* 14 (1): e1541.

Yu, Yong, Xiaosheng Si, Changhua Hu, and Jianxun Zhang. 2019. “A Review of Recurrent Neural Networks: LSTM Cells and Network Architectures.” *Neural Computation* 31 (7): 1235–70.

Yu, Yunjun, Junfei Cao, and Jianyong Zhu. 2019. “An LSTM Short-Term Solar Irradiance Forecasting Under Complicated Weather Conditions.” *IEEE Access* 7: 145651–66.

Zhang, Pengcheng, David Pitt, and Xueyuan Wu. 2022. “A New Multivariate Zero-Inflated Hurdle Model with Applications in Automobile Insurance.” *ASTIN Bulletin: The Journal of the IAA* 52 (2): 393–416.

Zheng, Xiaotian, Athanasios Kottas, and Bruno Sansó. 2022. “On Construction and Estimation of Stationary Mixture Transition Distribution Models.” *Journal of Computational and Graphical Statistics* 31 (1): 283–93.

Zheng, Xiaotian, Athanasios Kottas, and Bruno Sansó. 2023a. “Bayesian Geostatistical Modeling for Discrete-Valued Processes.” *Environmetrics* 34 (7): e2805.

Zheng, Xiaotian, Athanasios Kottas, and Bruno Sansó. 2023b. “Nearest-Neighbor Mixture Models for Non-Gaussian Spatial Processes.” *Bayesian Analysis* 18 (4): 1191–222.

Zhou, Xiaoxiao, Kai Kang, and Xinyuan Song. 2020. “Two-Part Hidden Markov Models for Semicontinuous Longitudinal Data with Nonignorable Missing Covariates.” *Statistics in*

Medicine 39 (13): 1801–16.

Zou, Yixuan, and Derek S Young. 2024. “Fiducial-Based Statistical Intervals for Zero-Inflated Gamma Data.” *Journal of Statistical Theory and Practice* 18 (1): 12.

APPENDICES

Appendix A: PDF and CDF Plots for Zero-Inflated Gamma MTD Models

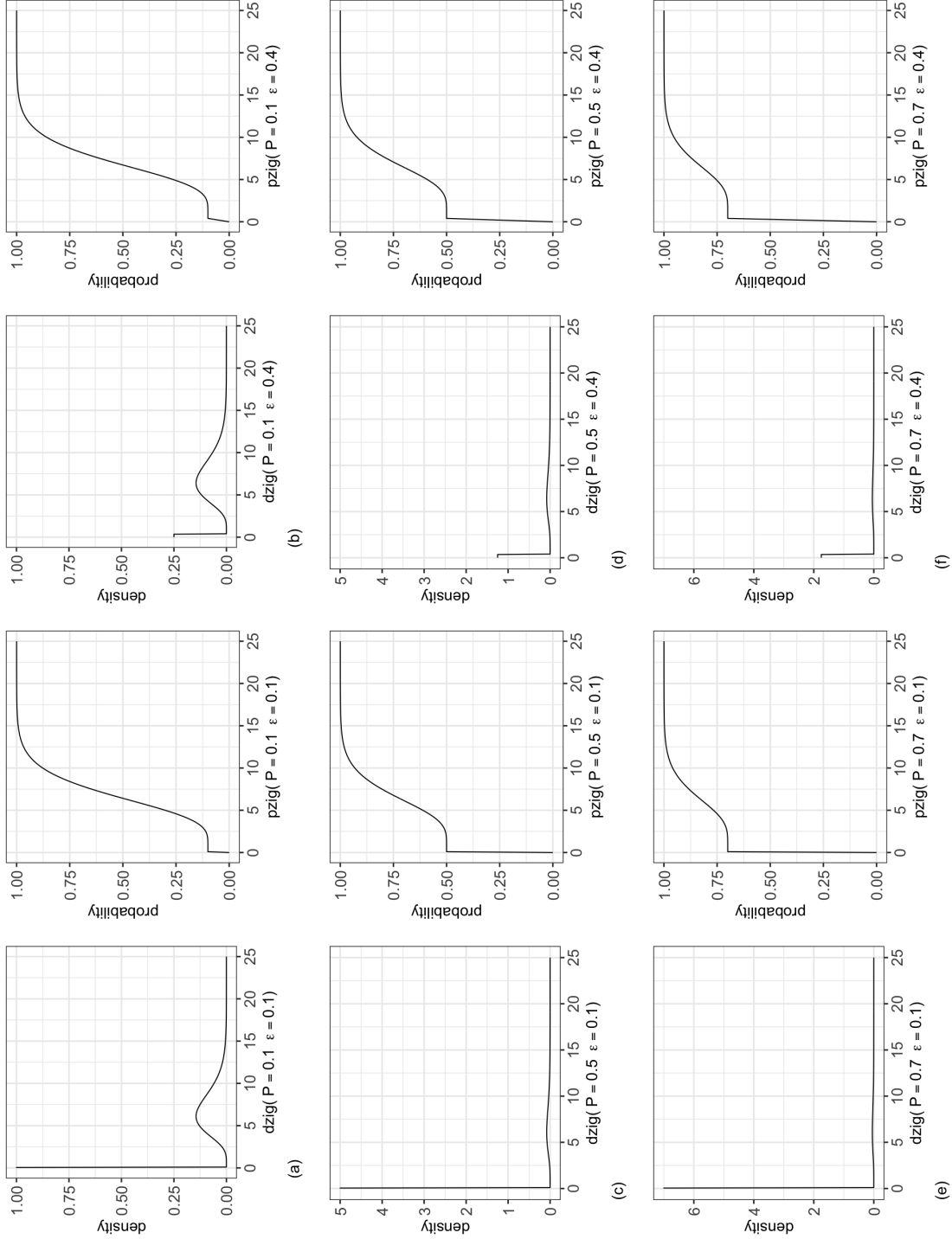


Figure A.1: (a), (b): $ZIGamma(\mu = 7, \beta = 1, P = 0.1, \epsilon = 0.1, 0.4)$; (c), (d): $ZIGamma(\mu = 7, \beta = 1, P = 0.5, \epsilon = 0.1, 0.4)$; (e), (f): $ZIGamma(\mu = 7, \beta = 1, P = 0.7, \epsilon = 0.1, 0.4)$. (Left) Probability density function (PDF) and (Right) cumulative distribution function (CDF) of the zero-inflated gamma distribution with varying parameters.

Appendix B: Simulations for Gamma MTD Models

B.1 Simulation Results

B.1.1 Convergence Diagnostics

B.1.1.1 Gelman-Rubin and ACF Plots

B.1.1.2 Trace and Density Plots

B.1.2 Weight and Dependence Parameters for Copula

B.1.3 Parameters for Marginal Distribution

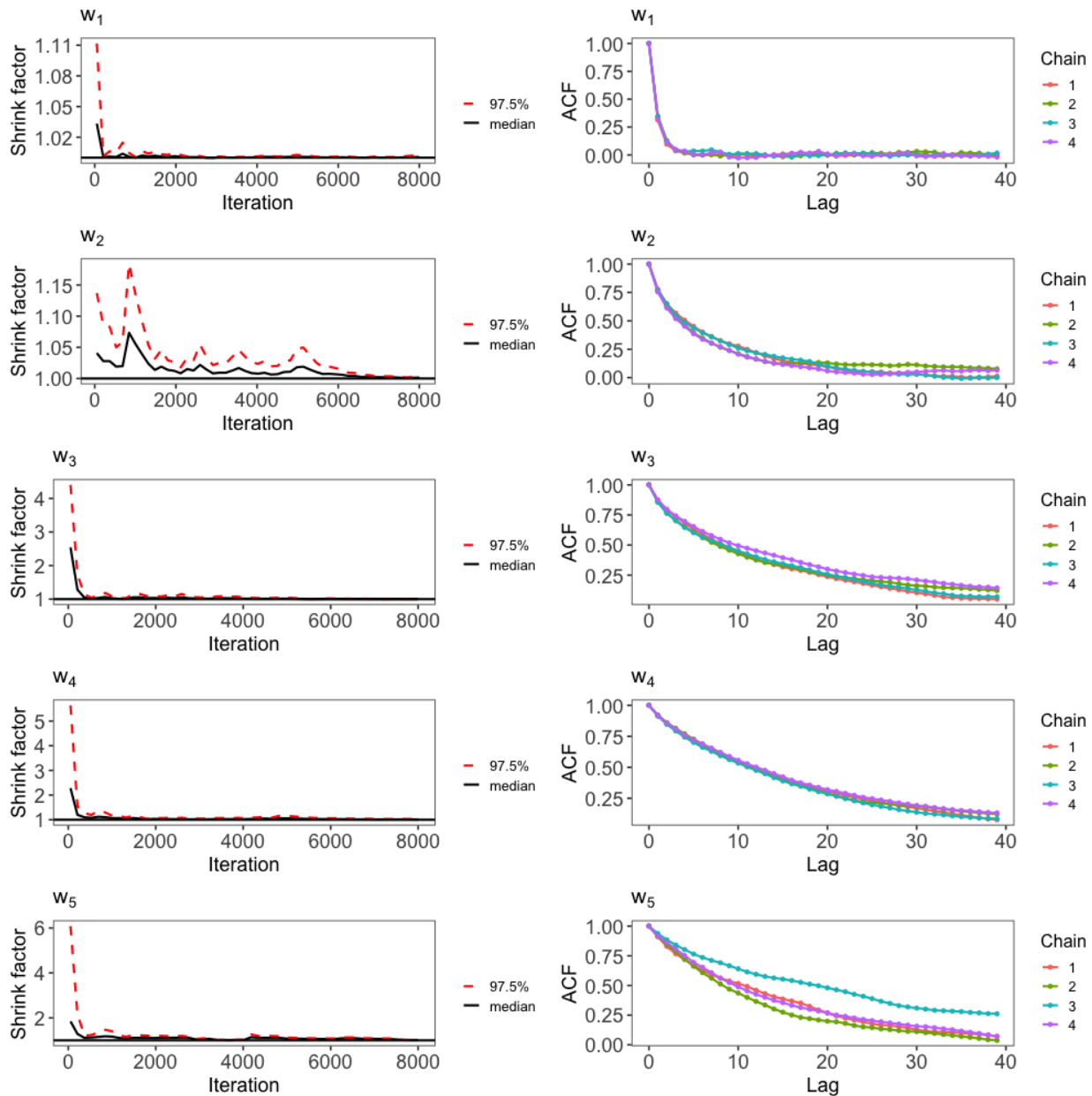


Figure B.1: (Left) Gelman-Rubin and (Right) ACF plot for Scenario 1's w .

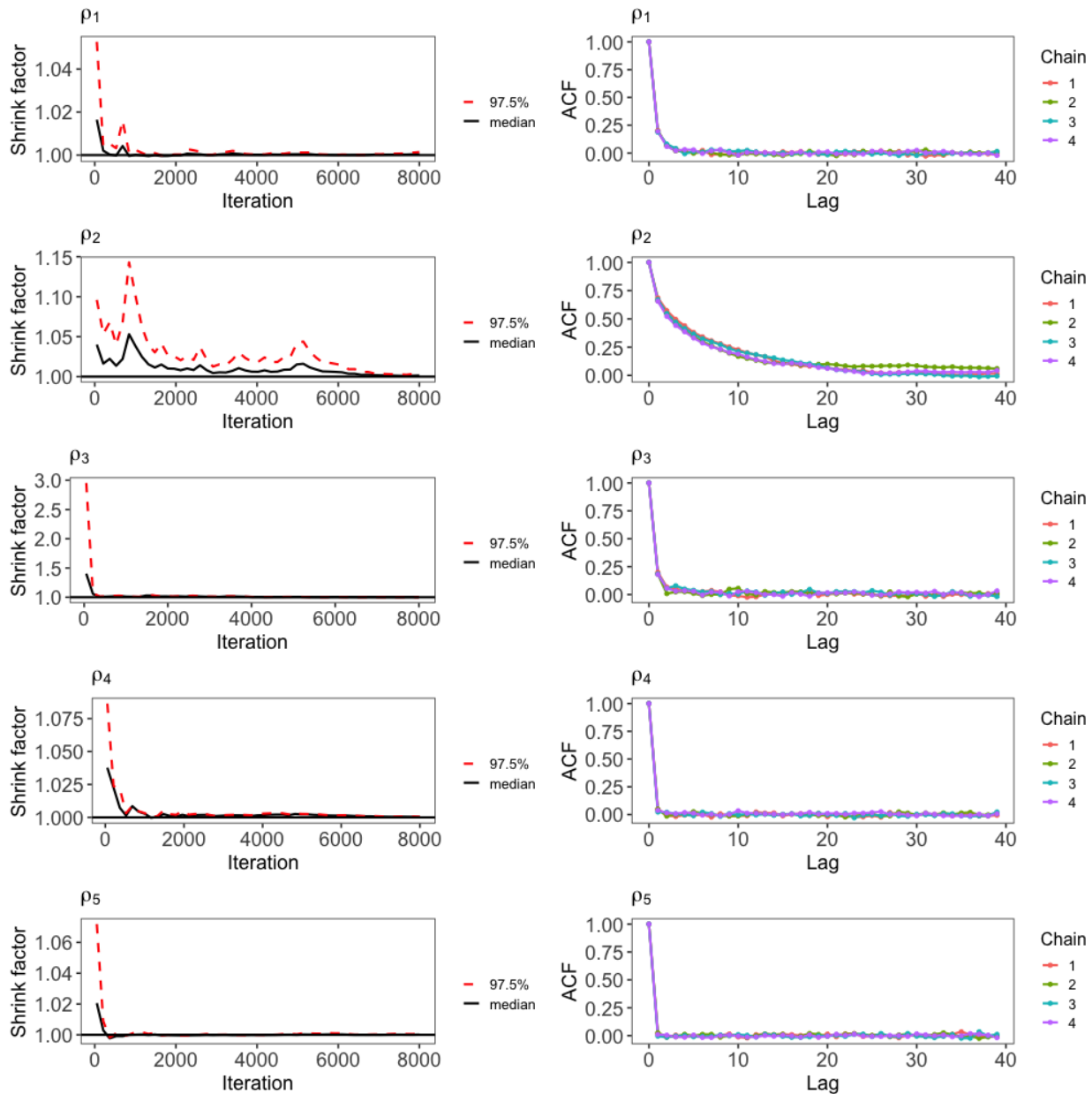


Figure B.2: (Left) Gelman-Rubin and (Right) ACF plot for Scenario 1's ρ .

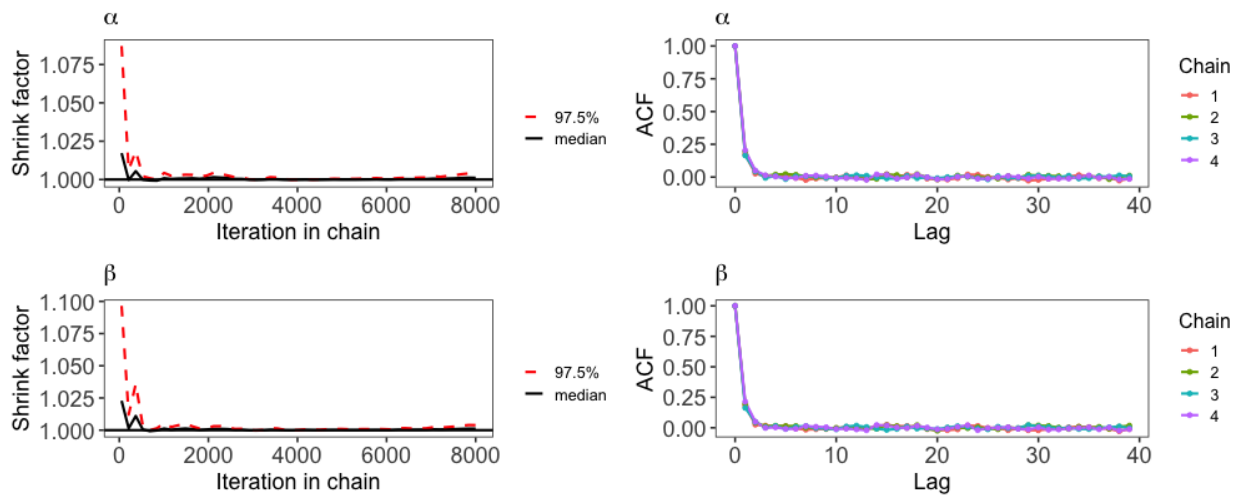


Figure B.3: (Left) Gelman-Rubin and (Right) ACF plot for Scenario 1's α, β .

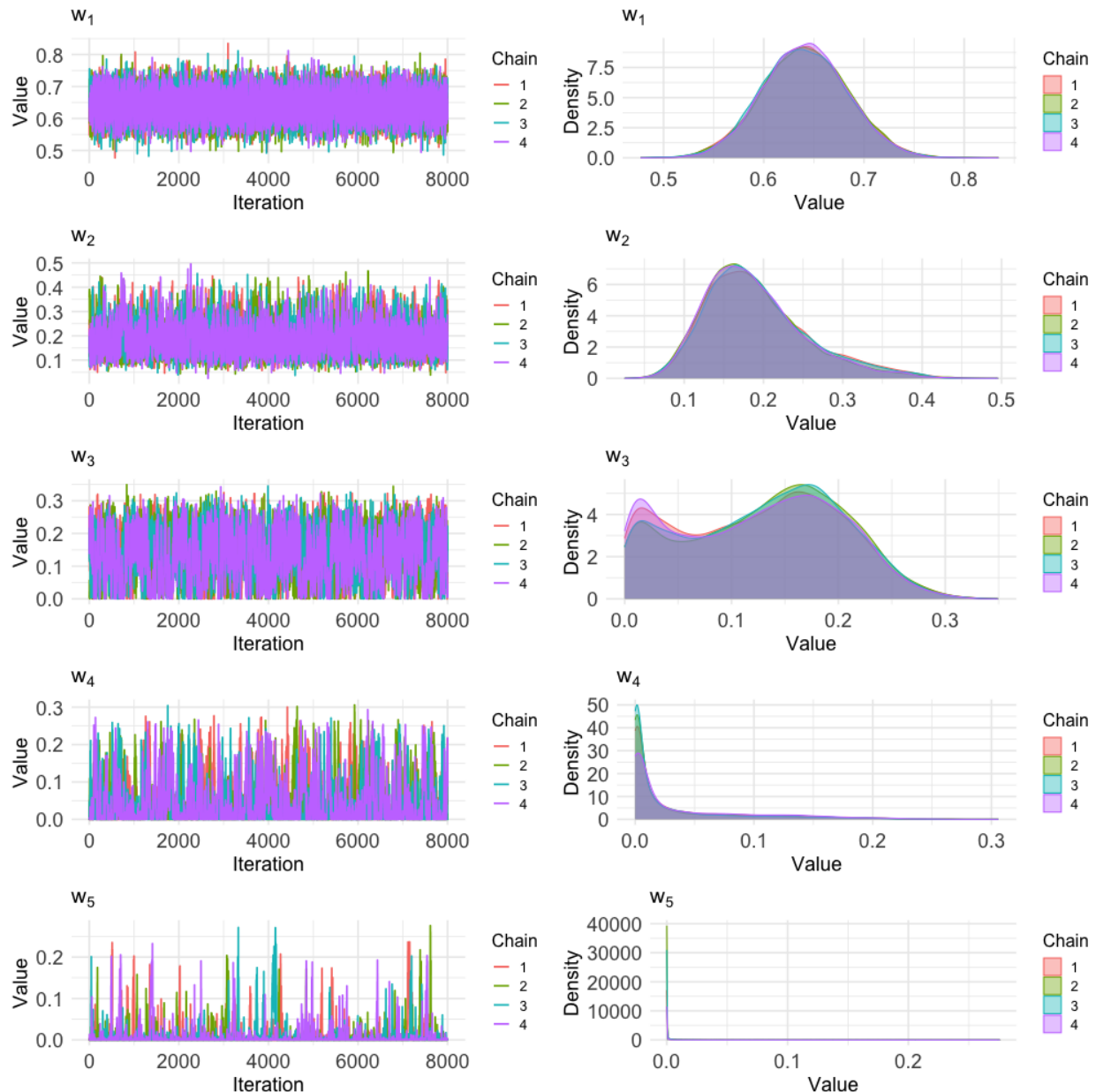


Figure B.4: (Left) Trace and (Right) density plot for Scenario 1's w .

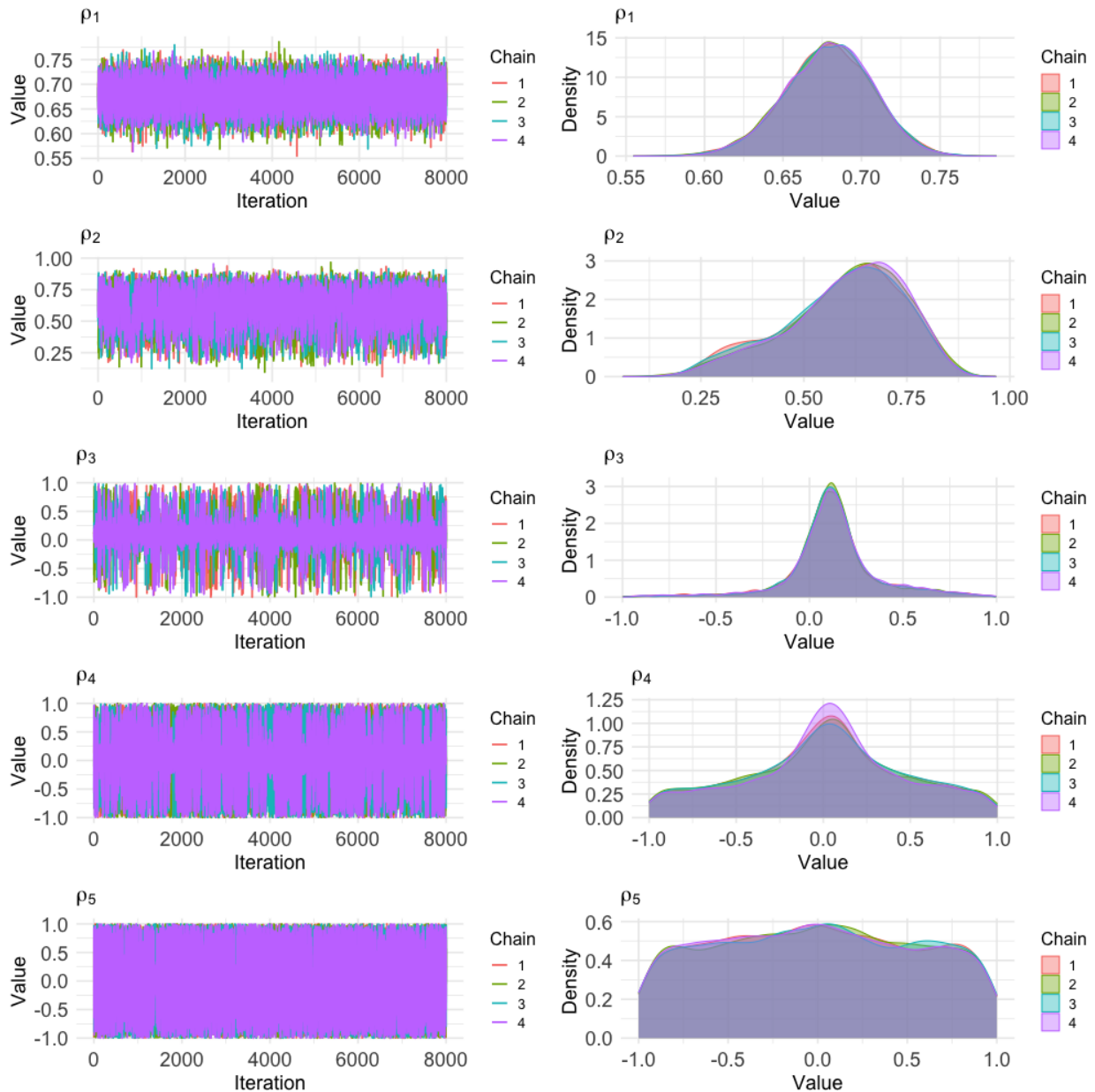


Figure B.5: (Left) Trace and (Right) density plot for Scenario 1's ρ .

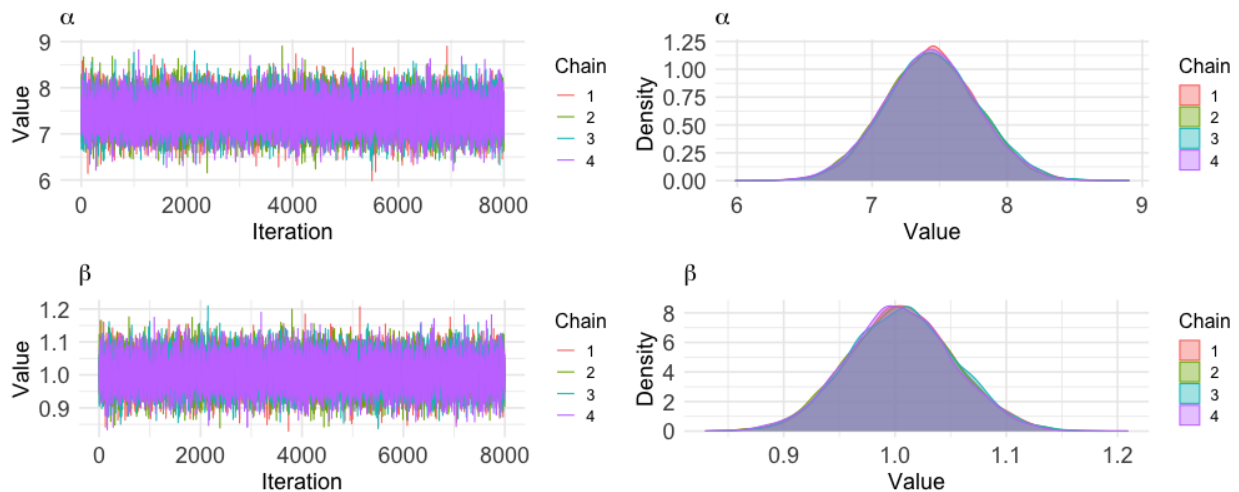


Figure B.6: (Left) Trace and (Right) density plot for Scenario 1's α, β .

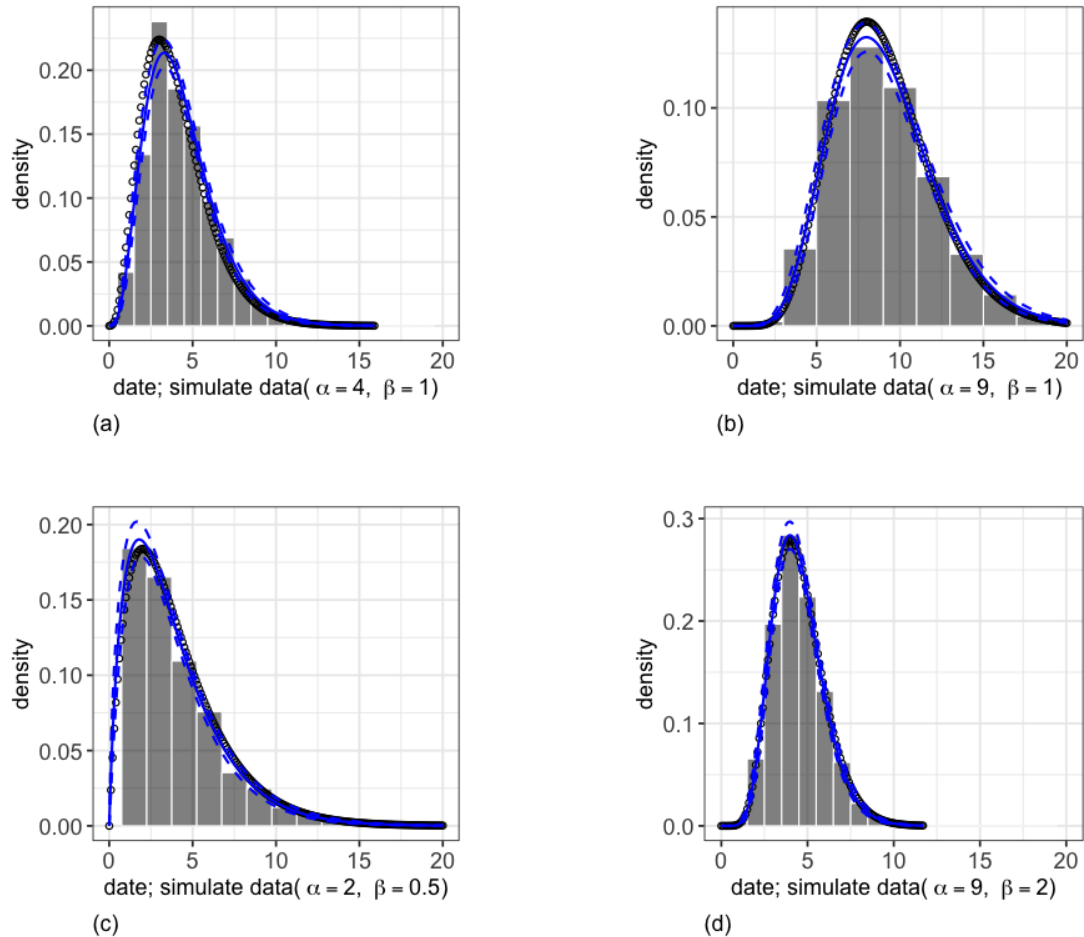


Figure B.7: Results for Scenario 3-6. Grey bars are histogram of the data. Circles are the true gamma density evaluated at the support, i.e., $x > 0$. Solid lines are the posterior means. Dashed lines are 95% credible intervals.

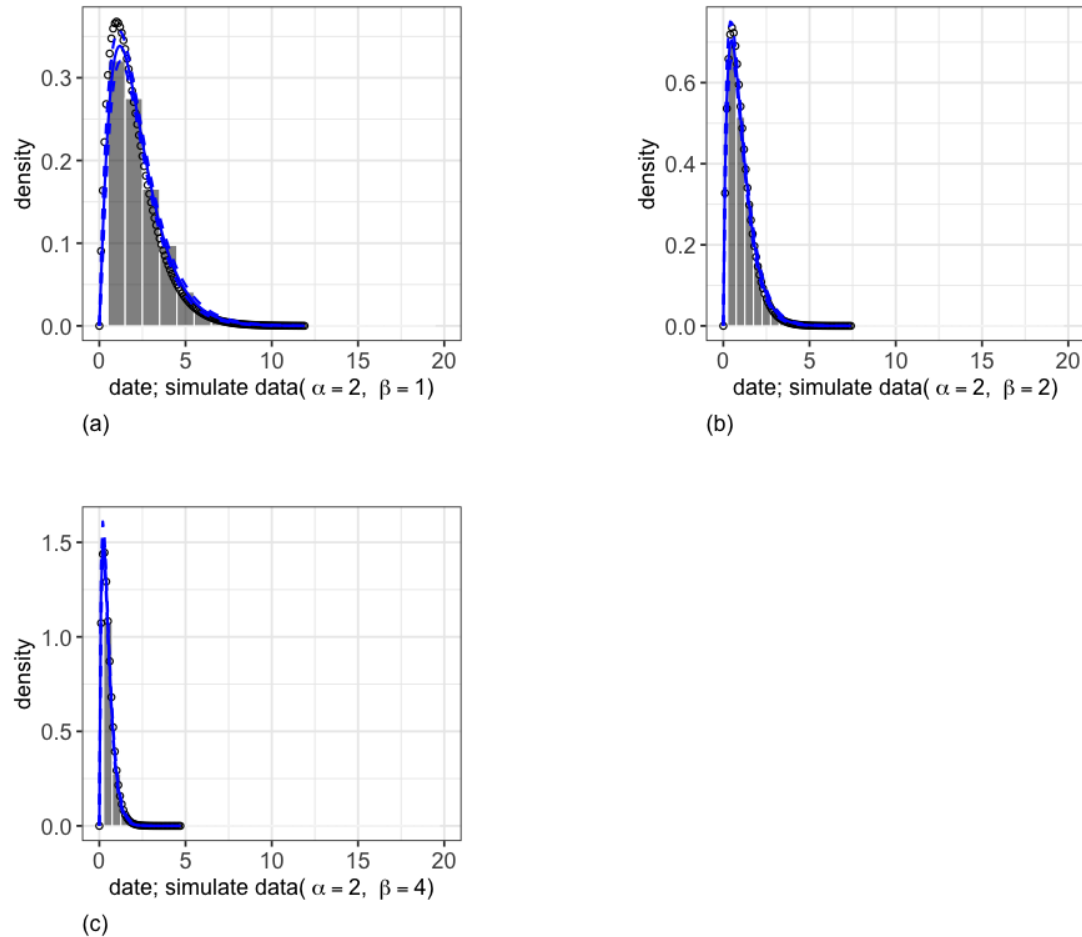


Figure B.8: Results for Scenario 7-9. Grey bars are histogram of the data. Circles are the true gamma density evaluated at the support, i.e., $x > 0$. Solid lines are the posterior means. Dashed lines are 95% credible intervals.

Appendix C: Simulations for Zero-Inflated Gamma MTD Models

C.1 Simulation Results

C.1.1 Convergence Diagnostics

C.1.1.1 Gelman-Rubin and ACF Plots

C.1.1.2 Trace and Density Plots

C.1.2 Weight and Dependence Parameters for Copula

C.1.3 Parameters for Marginal Distribution

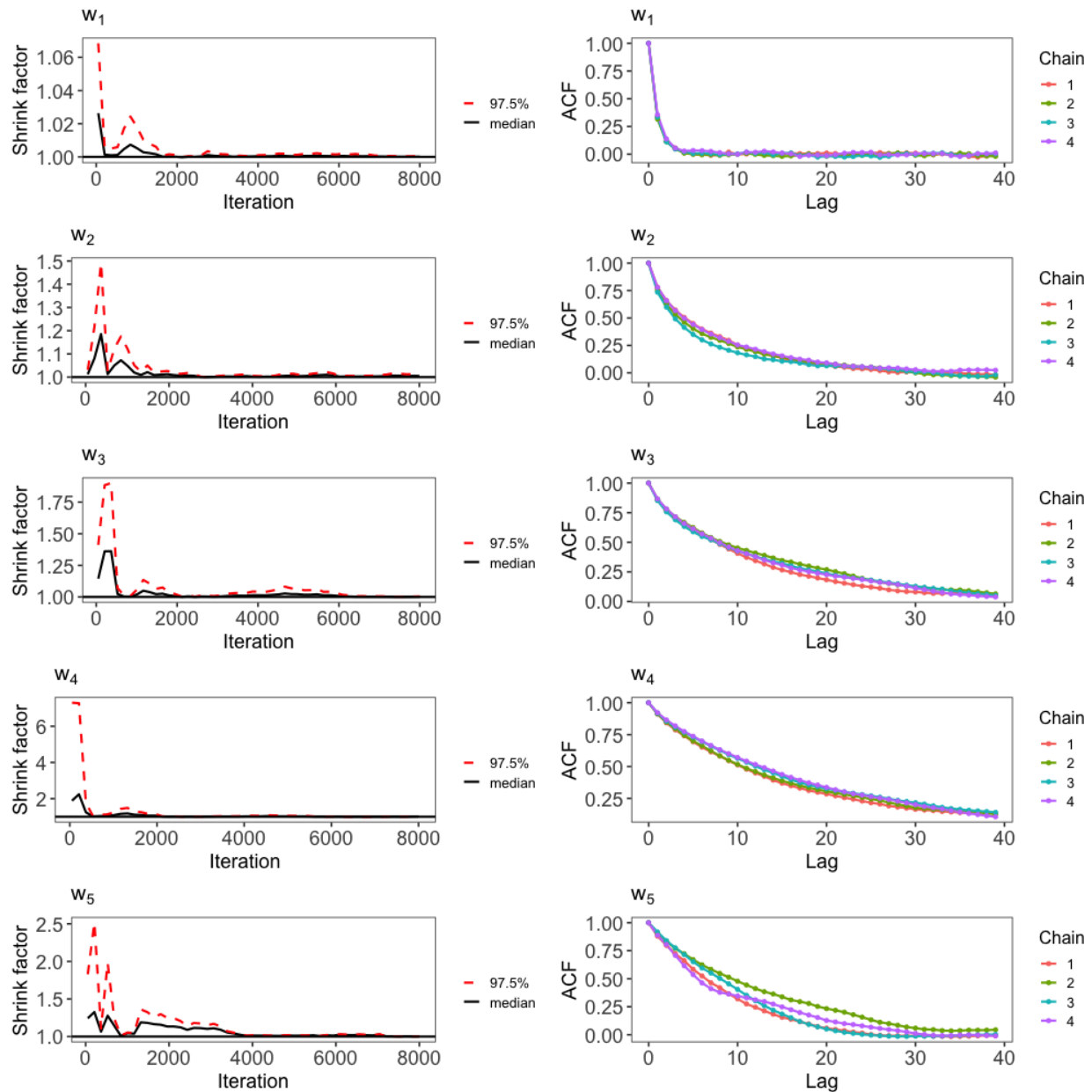


Figure C.1: (Left) Gelman-Rubin and (Right) ACF plot for Scenario 1's w .

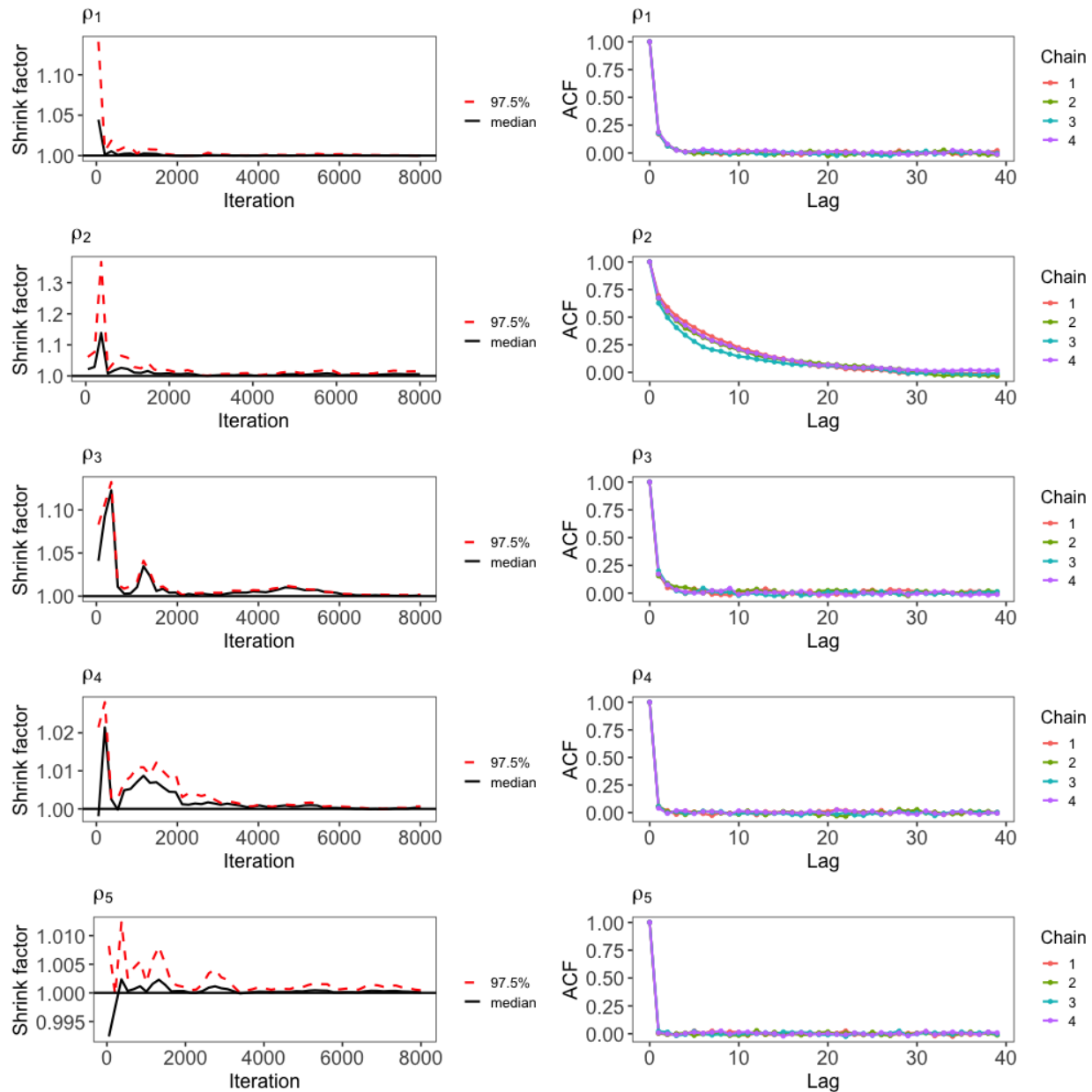


Figure C.2: (Left) Gelman-Rubin and (Right) ACF plot for Scenario 1's ρ .

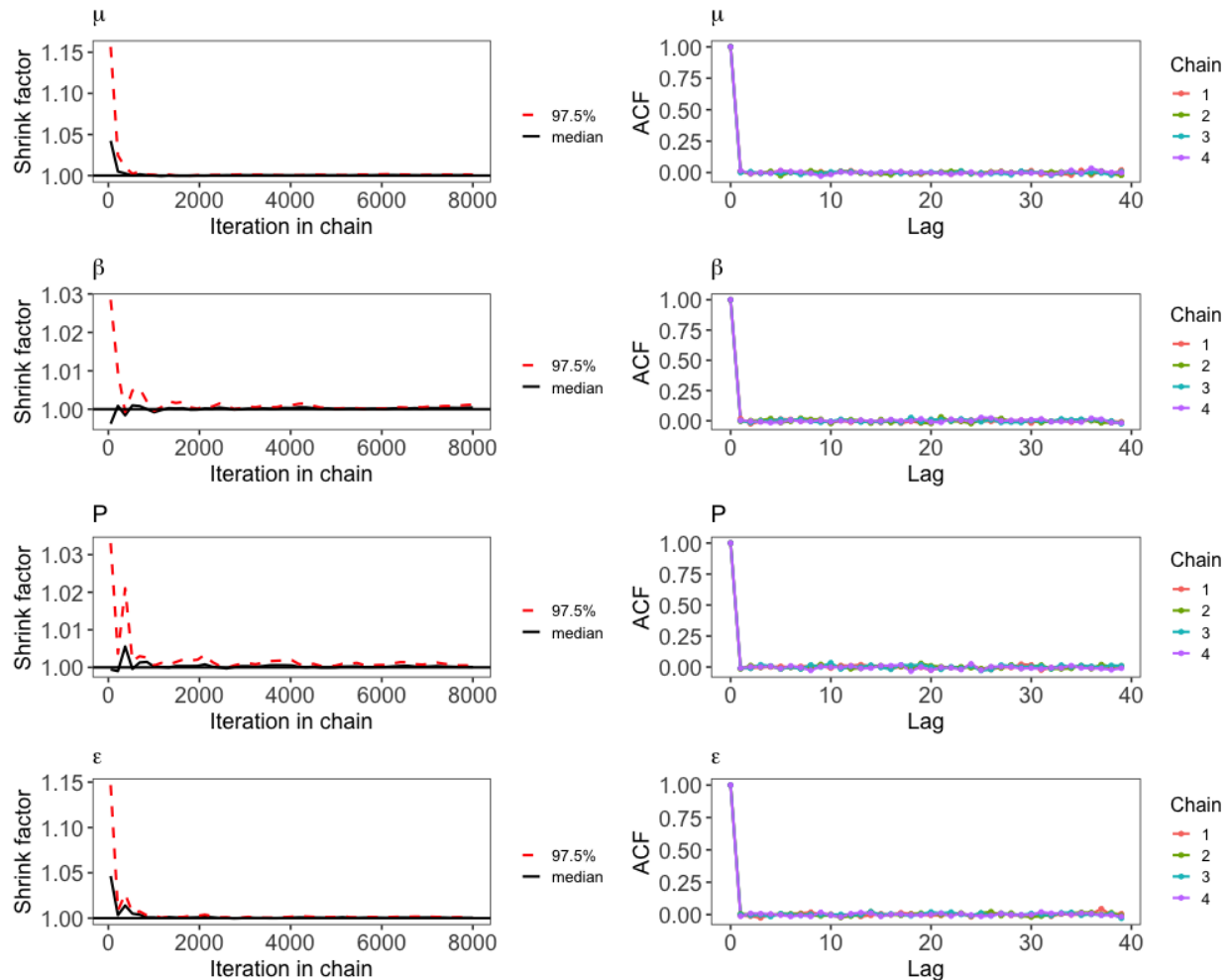


Figure C.3: (Left) Gelman-Rubin and (Right) ACF plot for Scenario 1's μ, β, P, ϵ .

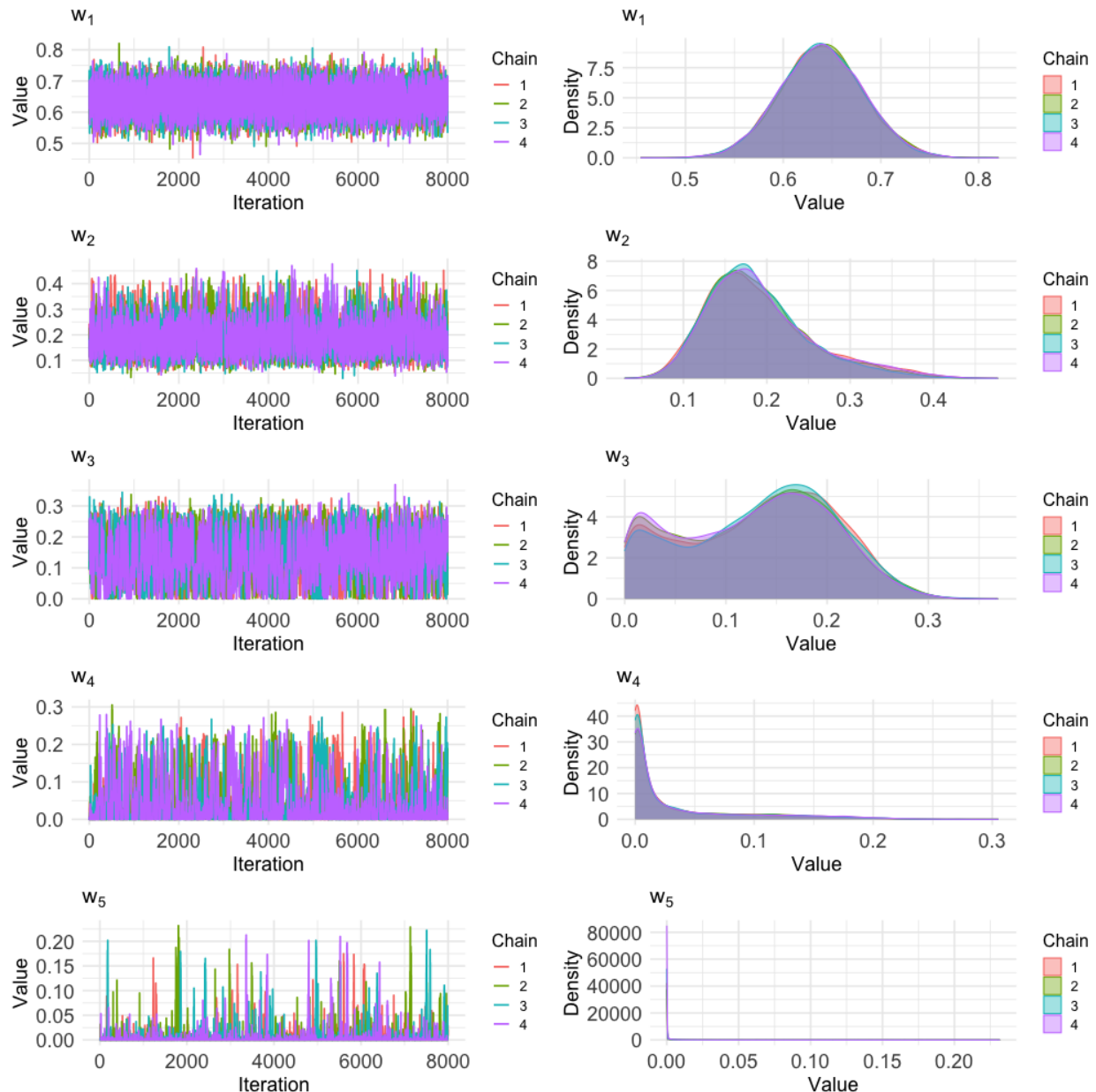


Figure C.4: (Left) Trace and (Right) density plot for Scenario 1's w .

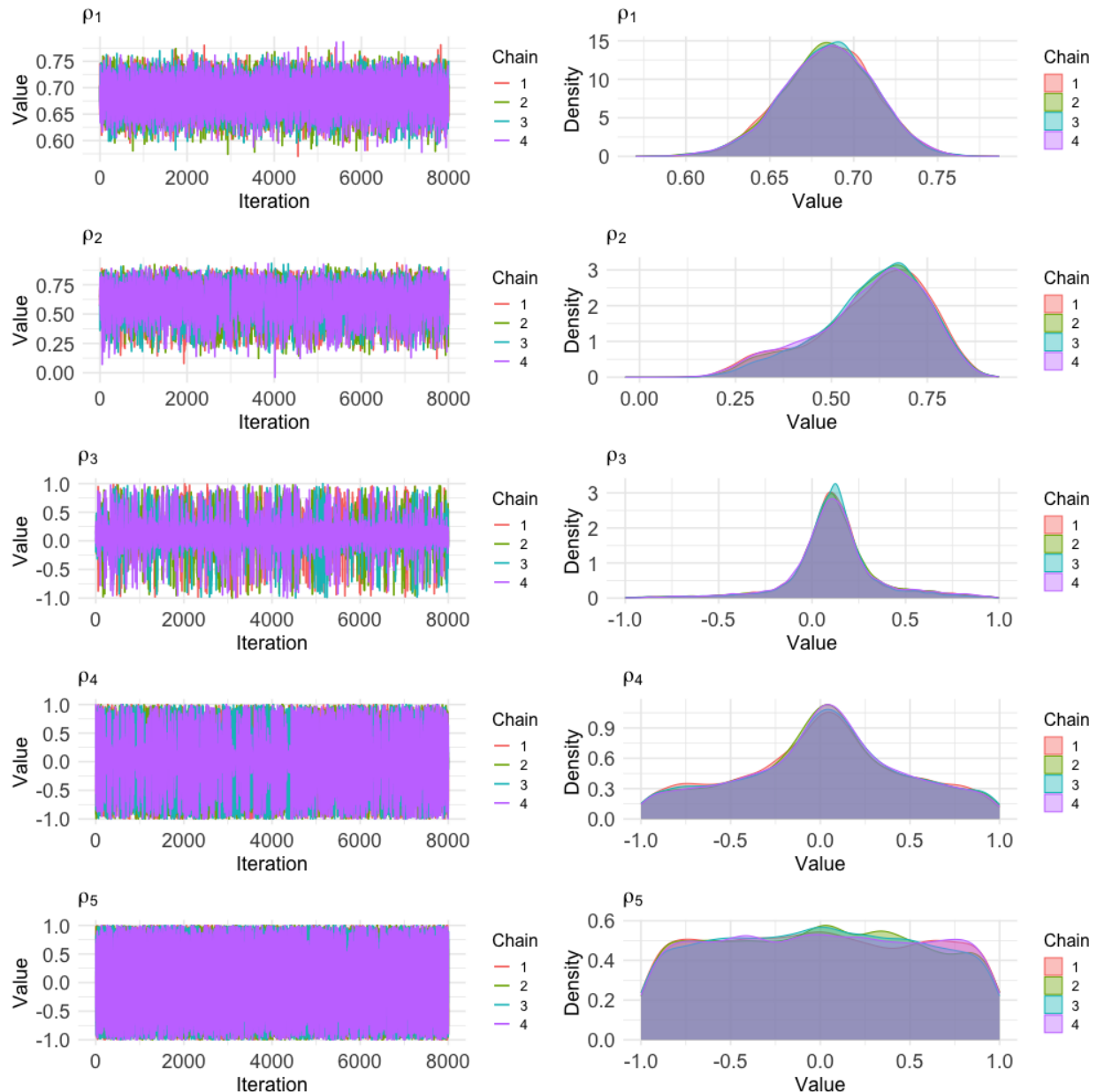


Figure C.5: (Left) Trace and (Right) density plot for Scenario 1's ρ .

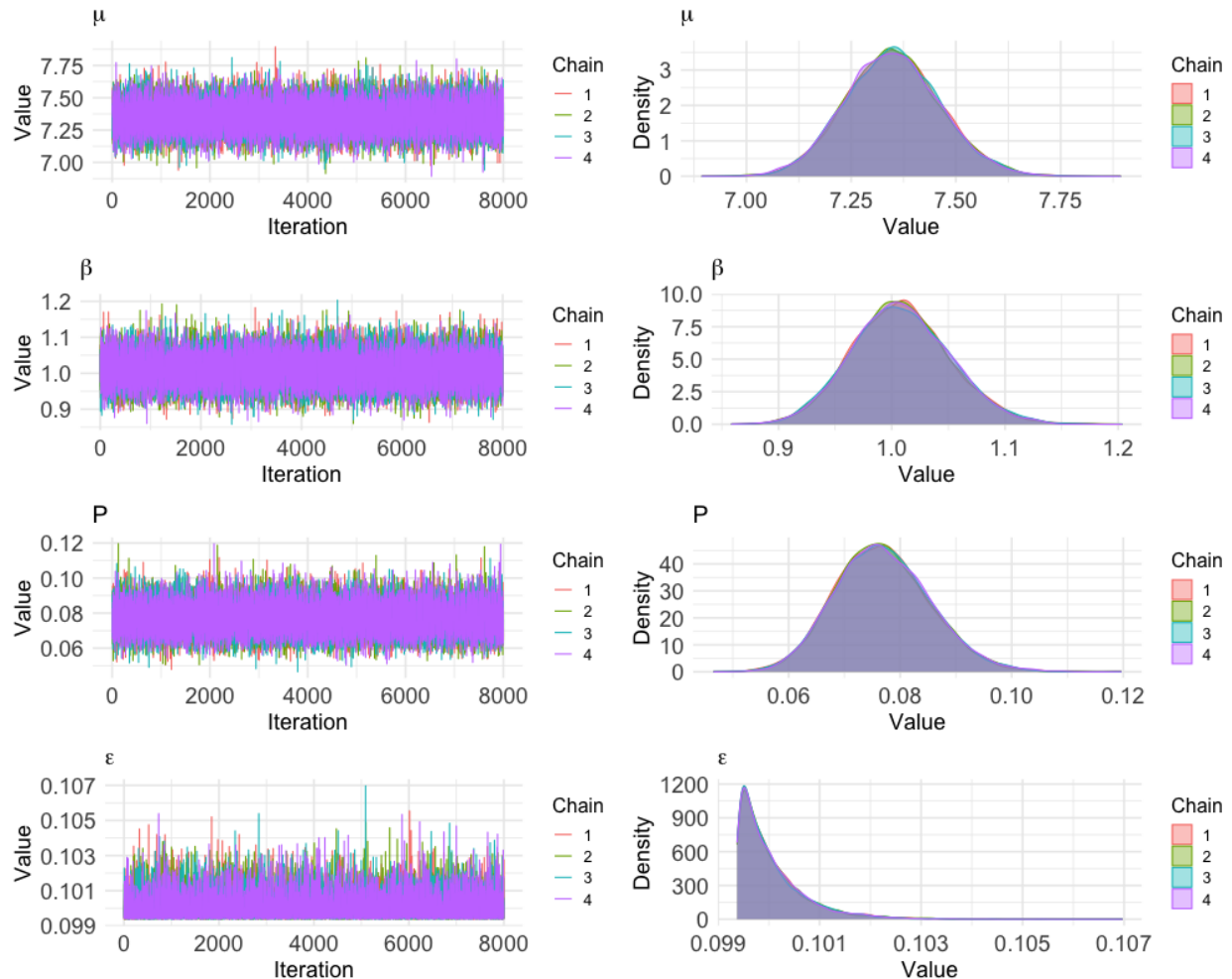


Figure C.6: (Left) Trace and (Right) density plot for Scenario 1's μ, β, P, ϵ .

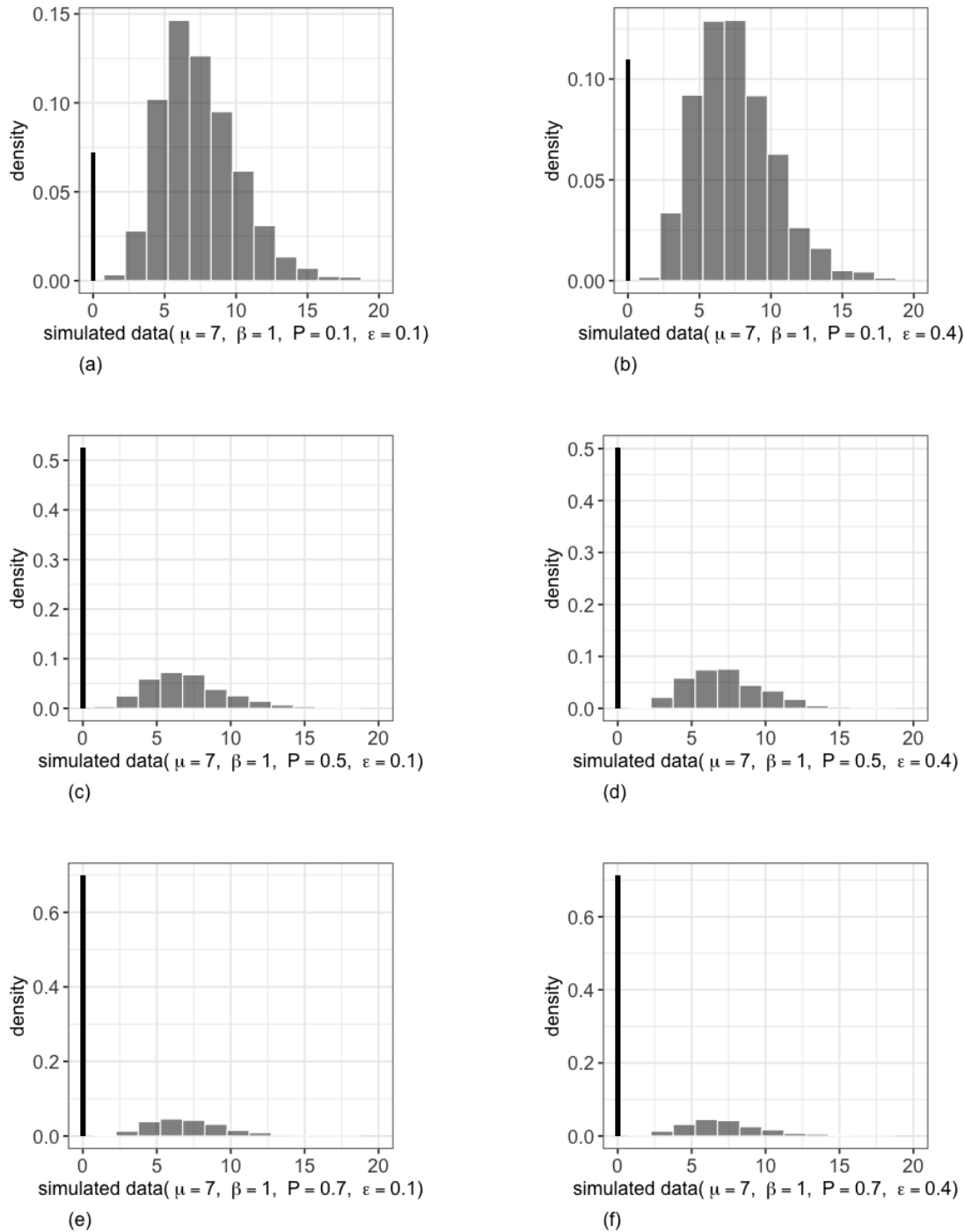


Figure C.7: Simulated data for Scenario 1. Grey bars are histogram of the data. Black bar is the zero-inflated probability.

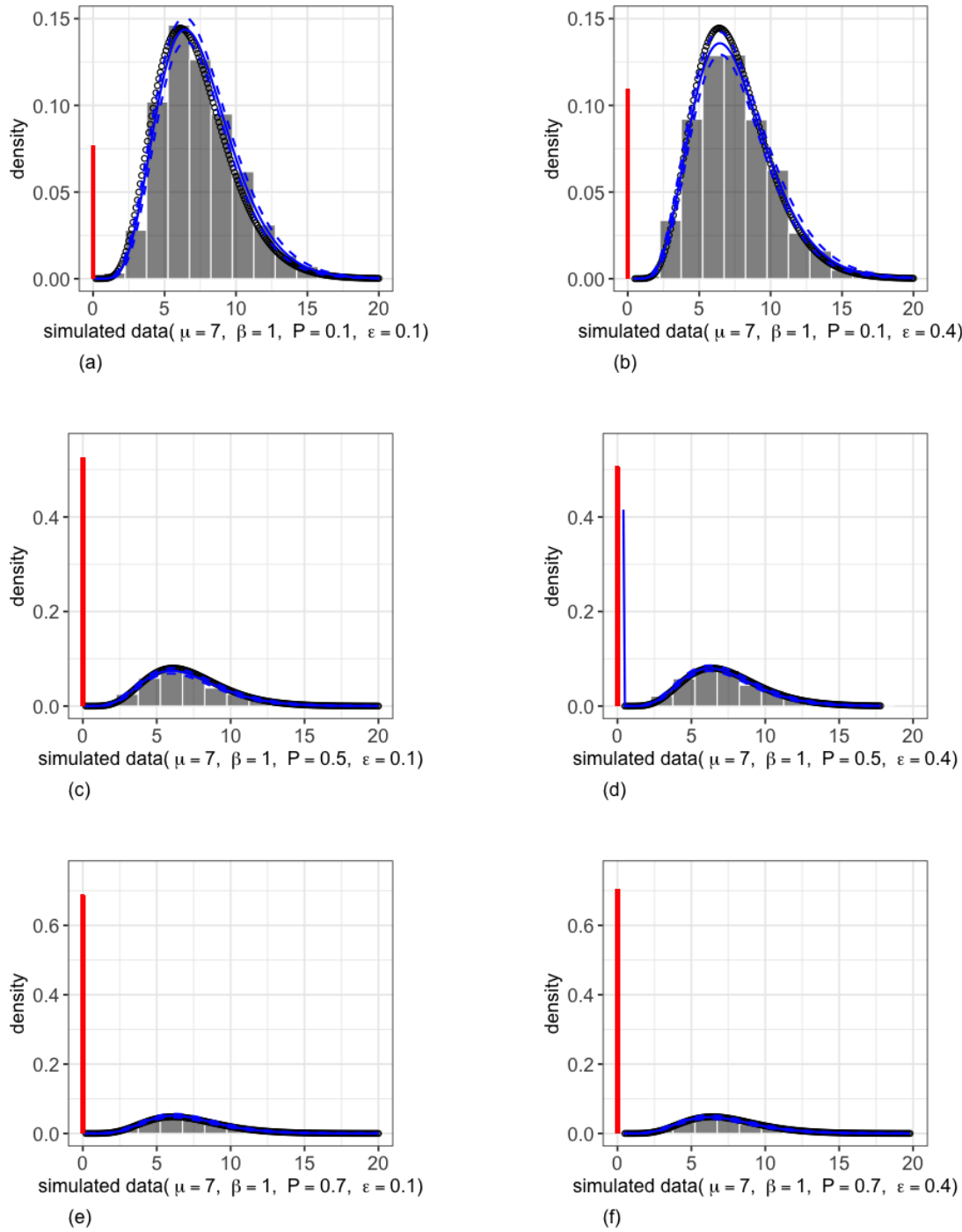


Figure C.8: Results for Scenario 1. Grey bars are histogram of the data. Circles are the true gamma density evaluated at the support, i.e., $x > 0$. Solid lines are the posterior means. Dashed lines are 95% credible intervals. Red bar is the zero-inflated probability.

Table C.1: Estimates and Gelman–Rubin Diagnostics for Scenario 1 ($P = 0.1$, $\epsilon = 0.1$) for parameters w , ρ , μ , β , P , and ϵ

.	Mean (SD)	R (Upper CI)	Naive SE	Time-series SE
$w_1 = 0.636$	0.6395 (0.0425)	1 (1)	0.0002	0.0003
$w_2 = 0.234$	0.1905 (0.0636)	1.01 (1.01)	0.0004	0.0013
$w_3 = 0.086$	0.1315 (0.0739)	1 (1)	0.0004	0.0021
$w_4 = 0.032$	0.0346 (0.0529)	1.01 (1.03)	0.0003	0.0017
$w_5 = 0.012$	0.0039 (0.0171)	1 (1)	0.0001	0.0004
$\rho_1 = 0.700$	0.6847 (0.0274)	1 (1)	0.0002	0.0002
$\rho_2 = 0.500$	0.606 (0.1426)	1.01 (1.01)	0.0008	0.0027
$\rho_3 = 0.300$	0.1168 (0.2389)	1 (1)	0.0013	0.0018
$\rho_4 = 0.100$	0.0147 (0.4675)	1 (1)	0.0026	0.0027
$\rho_5 = 0.100$	-0.0046 (0.5659)	1 (1)	0.0032	0.0032
μ	7.35 (0.1132)	1 (1)	0.0006	0.0006
β	1.0082 (0.0433)	1 (1)	0.0002	0.0002
P	0.0769 (0.0085)	1 (1)	0.0000	0.0000
ϵ	0.1 (7e-04)	1 (1)	0.0000	0.0000

Table C.2: Estimates and Gelman–Rubin Diagnostics for Scenario 2 ($P = 0.1$, $\epsilon = 0.1$) for parameters w , ρ , μ , β , P , and ϵ

.	Mean (SD)	R (Upper CI)	Naive SE	Time-series SE
$w_1 = 0.200$	0.1682 (0.0686)	1 (1)	0.0004	0.0012
$w_2 = 0.050$	0.0999 (0.0641)	1 (1)	0.0004	0.0012
$w_3 = 0.450$	0.4418 (0.0377)	1 (1)	0.0002	0.0003
$w_4 = 0.050$	0.0187 (0.0325)	1 (1)	0.0002	0.0007
$w_5 = 0.250$	0.2715 (0.0529)	1 (1)	0.0003	0.0006
$\rho_1 = 0.400$	0.3728 (0.1753)	1 (1)	0.0010	0.0026
$\rho_2 = 0.100$	-0.1457 (0.2685)	1 (1)	0.0015	0.0020
$\rho_3 = 0.700$	0.7399 (0.0321)	1 (1)	0.0002	0.0002
$\rho_4 = 0.100$	0.0687 (0.5259)	1 (1)	0.0029	0.0033
$\rho_5 = 0.500$	0.5701 (0.0753)	1 (1)	0.0004	0.0008
μ	7.232 (0.1128)	1 (1)	0.0006	0.0006
β	1.0705 (0.0452)	1 (1)	0.0003	0.0003
P	0.0812 (0.0087)	1 (1)	0.0000	0.0000
ϵ	0.1004 (7e-04)	1 (1)	0.0000	0.0000

Table C.3: Estimates and Gelman–Rubin Diagnostics for Scenario 1 (varying P , ϵ) for parameters μ , β , P , and ϵ

.	Mean (SD)	R (Upper CI)	Naive SE	Time-series SE
μ	7.35 (0.1132)	1 (1)	0.0006	0.0006
β	1.0082 (0.0433)	1 (1)	0.0002	0.0002
P	0.0769 (0.0085)	1 (1)	0.0000	0.0000
ϵ	0.1 (7e-04)	1 (1)	0.0000	0.0000
μ	7.1454 (0.12)	1 (1)	0.0007	0.0007
β	1.0994 (0.0472)	1 (1)	0.0003	0.0003
P	0.1091 (0.0103)	1 (1)	0.0001	0.0001
ϵ	0.4017 (0.0019)	1 (1)	0.0000	0.0000
μ	6.9447 (0.1207)	1 (1)	0.0007	0.0007
β	1.0659 (0.0542)	1 (1)	0.0003	0.0003
P	0.5248 (0.0172)	1 (1)	0.0001	0.0001
ϵ	0.1001 (1e-04)	1 (1)	0.0000	0.0000
μ	6.8454 (0.1154)	1 (1)	0.0006	0.0006
β	1.0086 (0.0512)	1 (1)	0.0003	0.0003
P	0.5064 (0.0173)	1 (1)	0.0001	0.0001
ϵ	0.4 (4e-04)	1 (1)	0.0000	0.0000
μ	6.988 (0.1303)	1 (1)	0.0007	0.0007
β	0.9593 (0.0594)	1 (1)	0.0003	0.0003
P	0.6879 (0.016)	1 (1)	0.0001	0.0001
ϵ	0.0999 (1e-04)	1 (1)	0.0000	0.0000
μ	6.8482 (0.1373)	1 (1)	0.0008	0.0008
β	1.0506 (0.0665)	1 (1)	0.0004	0.0004
P	0.7048 (0.0154)	1 (1)	0.0001	0.0001
ϵ	0.4002 (3e-04)	1 (1)	0.0000	0.0000

Table C.4: Estimates and Gelman–Rubin Diagnostics for Scenario 2 (varying P , ϵ) for parameters μ , β , P , and ϵ

.	Mean (SD)	R (Upper CI)	Naive SE	Time-series SE
μ	7.232 (0.1128)	1 (1)	0.0006	0.0006
β	1.0705 (0.0452)	1 (1)	0.0003	0.0003
P	0.0812 (0.0087)	1 (1)	0.0000	0.0000
ϵ	0.1004 (7e-04)	1 (1)	0.0000	0.0000
μ	7.0911 (0.1046)	1 (1)	0.0006	0.0006
β	1.0208 (0.0414)	1 (1)	0.0002	0.0002
P	0.1028 (0.0094)	1 (1)	0.0001	0.0001
ϵ	0.401 (0.002)	1 (1)	0.0000	0.0000
μ	7.0274 (0.1177)	1 (1)	0.0007	0.0007
β	1.0182 (0.0533)	1 (1)	0.0003	0.0003
P	0.5334 (0.0172)	1 (1)	0.0001	0.0001
ϵ	0.1001 (1e-04)	1 (1)	0.0000	0.0000
μ	6.932 (0.1184)	1 (1)	0.0007	0.0007
β	1.0968 (0.0557)	1 (1)	0.0003	0.0003
P	0.5034 (0.0172)	1 (1)	0.0001	0.0001
ϵ	0.4002 (4e-04)	1 (1)	0.0000	0.0000
μ	7.032 (0.1304)	1 (1)	0.0007	0.0007
β	0.9507 (0.0605)	1 (1)	0.0003	0.0003
P	0.6957 (0.0154)	1 (1)	0.0001	0.0001
ϵ	0.1001 (1e-04)	1 (1)	0.0000	0.0000
μ	6.9182 (0.1347)	1 (1)	0.0008	0.0008
β	0.9858 (0.0654)	1 (1)	0.0004	0.0004
P	0.7285 (0.0145)	1 (1)	0.0001	0.0001
ϵ	0.3999 (3e-04)	1 (1)	0.0000	0.0000

Appendix D: Predictions for Gamma MTD Models

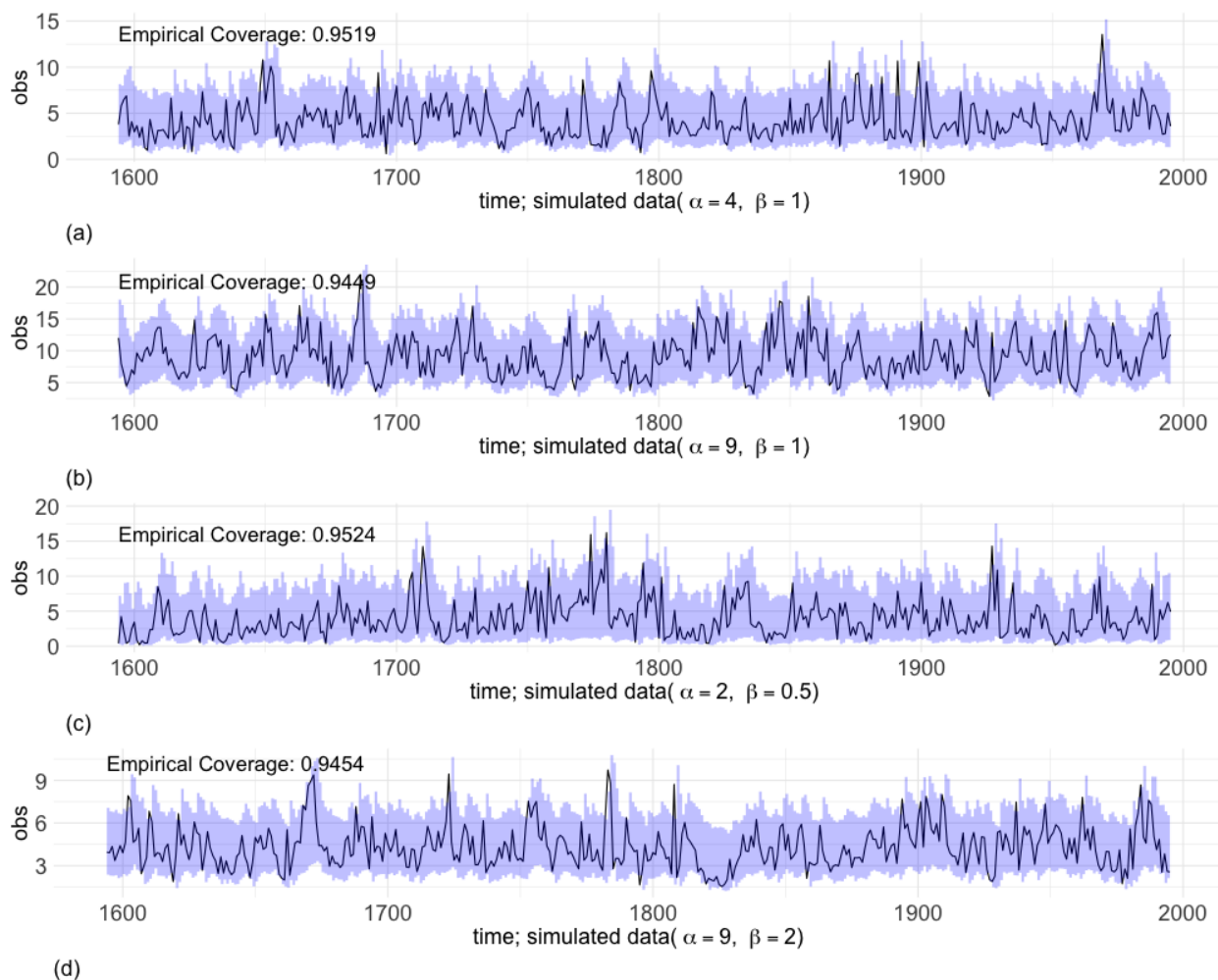


Figure D.1: 95% one-step ahead posterior predictive intervals for (a) Gamma Scenario 3, (b) Scenario 4, (c) Scenario 5, and (d) Scenario 6.

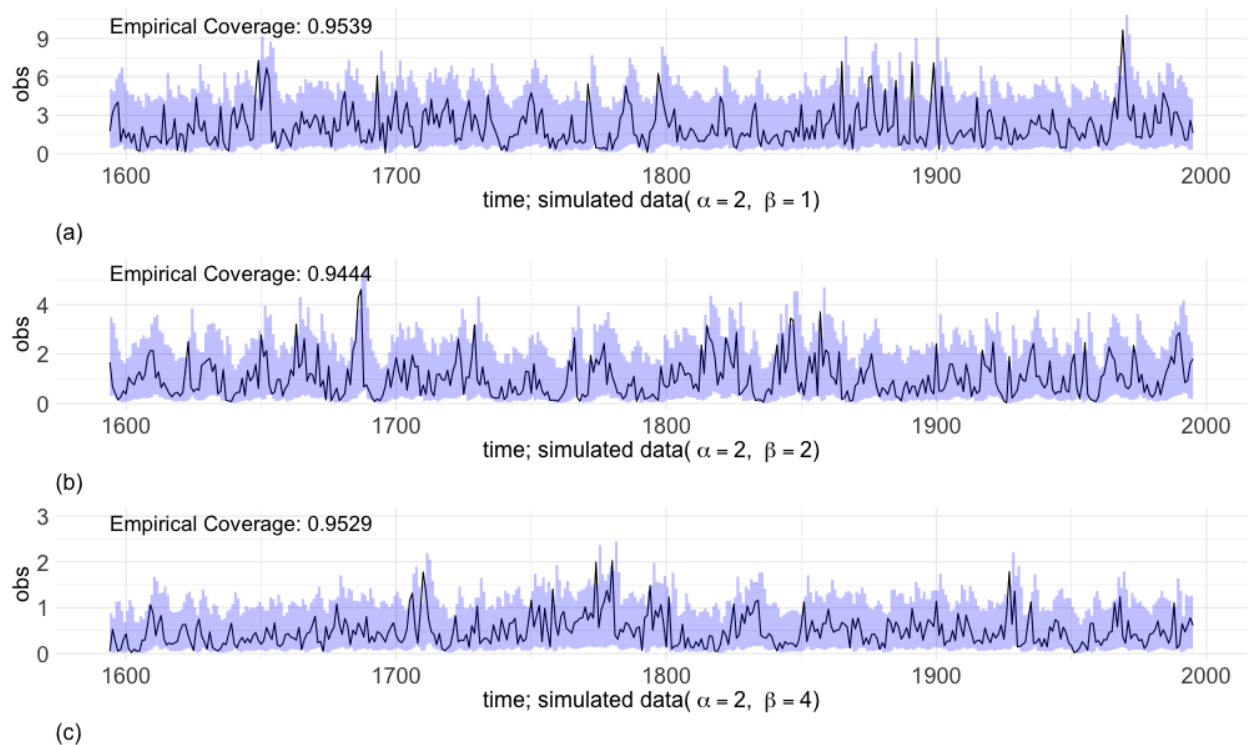


Figure D.2: 95% one-step ahead posterior predictive intervals for (a) Gamma Scenario 7, (b) Scenario 8, and (c) Scenario 9.

Appendix E: Predictions for Zero-Inflated Gamma MTD Models

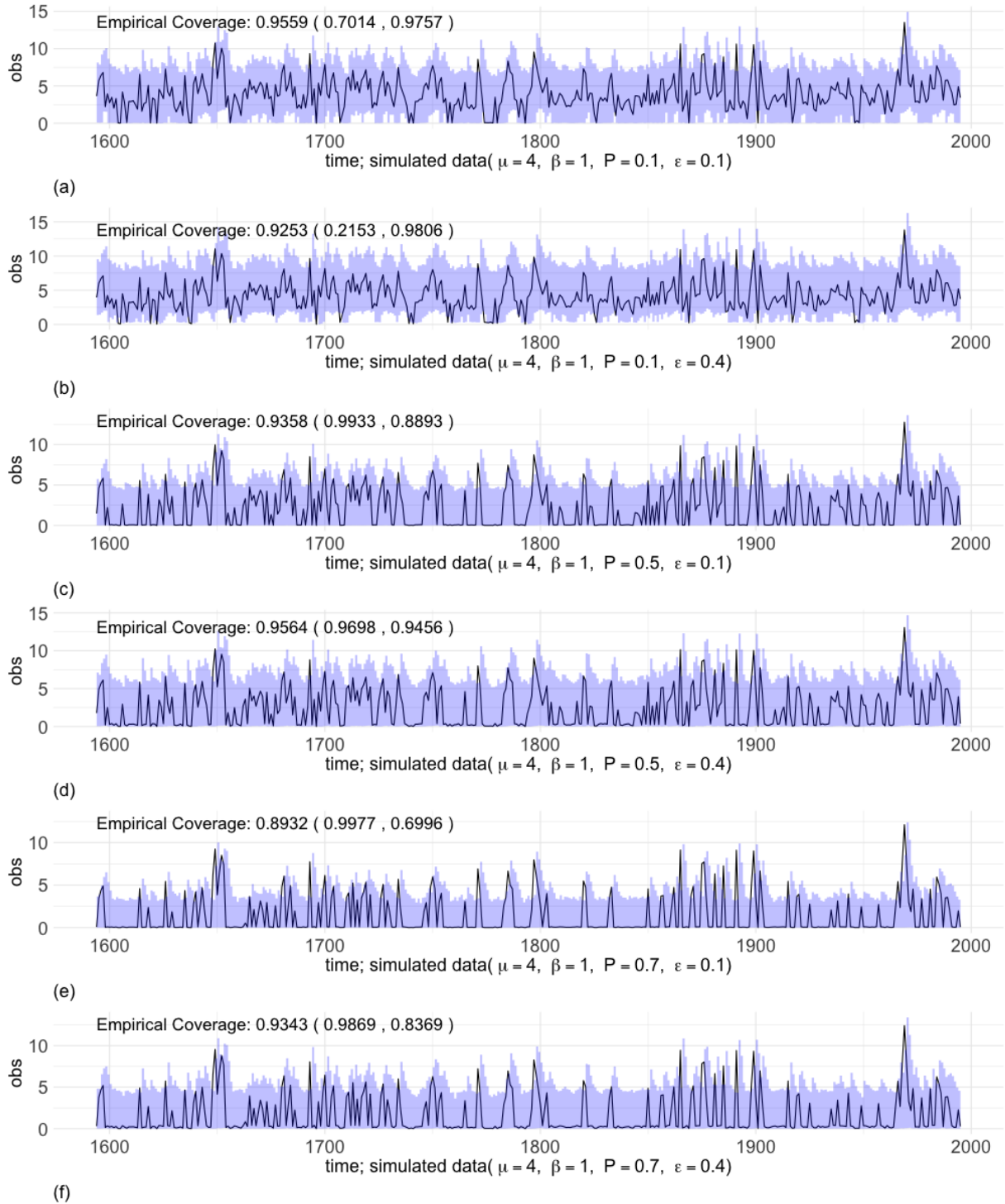


Figure E.1: 95% one-step ahead posterior predictive intervals for ZIGamma Scenario 3. Reported values show overall empirical coverage, with decomposed coverage below and above the threshold shown in parentheses: coverage (coverage for data $\leq \epsilon$, coverage for data $> \epsilon$).

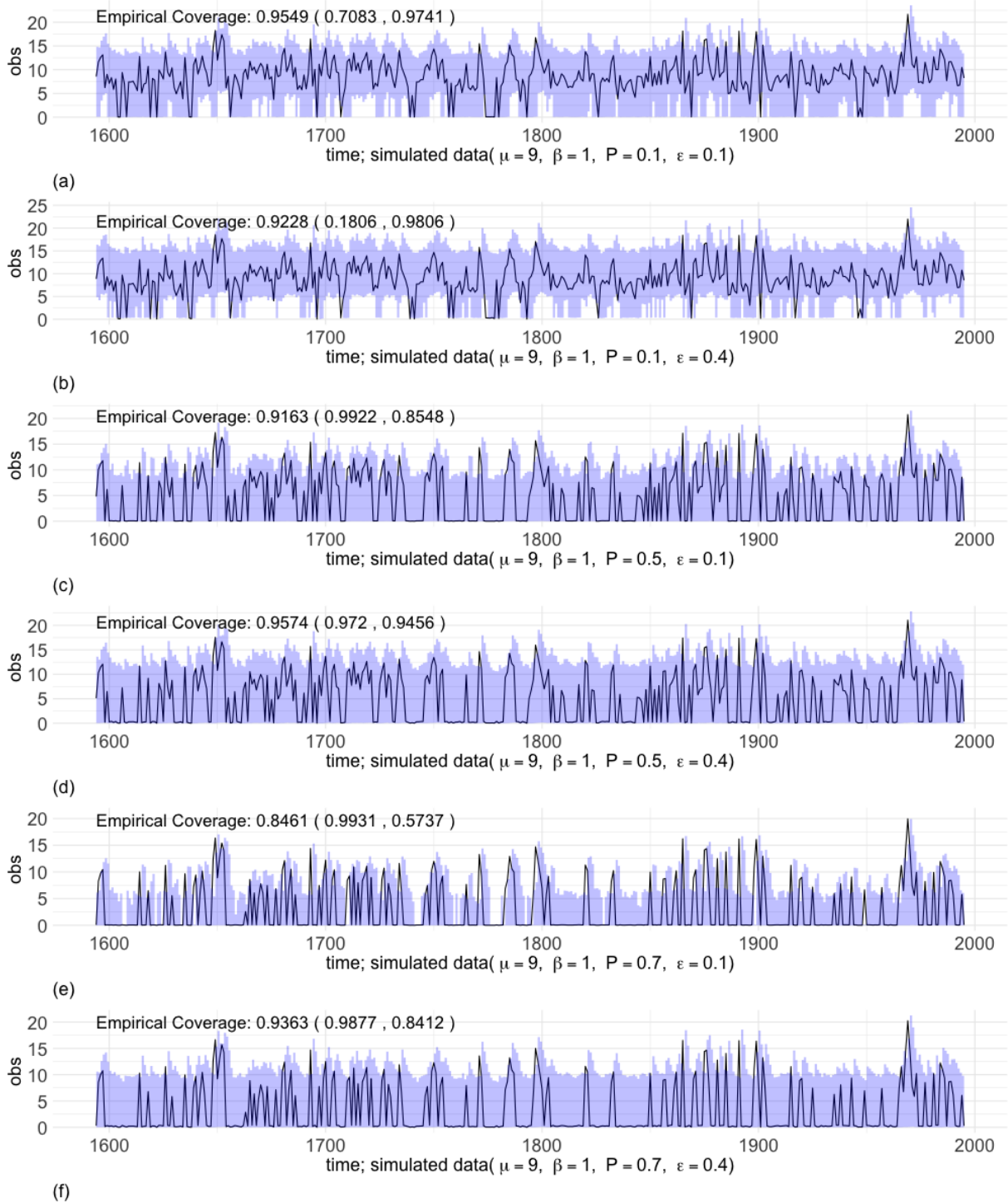


Figure E.2: 95% one-step ahead posterior predictive intervals for ZIGamma Scenario 4. Reported values show overall empirical coverage, with decomposed coverage below and above the threshold shown in parentheses: coverage (coverage for data $\leq \epsilon$, coverage for data $> \epsilon$).

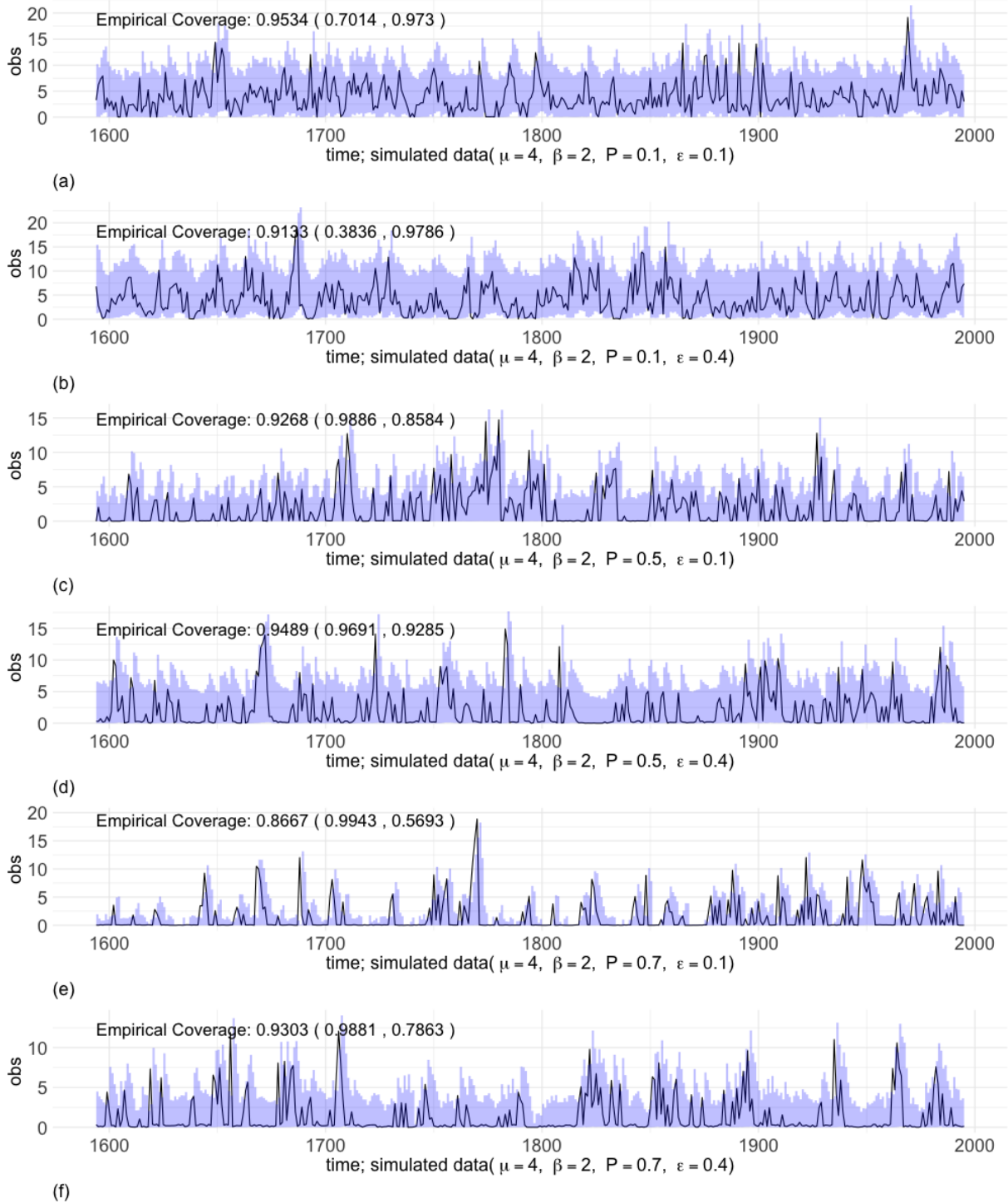


Figure E.3: 95% one-step ahead posterior predictive intervals for ZIGamma Scenario 5. Reported values show overall empirical coverage, with decomposed coverage below and above the threshold shown in parentheses: coverage (coverage for data $\leq \epsilon$, coverage for data $> \epsilon$).

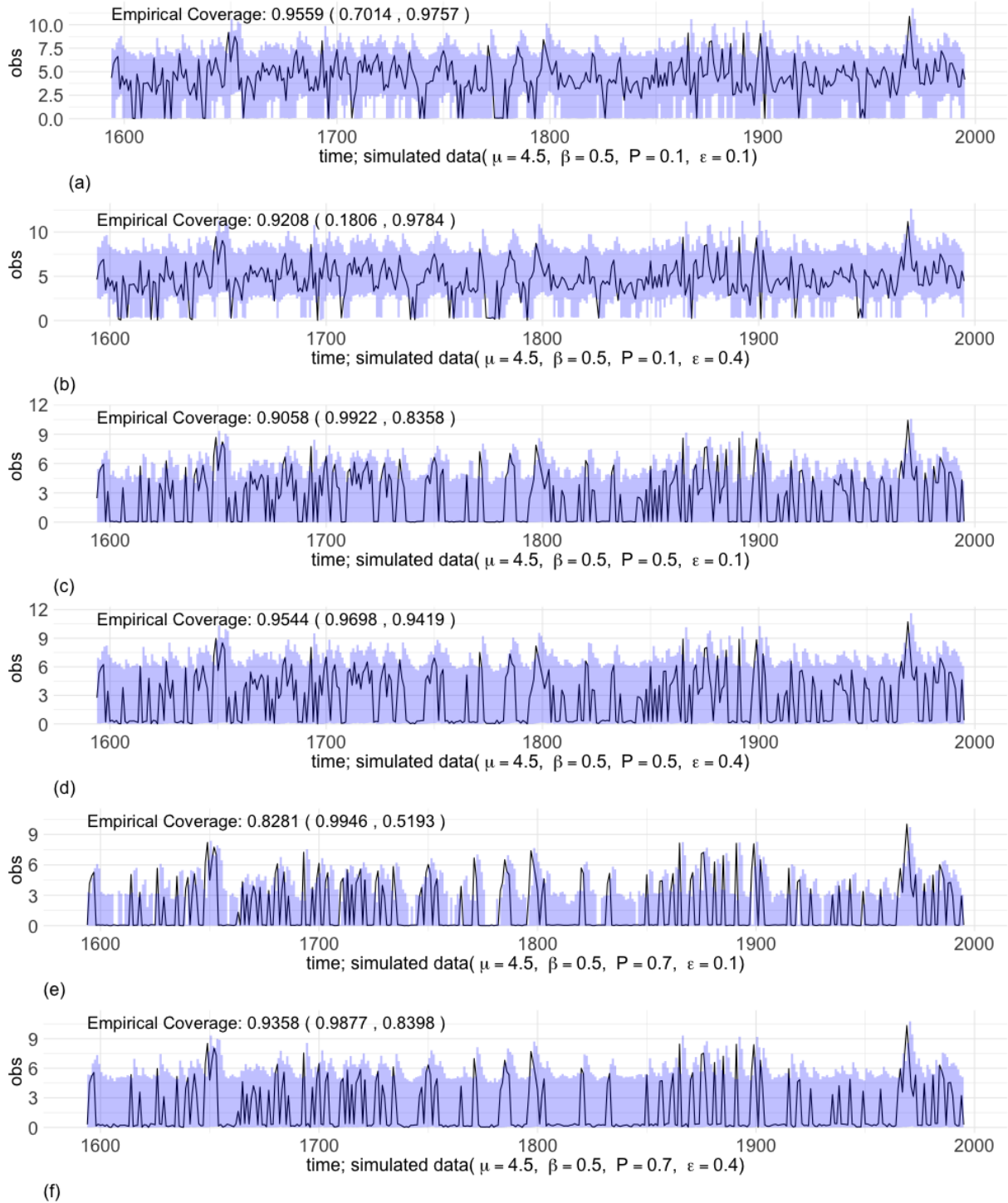


Figure E.4: 95% one-step ahead posterior predictive intervals for ZIGamma Scenario 6. Reported values show overall empirical coverage, with decomposed coverage below and above the threshold shown in parentheses: coverage (coverage for data $\leq \epsilon$, coverage for data $> \epsilon$).

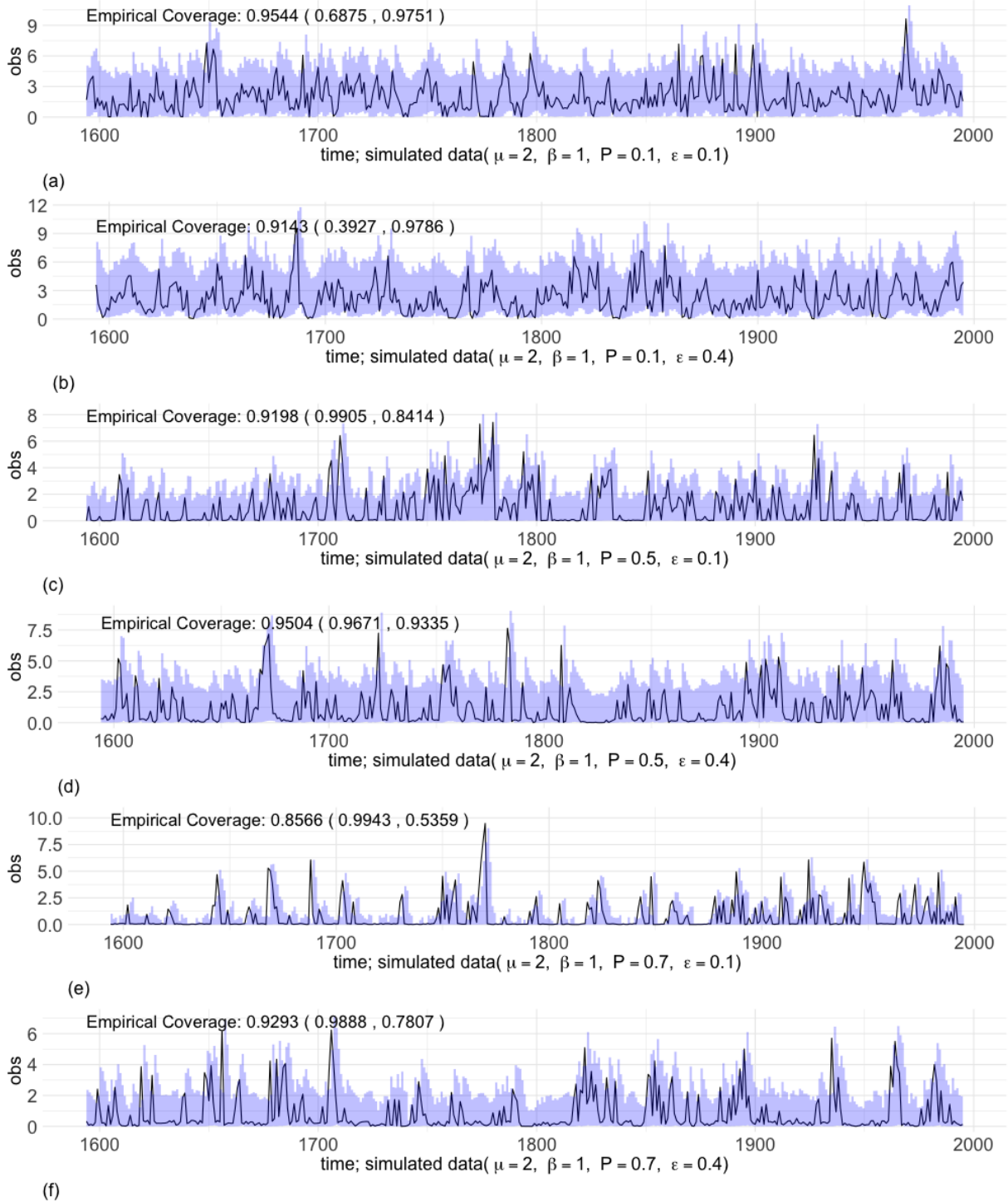


Figure E.5: 95% one-step ahead posterior predictive intervals for ZIGamma Scenario 7. Reported values show overall empirical coverage, with decomposed coverage below and above the threshold shown in parentheses: coverage (coverage for data $\leq \epsilon$, coverage for data $> \epsilon$).

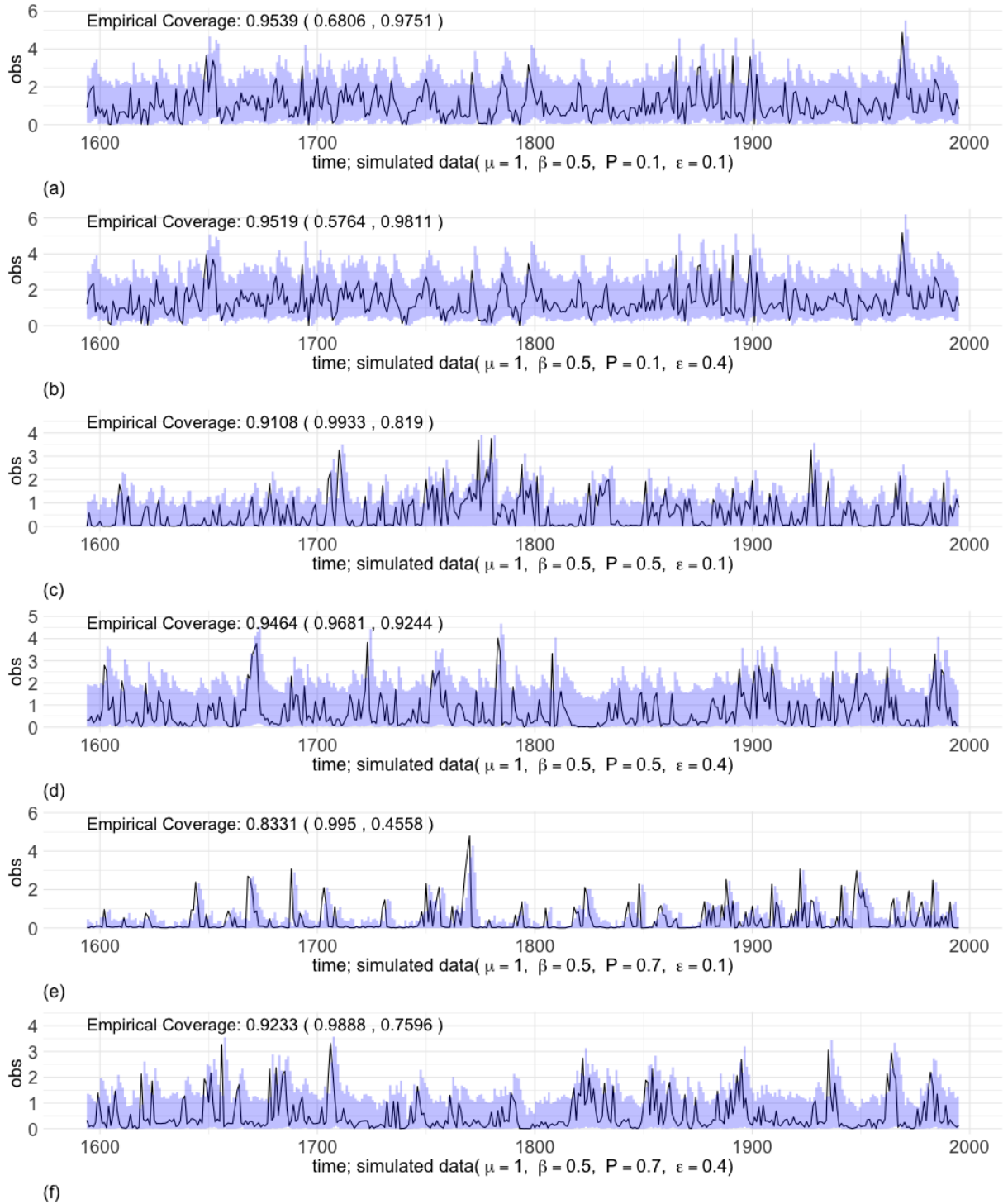


Figure E.6: 95% one-step ahead posterior predictive intervals for ZIGamma Scenario 8. Reported values show overall empirical coverage, with decomposed coverage below and above the threshold shown in parentheses: coverage (coverage for data $\leq \epsilon$, coverage for data $> \epsilon$).

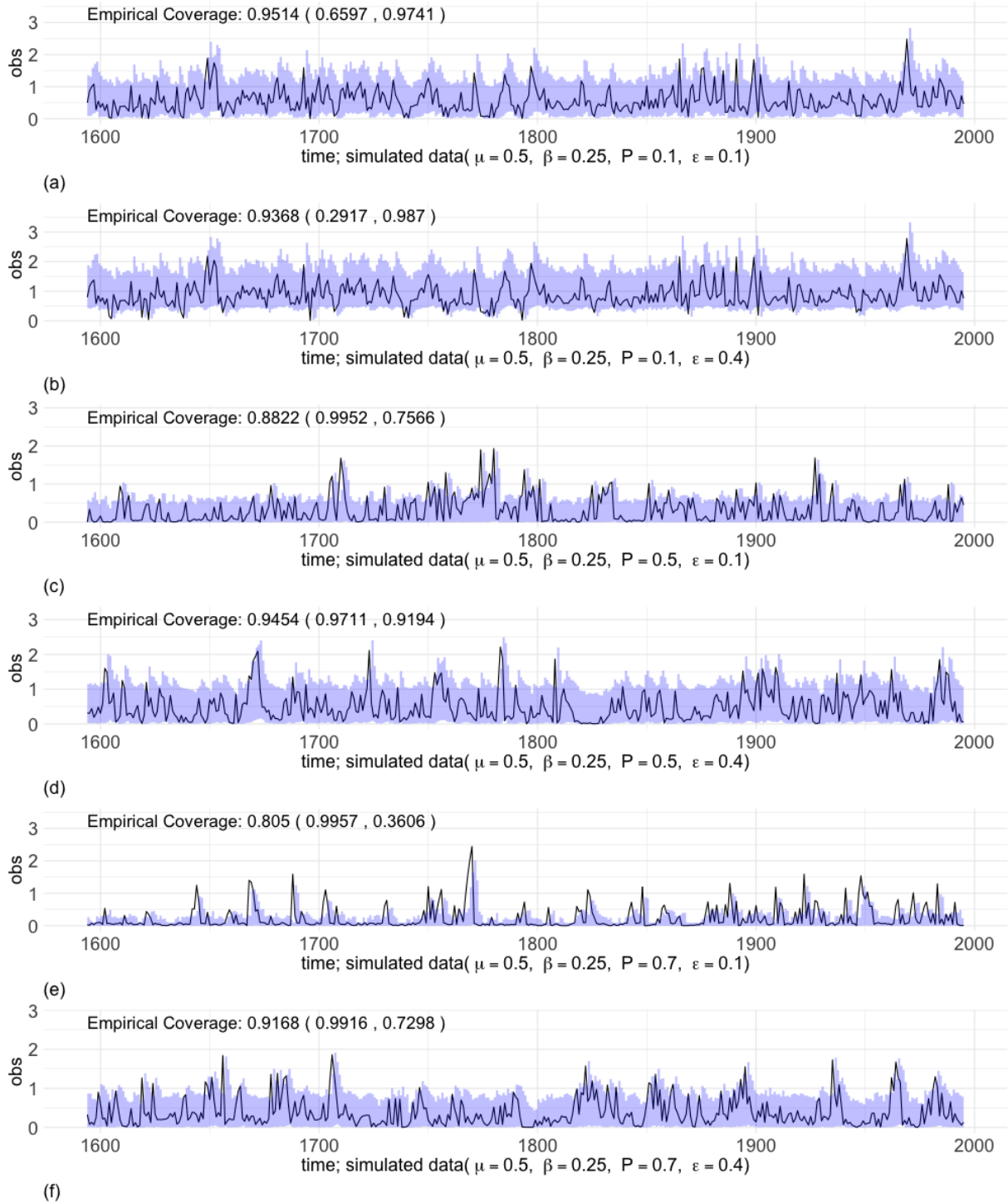


Figure E.7: 95% one-step ahead posterior predictive intervals for ZIGamma Scenario 9. Reported values show overall empirical coverage, with decomposed coverage below and above the threshold shown in parentheses: coverage (coverage for data $\leq \epsilon$, coverage for data $> \epsilon$).

Appendix F: Predictions for MTD Models vs LSTM Networks

F.1 Gamma

F.2 Zero-Inflated Gamma

F.3 Data Applications

Table F.1: RMSE Comparison of LSTM and MTD for ZIGamma Scenarios 2. Each row label indicates the combination of P (zero-inflated probability) and ϵ (threshold value) used in the simulation.

.	LSTM	MTD
P01Eps01	3.0477	3.2302
P01Eps04	3.3478	3.5392
P05Eps01	3.5281	3.8117
P05Eps04	3.7440	3.9138
P07Eps01	3.2557	3.3914
P07Eps04	3.0371	3.0929

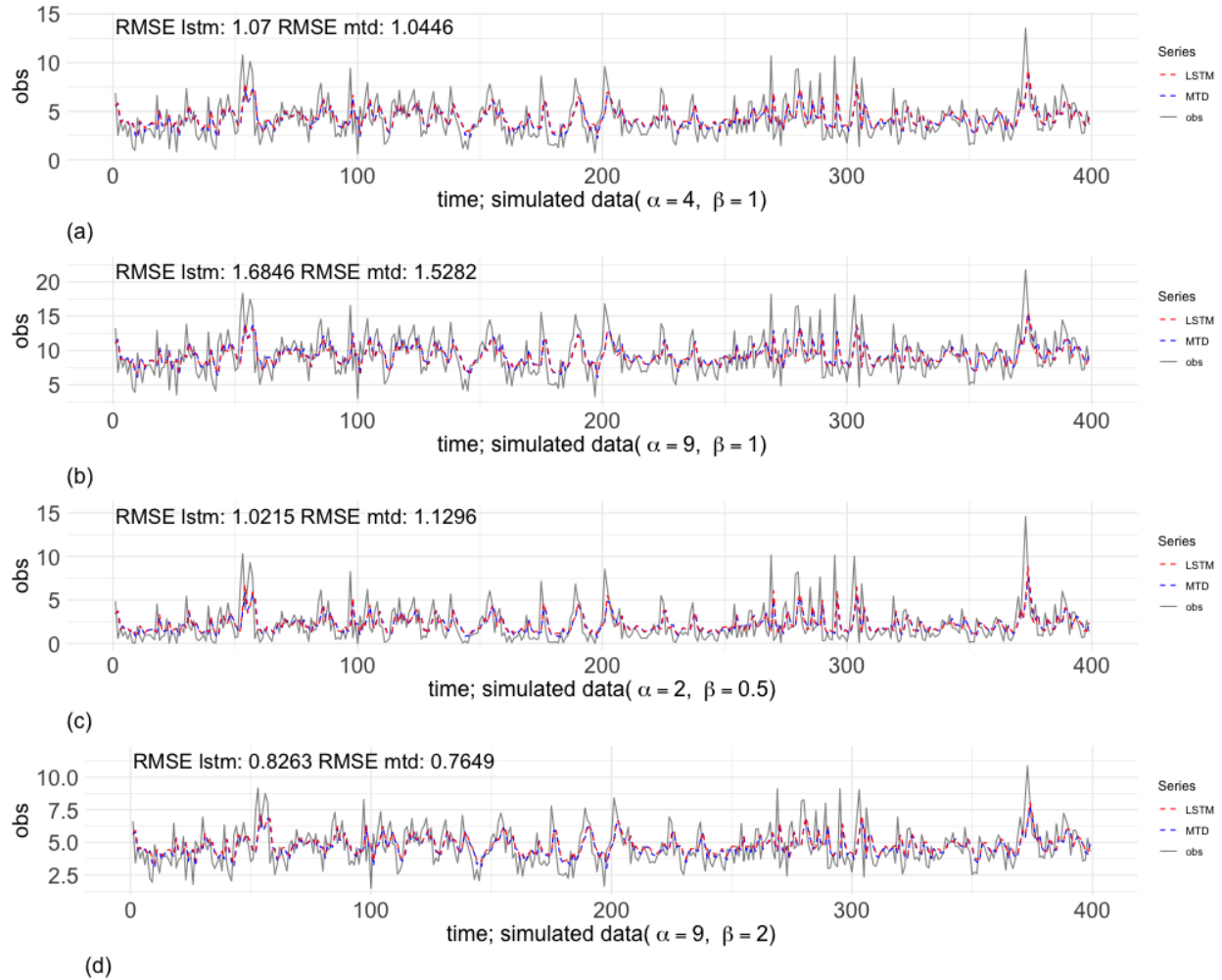


Figure F.1: One-step ahead predicted means for Gamma Scenario 3, 4, 5, 6: Solid (black) lines are true values. Dashed (red) lines are LSTM predicted means and dashed (blue) lines are MTD predicted means.

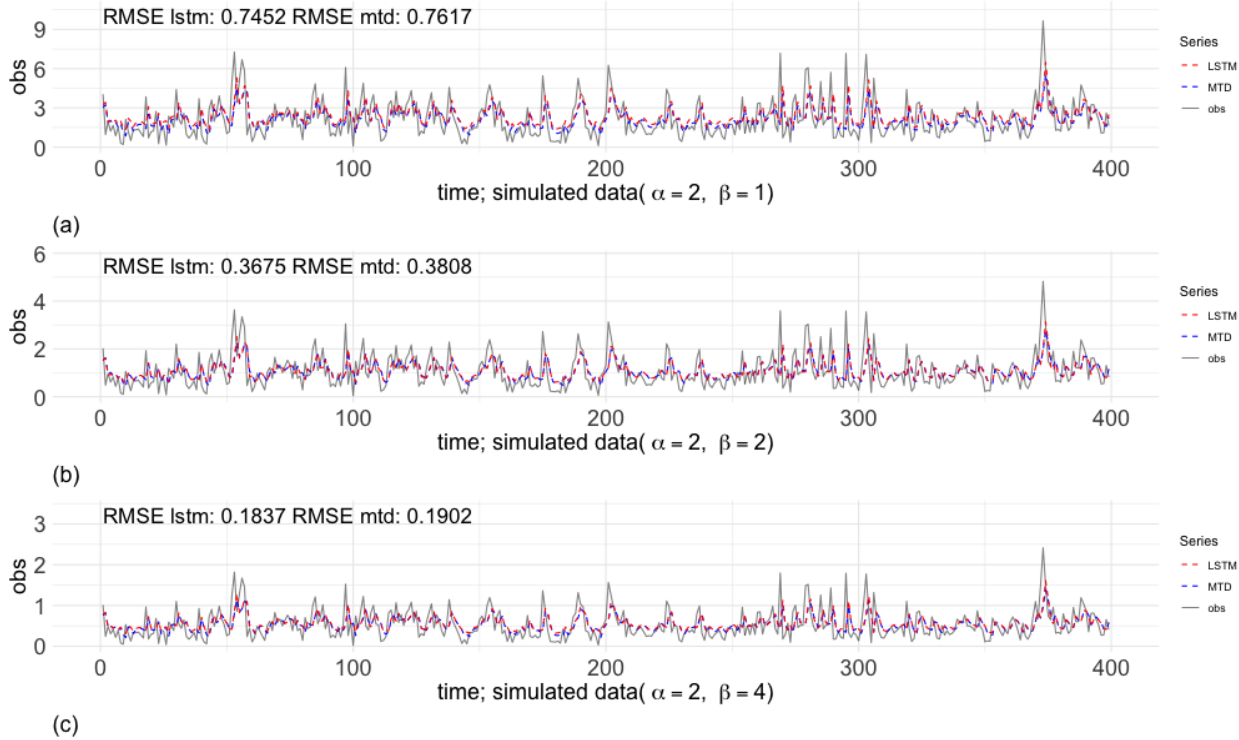


Figure F.2: One-step ahead predicted means for Gamma Scenario 7, 8, 9: Solid (black) lines are true values. Dashed (red) lines are LSTM predicted means and dashed (blue) lines are MTD predicted means.

Table F.2: RMSE Comparison of LSTM and MTD for ZIGamma Scenarios 2 Above and Below. Each row label indicates the combination of P (zero-inflated probability) and ϵ (threshold value) used in the simulation. Reported values show overall RMSE, with decomposed RMSE below and above the threshold.

.	LSTM Below	MTD Below	LSTM Above	MTD Above
P01Eps01	6.8130	6.5172	2.6077	2.8787
P01Eps04	5.2474	7.0593	2.9948	2.7220
P05Eps01	2.8224	1.6276	4.2344	5.3911
P05Eps04	2.9031	3.0532	4.6896	4.8859
P07Eps01	1.8206	0.8683	5.4472	6.2960
P07Eps04	1.6255	1.1711	5.6060	6.1000

Table F.3: Bias Comparison of LSTM and MTD for ZIGamma Scenarios 2. Each row label indicates the combination of P (zero-inflated probability) and ϵ (threshold value) used in the simulation.

.	LSTM	MTD
P01Eps01	0.4133	0.0071
P01Eps04	-0.6692	0.9213
P05Eps01	-0.0042	-1.3811
P05Eps04	0.0165	-0.0439
P07Eps01	-0.0872	-1.1302
P07Eps04	0.0396	-0.5514

Table F.4: Bias Comparison of LSTM and MTD for ZIGamma Scenarios 2 Above and Below. Each row label indicates the combination of P (zero-inflated probability) and ϵ (threshold value) used in the simulation. Reported values show overall RMSE, with decomposed RMSE below and above the threshold.

.	LSTM Below	MTD Below	LSTM Above	MTD Above
P01Eps01	6.7605	6.3816	-0.0121	-0.4202
P01Eps04	5.2015	7.0151	-1.4743	0.0856
P05Eps01	2.7283	1.3505	-3.3473	-4.7232
P05Eps04	2.7923	2.7756	-3.9440	-4.0667
P07Eps01	1.6980	0.6320	-4.7611	-5.7438
P07Eps04	1.5469	0.9310	-5.0453	-5.5523

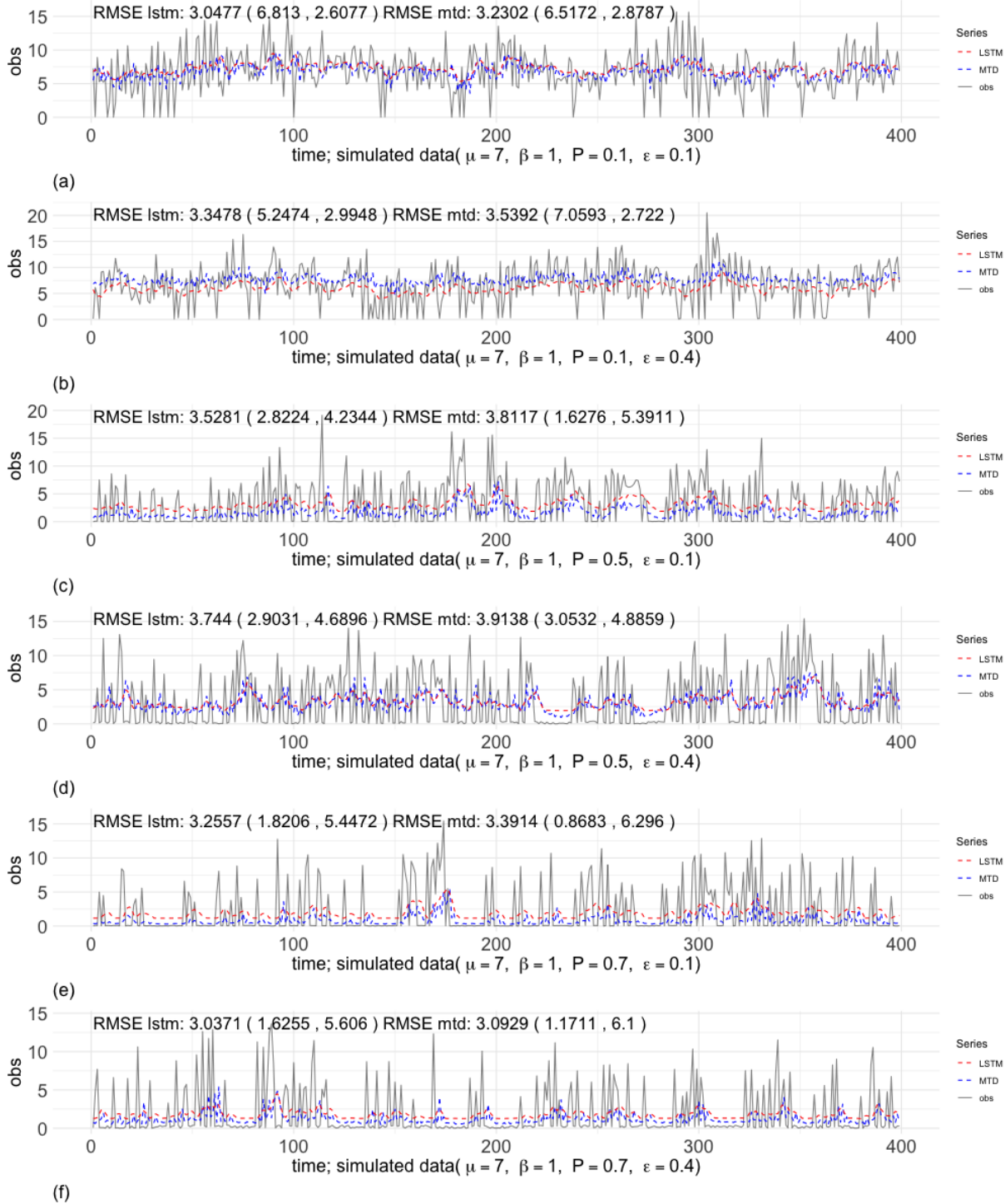


Figure F.3: One-step ahead predicted means for Gamma Scenario 2: Solid (black) lines are true values. Dashed (red) lines are LSTM predicted means and dashed (blue) lines are MTD predicted means. Reported values show overall RMSE, with decomposed RMSE below and above the threshold shown in parentheses: RMSE (RMSE for data $\leq \epsilon$, RMSE for data $> \epsilon$).

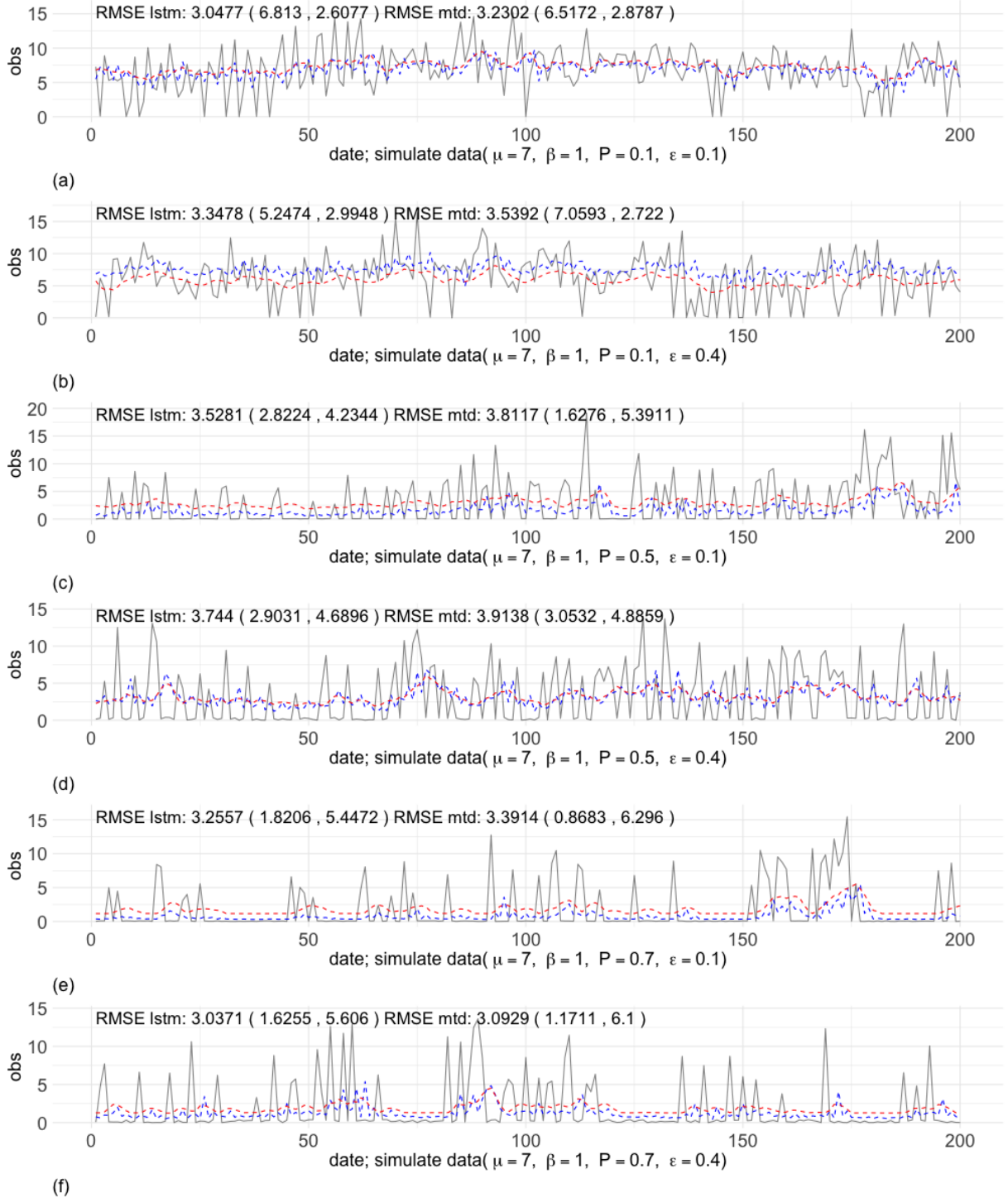


Figure F.4: Zoomed-in view of one-step ahead predicted means for ZIGamma Scenario 2: Solid (black) lines are true values. Dashed (red) lines are LSTM predicted means and dashed (blue) lines are MTD predicted means. Reported values show overall RMSE, with decomposed RMSE below and above the threshold shown in parentheses: RMSE (RMSE for data $\leq \epsilon$, RMSE for data $> \epsilon$).

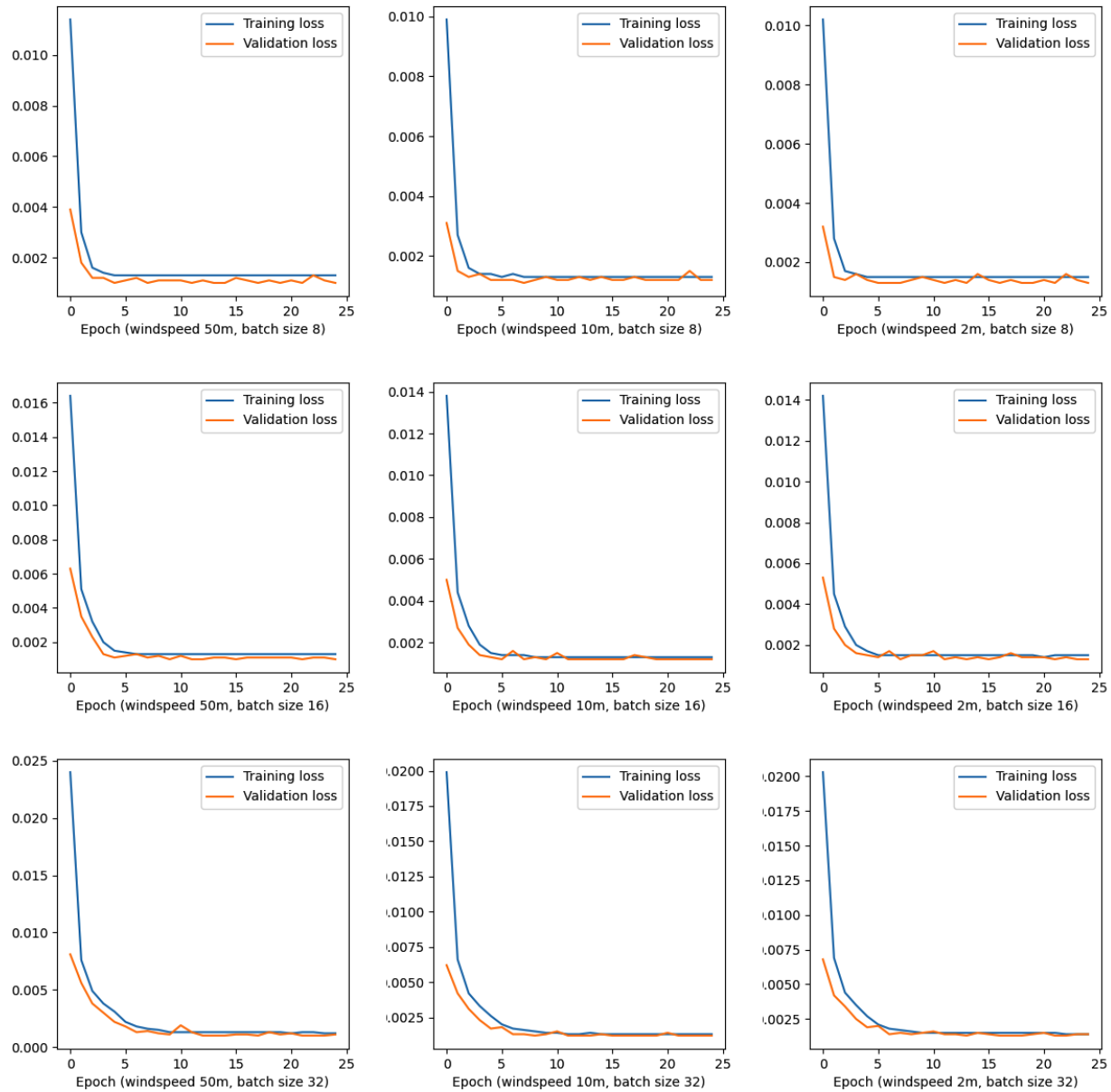


Figure F.5: Training and validation loss curves for the LSTM model. Columns (left to right) correspond to wind speeds at 50 m, 10 m, and 2 m above ground level, respectively. Rows (top to bottom) correspond to batch sizes 8, 16, and 32, respectively.

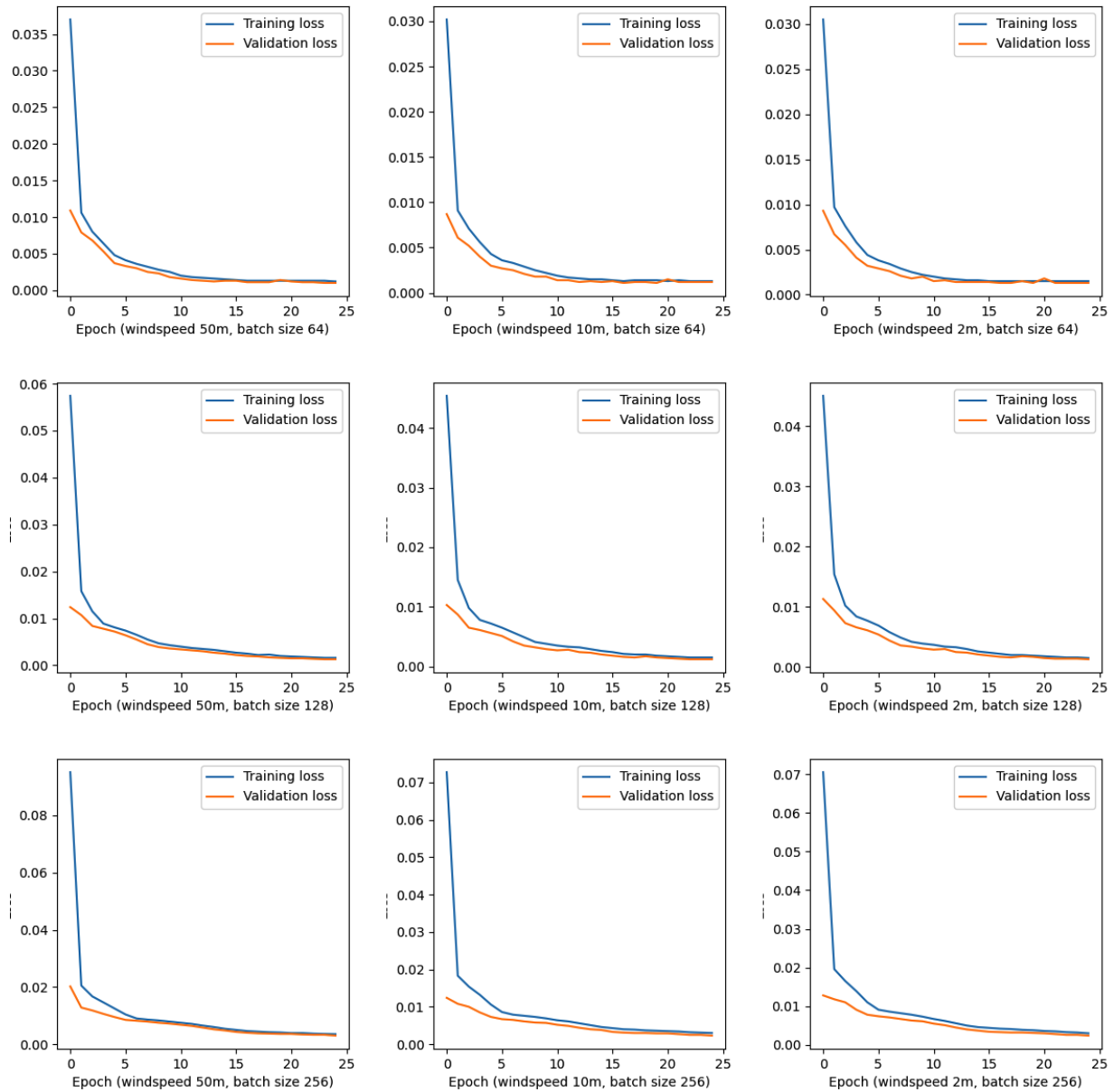


Figure F.6: Training and validation loss curves for the LSTM model. Columns (left to right) correspond to wind speeds at 50 m, 10 m, and 2 m above ground level, respectively. Rows (top to bottom) correspond to batch sizes 64, 128, and 256, respectively.

Appendix G: **mtd**: An R Package for Modeling Gamma and Zero-inflated Gamma Time Series

G.1 Extension to the **mtd** Package

The **mtd** package by Zheng et al. (2022) includes the Gaussian, Poisson, Negative Binomial, and Lomax MTD regression models. We extend the package to include the copula-based Gamma and zero-inflated Gamma MTD models.

The original **mtd** package can be installed and loaded from GitHub:

```
devtools::install_github("xzheng42/mtd")
library(mtd)
```

G.2 Installation of the Extended **mtd** Package

The extended **mtd** package can be installed and loaded from GitHub:

```
devtools::install_github("franceslinyc/mtd")
library(mtd)
```

